Abstract

Zhao, Qingzhong. Mechanical and Transport Properties of Carbon Nanotube Systems. (Under the direction of Jerry Bernholc.)

This dissertation consists of four parts. The first part reviews our computational methods. The *ab initio* method, extensively used through out the whole work, is the main focus of the first part. A new large scale order-N *ab initio* method is also introduced and we discuss our experience with this promising new methodology. In the second part, a brief introduction to carbon nanotubes is given, and SWNT's amazing mechanical and electrical transport properties are discussed. By studying the defect formation of CNT under tensile strain, we probe the ultimate strength of CNT in the third part. In the final part, large scale quantum transport simulations were carried out to investigate the electrical properties of a new carbon nanotube based material: carbon nanotube-metal cluster assembly. This new material could lead to novel good chemical sensors.

Chapter 1 gives an overview of theoretical methods involved in this dissertation. The big three commonly used computation methods: classical molecular dynamics, tight-binding and *ab initio* method are introduced one by one, with greater emphasis on *ab initio* total-energy calculations. Detailed explanations are given to *ab initio* method's infrastructure building blocks: DFT, LDA and pseudopotentials. Popular iterative minimization techniques for total-energy pseudopotential calculations, like Car-Parrinello Molecular Dynamics (CPMD), Steepest Descent (SD), Conjugate Gradient(CG) and Multigrid (MG) are reviewed. A new linear scaling *ab initio* method based on nonorthogonal local orbitals is introduced, and the implementation, improvement and

application of the new method are also discussed. In the end, an assessment of all theoretical methods is provided, based on our experience in this dissertation.

Since this theoretical project is targeted on CNT and related nano-structures, a detailed introduction to carbon nanotube systems is given in Chapter 2. The large variety of possible helical geometries and strong and flexible covalent carbon bonds give carbon nanotube systems so many extraordinary physical properties. CNTs can provide unmatched strength and they can be excellent conductors or semi-conductors, depending only on their geometries.

In Chapter 3, the ultimate strength of carbon nanotubes is investigated by large-scale ab initio, tight-binding and classical molecular dynamics calculations. While the formation energy of strain-induced topological defects determines the thermodynamic limits of the elastic response and of mechanical resistance to applied tension, it is found that the activation barriers for the formation of such defects are much larger than estimated previously. The theoretical results indicate a substantially greater resilience and strength, and show that the ultimate strength limit of carbon nanotubes has yet to be reached experimentally. Carbon nanotubes are indeed the strongest material known.

Using large scale O(N) *ab initio* method, we have theoretically investigated the quantum transport properties of carbon nanotube-metal cluster assemblies in a gas environment. For an Al cluster attached to a metallic nanotube, we have observed that its electrical response dramatically changes upon NH3 adsorption onto the metal cluster. For a semiconducting nanotube-Al cluster assembly, the same gas adsorption enhances the system's conductivity. The results of our *ab initio* computer simulations explain the observed behavior in terms of interactions between the molecular species and the

nanotube-cluster system, where successive charge transfers between the components tailor the electronic and transport properties. We will discuss the relation between the electronic response and the mechanism of molecular sensing, and present possible ways to improve the detection of different species.

Mechanical and Transport Properties of Carbon Nanotube Systems

by

Qingzhong Zhao

Under the direction of Prof. Jerry Bernholc

A dissertation submitted to the Graduate Faculty of
North Carolina State University
in partial fulfillment of the
requirements for the Degree of
Doctor of Philosophy

Department of Physics

Raleigh

2003

Approved by:

_____	_____
Dr. Jerry Bernholc Chair of Advisory Committee	Dr. Marco Buongiorno Nardelli
_____	_____
Dr. Christopher Roland	Dr. Frank, Mueller

Biography

Qingzhong Zhao was born on June 1st, 1971 in Qinghe, Hebei province, China. He grew up in a small and quiet village in Taihang Mountains until 7, and then moved to Qinghe to live with his parents until he graduated from Qinghe High School. His parents always encouraged him to explore and develop his interests in Mathematics and Physics. In 1990, he entered Lanzhou University to study physics. After graduation, he was accepted a position as a graduate student at the Institute of Modern Physics in Lanzhou. To pursue his academic goals, he came to the United States as a Ph. D. candidate of the Department of Physics at North Carolina State University in August 1997. In the second year, he joined the Solid State Theory group.

Acknowledgements

First, I would like to thank my advisor, Prof. Jerry Bernholc, for his constant support and encouragement. Without his enthusiasm and guidance, the research projects reported in this dissertation would never have been completed. I would also like to thank Prof. Marco Buongiorno Nardelli for his daily guidance. I really appreciate Prof. Wenchang Lu's help in computational techniques and many more. Thanks are due to Prof. Christopher Roland for helpful suggestions. I would also like to thank Prof. Frank Mueller and his student Yifan Zhu's help in programming techniques. I am very grateful to J.-L. Fattebert for the fruitful discussions on the O(N) method. Thanks are also due to Emil Briggs, Shuchun Wang and others for their helpful discussions and everyday help. This work was supported in part by grants from NASA and ONR. We thank also DoD, NSF and NC Supercomputing Centers for extensive computing support.

Finally, I thank my wife and my parents for their love and support.

TABLE OF CONTENTS

List of Tables

List of Figures

List of Acronyms

TB	Tight-Binding
DFT	Density Functional Theory
LCAO	Linear Combination of Atomic Orbitals
PBC	Periodic Boundary Conditions
KS	Kohn-Sham
LDA	Local Density Approximation
GGA	Generalized Gradient Approximation
HF	Hartree-Fock
DOS	Density-of-States
FFT	Fast Fourier Transform
MG	MultiGrid
SD	Steepest Descent
CG	Conjugate Gradient
SC	Self-Consistent
CNT	Carbon Nanotube
SWCNT	Single-Wall Carbon Nanotube
MWCNT	Multi-Wall Carbon Nanotube

Chapter 1

Theoretical Methods

The work presented in this thesis employed a number of major theoretical and computational techniques widely used in computational physics today, ranging from the simple classical potential methods,[1] tight-binding (TB) models[2] to the rather complicated and computationally challenging *ab initio* methods.[3,4] In the first chapter, we give an introduction to each of these methods first, and then we concentrate on *ab initio* total-energy pseudopotential methods, which are extensively used in this work. With the knowledge of conventional *ab initio* methods, we move the discussion to a new local-orbital-based *ab initio* method, which scales essentially linearly with the number of atoms in simulation system. The order-N method helps greatly in large-scale quantum transport simulations in Chapter 4. Comparison among the theoretical methods used in this thesis is summarized at the end of this chapter.

Atomistic simulations and quantum mechanical calculations are becoming increasingly important in both academic and industrial research. During the last three decades, a variety of simulation methods has emerged, each having particular strengths and limitations. Among these methods, classical potential, tight-binding and *ab initio* are the big three methods widely used in solid state physics with great success and popularity. The appropriate combination of the three methods can provide the needed power to explore most problems, in terms of capability, accuracy, system size and computational efficiency. We will look at the three methods one by one in the following sections.

1.1 Empirical classical potential models

The classical potential method is also often called classical molecular dynamics or force-field models[5] in the chemistry and biochemistry communities. It treats the simulated system as a collection of atoms without internal structure, interacting with each other through a potential function. The interaction potential used in the simulation may be generic or realistic. A generic potential attempts to capture the essential physics while the structure of the potential is simplified as much as possible. Generic potentials are used to study phenomena and models. A realistic potential attempts to describe real materials under specific conditions. Realistic potentials may be either accurate or approximate. The realistic potential total energy methods are interpolation schemes used to calculate the energy from parameters fitted from experiments or from first principle calculations.
At the simplest level, the interaction potential consists of a sum of pair-wise interaction energies. At the intermediate level, the energy for the system is a sum of energies of the atoms, but the energy cannot be decomposed into a sum of pair-wise interaction energies. For the most complicated case, the energy of the system cannot be decomposed into a sum of pairwise interaction energies or even as a sum of energies for the individual atoms.

Since classical potential method neglects quantum behavior, it greatly simplifies the system's degree of freedom and interactions. This makes it possible to be applied

extensively to model systems containing thousands to millions of atoms. It is the first and sometime the only method to observe the dynamics for a large system or for a long time period. However, in situations where quantum mechanical effects are significant, classical potentials can easily fail to or may produce meaningless or misleading results. For example, pair potentials fail to stabilize tetrahedral structures such as diamond and zincblende, since the directional covalent bonding in these systems is primarily determined by quantum mechanical effects. The transferability of the classical potential method is thus quite limited. Furthermore, it highly depends on the specific model and potential parameters.

1.2 Tight-binding total energy methods

The tight-binding model is originated from the idea of linear combination of atomic orbits (LCAO) by Bloch,[6] and is developed by Slater and Koster.[7] Compared with simple classical potential and complicated *ab initio* methods, the tight-binding method takes an intermediate step towards modeling materials that takes into account quantum mechanical effects without too much computational effort. The derivation of tight-binding formalism starts from quantum mechanics. The idea is to write the eigenstates of the Hamiltonian in atomic-like basis set, $\{\phi_{i\alpha}\}$, and replacing the exact many-body Hamiltonian operator with a parameterized Hamiltonian matrix. The basis set is not, in general, explicitly constructed, but it is atomic-like in which it has the same symmetry properties as the atomic orbitals. In general only a small number of basis functions are used, and those

functions are roughly corresponding to the atomic orbitals in the energy range of interest. For instance, when modeling carbon nanotube, only 2s and 2p orbits are considered, and even the p_z π bonding orbital is enough under some circumstances.

1.2.1 Orthogonal tight-binding methods

The modern orthogonal tight-binding scheme was developed by Slater and Koster, who derived the first detailed tight-binding formalism for band structure calculations. In our presentation, we shall assume periodic boundary conditions (PBC) for simplicity. However, It is straightforward to extend the TB formalism to finite-size systems.

Denoting an atomic orbital $n = (\tau, \alpha)$ at unit cell i as $\phi_n(r - r_\tau - R_i)$, we have the Bloch sum

$$\phi_{nk} = \frac{1}{\sqrt{N}} \sum_{i=1}^{N} e^{ik(r_\tau + R_i)} \phi_n(r - r_\tau - R_i)$$

where the sum is over the atoms in equivalent positions in all unit cells in the crystal. τ is the atomic index in the unit cell and α specifies the atomic orbitals of atom τ. For example, in the diamond structure, τ=1,2 and α =s, p_x, p_y, p_z. We may express the wavefunctions of the system as linear combinations of Bloch sums. However, the Bloch sum formed from atomic orbitals is not an ideal basis, since atomic orbitals at different sites may not be orthogonal to each other. It is more convenient to work in an orthogonal basis, the so-called Löwdin orbitals $\psi_n(r)$ which are formed by the reorthogonalization of atomic orbitals $\phi_n(r)$.[8] We shall assume that such a reorthogonalization is done and rewrite the Bloch sum as

$$\psi_{nk} = \frac{1}{\sqrt{N}} \sum_{i=1}^{N} e^{ik(r_\tau + R_i)} \psi_n (r - r_\tau - R_i) .$$

The Hamiltonian matrix element between two Bloch sums with the same k is

$$H_{n,n'}(k) = \sum_{i=1}^{N} e^{ik(r_\tau + R_i - r_{\tau'})} \left\langle \psi_n (r - r_\tau) \middle| H \middle| \psi_{n'} (r - r_{\tau'}) \right\rangle .$$

In the above equation, the sum has to be carried out over all unit cells in principle. In practice, one always assumes that the matrix element $\left\langle \psi_n \middle| H \middle| \psi_{n'} \right\rangle$ is short-ranged and decays to zero beyond some cut-off distance.[9,10,11] The matrix elements $\left\langle \psi_n \middle| H \middle| \psi_{n'} \right\rangle$ in the TB formalism are modeled by some empirical parameters which are either obtained by fitting experimental data or from the more accurate *ab initio* calculations. Eigenvalues and corresponding wavefunctions are then calculated by diagonalizing the Hamiltonian matrix H. This is the original Slater-Koster TB model.[7]

The Slater-Koster TB formalism computes only the band energies. For atomistic simulations, the total energy of the system must also be derived. Chadi proposed that the total energy of a system in the TB framework can be written as band structure energy plus a sum of pairwise repulsive potentials

$$E_{tot} = E_{bs} + E_{rep} = \sum_{i \in occupied} \varepsilon_i + \sum_{i,j} U(| r_i - r_j |) .$$

This is consistent with the local density approximation (LDA) expression for the total energy, which is as a sum of the band energy and various potential contributions. The idea that the terms in the total energy that are not included in the single-electron band energy can be approximated by a sum of pair terms is of great importance and is almost universally applied.[2] However, the reason for doing it is still not clear. The force acting on an atom in the TB formalism contains two terms, one arising from the band structure

energy E_{bs} and the other from the repulsive potential energy.

In this work, we chose a TB model developed by Xu,[12] and used the parameters for carbon systems given in Xu's paper. Xu's model is derived from GSP[11] model which accurately describes silicon. In Xu's model, the total energy of the system is written as

$$E_{tot} = E_{bs} + E_{rep},$$

where E_{bs} is the sum of electronic eigenvalues over all occupied electronic states, and the short-ranged repulsive energy E_{rep} is given by

$$E_{rep} = \sum_i f[\sum_j \phi(r_{ij})],$$

where $\phi(r_{ij})$ is a pairwise potential between atoms i and j, and f is a functional expressed as 4th-order polynomial with argument $\sum_j \phi(r_{ij})$. The pair potential $\phi(r_{ij})$ is defined as

$$\phi(r) = \phi_0 (\frac{d_0}{r})^m e^{m[-(\frac{r}{d_c})^{m_c} + (\frac{d_0}{d_c})^{m_c}]}.$$

The electronic eigenvalues are obtained by diagonalizing an empirical tight-binding Hamiltonian H_{TB}. The off-diagonal elements of H_{TB} are given by a set of orthogonal sp^3 two-center hopping parameters, $V_{ss\sigma}$, $V_{sp\sigma}$, $V_{pp\sigma}$ and $V_{pp\pi}$, scaled with interatomic separation r as a function s(r). The on-site elements are the atomic orbital energies of the corresponding atom. The scaling function s(r) for the Slater-Koster Hamilton matrix elements has the form

$$s(r) = (\frac{r_0}{r})^n e^{n[-(\frac{r}{r_c})^{n_c} + (\frac{r_0}{r_c})^{n_c}]}.$$

All the parameters in the above functions were determined by fitting first-principles LDA results of energy versus nearest-neighbor interatomic separation for different carbon

polytypes, i.e., diamond, graphite, linear chain, simple cubic and face-centered cubic structures. In order to facilitate molecular-dynamics simulations, the scaling functions s(r) and $\phi(r)$ were required to go smoothly to zero at some designed cut-off distance. This is achieved by replacing the tail of s(r) with a third-order polynomial $t_s(r-r_1)$ whose coefficients are determined by requiring the connection of s(r) and $t_s(r)$ at r_1 ($r_1 \leq r_m$) to be smooth up to the first derivative, and $t_s(r)$ and its first derivative to be zero at the matching point r_m. The same procedure is used to determine $t_\phi(r - d_1)$ which replaces the tail of $\phi(r)$. Our results show that Xu's model can describe carbon nanotubes' mechanical behavior successfully up to fairly high strains.

1.2.2 Nonorthogonal tight-binding methods

The orthogonal TB model described in the above section is conceptually simple and computationally efficient. However, it has serious limitations. The assumption that an orthogonal set of orbitals can be constructed from the nonorthogonal atomic orbitals by the Löwdin procedure is not always valid, i.e., an orthogonal transformation is valid only for a single configuration of the system. Furthermore, the Löwdin orbitals are usually more extended than the nonorthogonal atomic orbitals, which make the Hamiltonian matrix element $\langle \psi_n | H | \psi_{n'} \rangle$ long-ranged. The usually short-ranged TB parameterization is therefore not expected to work well across different environments. Failure to properly account for the overlap effects is probably the main reason for the lack of transferability of orthogonal TB models, although other issues such as the two-center approximation of

the Hamiltonian matrix element, the pairwise repulsive potentials, and the lack of self-consistency are also important factors. The transferability can be improved somewhat by including a wider range of empirical data; however, the improvement is limited and not systematic. Dorantes-Dávila and Pastor *et al.*[13,14] have proposed an iterative scheme to incorporate in an orthogonal TB framework the effects of the overlaps of atomic orbitals. A different approach is the so-called nonorthogonal TB model. As its name tells, this approach eliminates the assumption of orthogonality so that most of the drawbacks associated with this assumption can be overcome. (The effect of neglecting the nonorthogonality of the basis has been investigated by Mirabella *et al.*[15] and Mckinnon and Choy.)[16]

In the nonorthogonal TB model, one has to solve the generalized eigenvalue problem

$$(H - E_i S)\psi_i = 0 ,$$

where S is the overlap matrix between TB orbits,

$$S_{n,n'} = \int \phi_n(r)\phi_{n'}(r)dr$$

and ϕ are nonorthogonal atomic TB orbitals as opposed to the orthogonalized Löwdin orbitals ψ. The repulsive part of the total energy is usually assumed to be pairwise as in the orthogonal TB models. The on-site (diagonal) Hamiltonian matrix elements are usually taken as the atomic ionization potentials of the corresponding orbitals, i.e., $H_{n,n'} = \varepsilon_n$, and the off-diagonal elements can be determined using Mulliken approximation,[17,18]

$$H_{n,n'} = \frac{1}{2}K(\varepsilon_n + \varepsilon_{n'})S_{n,n'} ,$$

where K is an adjustable parameter, or by other means.[19,20]

1.3 Ab initio methods

1.3.1 Approximations

Since the establishment of quantum mechanics in the first two decades in last century,[21] scientists believe that most of low-energy physics, chemistry and biology can be explained by the quantum mechanics of electrons and ions. But how to apply quantum mechanics to the atomic system remained a challenge for a long time. Different theoretical methods derived from quantum mechanics have been proposed and developed over decades. Among them, the *ab initio* methods or first principle methods stand out because these methods require only a specification of the ions (by their atomic number). Due to the fact that many ground state physical properties are related to total energies or to differences between total energies, direct calculation of total energy from quantum mechanics becomes the heart of quantum simulations. Among all the first-principles methods, the total-energy pseudopotential method[22,23] stands alone. With the most efficient numerical algorithms, total-energy pseudopotential method can handle systems with up to a thousand atoms and even include nonzero temperatures for the first time in quantum simulations. In *ab initio* methods, it is especially important to apply approximations in the calculation of the system's quantum-mechanical total energy in order to make the calculation efficient and therefore possible.

Because of the large difference in masses between the electrons and the nuclei and

the fact that the forces on the particles are of the similar magnitude, the electrons respond essentially instantaneously to the motion of the nuclei. Thus the nuclei can be treated adiabatically, leading to a separation of electronic and nuclear coordinates in the many-body wave function. This is the so-called Born-Oppenheimer approximation. This "adiabatic principle" reduces the many-body problem to the solution of the dynamics of the electrons in some frozen-in configuration of the nuclei.

Even with this simplification, the many-body problem remains formidable. Further simplifications, however, can be introduced that allow the total-energy calculations to be performed accurately and efficiently. These include density-functional theory (DFT) to model the electron-electron interactions, pseudopotential theory to model the electron-ion interactions, periodic supercells to unify the modeling of periodic and aperiodic systems, and iterative minimization techniques to relax the ionic and electronic coordinates.

The following is a brief description of these essential concepts:

(i) Density-functional theory allows one, in principle, to map exactly the problem of a strongly interacting electron gas (in the presence of nuclei) onto that of a single particle moving in an effective nonlocal potential. Although this potential is not known precisely, local approximations to it work remarkably well.

(ii) Pseudopotential theory,[24] allows one to replace the strong electron-ion potential with a much weaker potential-- a pseudopotential—that describes all the salient features of a valence electron moving through the solid, including relativistic effects. Thus the original solid is now replaced by pseudo-valence electrons and pseudo-ion cores. These pseudoelectrons experience exactly the same potential outside the core region as

the original electrons but have a much weaker potential inside the core region. The fact that the potential is weaker is crucial, however, because it makes the solution of the Schrödinger equation much simpler by allowing expansion of the wave functions in a relatively small set of plane waves.

(iii) The supercell[25] approximation allows one to deal with aperiodic configurations of atoms within the framework of Bloch's theorem. One simply constructs a large unit cell containing the configuration in question and repeats it periodically throughout space. By studying the properties of the system for larger and larger unit cells, one can gauge the importance of the induced periodicity and systematically filter it out.

In general, taking these approximations in quantum simulations is a process to reduce the number of the degrees of freedom and the complexity of interactions of the system. These processes can be illustrated in the following chart:

Approximations in *ab initio* calculations

Starting simulation system: strongly Interacting Ions and electrons

Born_Oppenheimer approximation

Separate ions and electrons: All electrons in "frozen-in" nuclar configuration

Density-functional theory (DFT and LDA)

Map the strongly interacting many-electron system to equivalent non-interacting pseudo-electron system

Pseudopotential theory

Separate valence and core electrons: valence electrons are considered explicitly

Bloch's theorem, k-point sampling and supercell

Approximate an infinite system with a unit cell with finite number of atoms with periodic boundary conditions

Solving DFT equations by iterative methods

Physically meaningful results are achieved at the end of convergence

1.3.2 Density functional theory

The most difficult problem in many-body electron system is how to deal with the exchange and correlation interactions. The pioneering work done by Hohenberg and Kohn (1964)[26] and Kohn and Sham (1965)[27] proposed a simple method for describing the effects of exchange and correlation in an electron gas. After many extremely successful applications, their theory became the foundation of most *ab initio* calculations. Hohenberg and Kohn proved that the total energy, including exchange and correlation energy of an electron gas, is a unique functional of the electron density. The minimum value of the total-energy functional is the ground-state energy of the system, and the density that yields this minimum value is the exact single-particle ground-state density. Kohn and Sham then showed how it is possible, formally, to replace the many-electron problem by an exactly equivalent set of self-consistent one-electron equations. This is the so called density-functional theory (DFT).

DFT is best described by Hohenberg and Kohn (1964) and Kohn and Sham (1965) Theorems:

Theorem 1: The all-electron many-body ground state wavefunction $\psi(r_1,...,r_n)$ of a system of N interacting electrons is a unique functional of the electronic density n(r). The immediate consequence of this theorem is that all physically measurable quantities based on the electronic structure are in fact unique functionals of the electronic ground state density alone. Note that in general there is no closed expression for these

functionals.

Theorem 2: For all N-representable densities n(r), the one that minimizes the energy functional with a given external potential is the ground state density, i.e., the density that corresponds to the solution of the Schrödinger equation.

The proof of these remarkable theorems, which were later generalized by Levy,[28] turns out to be rather simple. Here we follow here the derivation in a review article by Jones and Gunnarsson.[29]

Let's denote n(r) as "N-representable" densities, i.e., those that can be obtained from some antisymmetric many-electron wavefunction Ψ

$$n(r) = N\int | \Psi(r, r_2, r_3, ..., r_N) |^2 \; dr_2 ... dr_N ,$$

assuming that the wavefunction Ψ is normalized to one. The Hamiltonian for N electrons moving in an external potential V^{ext} is

$$H = T + V^{ee} + \sum_{i=1}^{N} V^{ext}(r_i)$$

where T is the kinetic energy operator and V_{ee} is electron-electron interaction. Levy defined a functional

$$F(n) = \min_{\Psi \to n} < \Psi \mid T + V^{ee} \mid \Psi >,$$

where the minimization is taken over all wavefunctions Ψ that give the charge density n(r). For all N-representable n(r), the two basic theorems of DFT are

$$E(n) \equiv \int V^{ext}(r) n(r) dr + F(n) \geq E_0 ,$$
$$\int V^{ext}(r) n_0(r) dr + F(n_0) = E_0 ,$$

where E_0 is the ground state energy, and n_0 is the ground state charge density.

The variational principle above is obvious since, for any N-representable density n, the n-body wavefunction that minimizes the functional F(n), denoted as $\Psi^n_{\min}$, is a superposition of the n-body eigenfunctions of the system. Therefore, the expectation value of $\Psi^n_{\min}$, namely, E(n), should be higher or equal to the ground state energy.

If Ψ_0 is the ground state wavefunction, n_0 is the ground state charge density, and $\Psi^{n0}_{\min}$ is the wavefunction that minimizes the functional $F(n_0)$, we have from the definition of the ground state,

$$E_0 \equiv \left\langle \Psi_0 \left| V^{ext} + T + V^{ee} \right| \Psi_0 \right\rangle \le \left\langle \Psi^{n_0}_{\min} \left| V^{ext} + T + V^{ee} \right| \Psi^{n_0}_{\min} \right\rangle$$

Since

$$\left\langle \Psi_0 \left| V^{ext} \right| \Psi_0 \right\rangle = \left\langle \Psi^{n_0}_{\min} \left| V^{ext} \right| \Psi^{n_0}_{\min} \right\rangle = \int V^{ext}(r) n_0(r) dr ,$$

we have

$$\left\langle \Psi_0 \left| T + V^{ee} \right| \Psi_0 \right\rangle \le \left\langle \Psi^{n_0}_{\min} \left| T + V^{ee} \right| \Psi^{n_0}_{\min} \right\rangle$$

On the other hand, the definition of functional F(n) yields

$$\left\langle \Psi^{n_0}_{\min} \left| T + V^{ee} \right| \Psi^{n_0}_{\min} \right\rangle \le \left\langle \Psi_0 \left| T + V^{ee} \right| \Psi_0 \right\rangle$$

This can be true only if

$$\left\langle \Psi_0 \left| T + V^{ee} \right| \Psi_0 \right\rangle = \left\langle \Psi^{n_0}_{\min} \left| T + V^{ee} \right| \Psi^{n_0}_{\min} \right\rangle$$

Therefore, we have

$$
\begin{aligned}
E_0 &\equiv \left\langle \Psi_0 \left| V^{ext} + T + V^{ee} \right| \Psi_0 \right\rangle \\
&= \int V_{ext}(r) n_0(r) dr + \left\langle \Psi_0 \left| T + V^{ee} \right| \Psi_0 \right\rangle \\
&= \int V_{ext}(r) n_0(r) dr + \left\langle \Psi_{\min}^{n_0} \left| T + V^{ee} \right| \Psi_{\min}^{n_0} \right\rangle \\
&= \int V_{ext}(r) n_0(r) dr + F(n_0)
\end{aligned}
$$

This completes the proof of the two basic theorems of DFT.

The DFT of Hohenberg and Kohn states that knowledge of the ground state charge density $n_0(r)$ of a system is, in principle, sufficient to calculate any of its ground state properties, provided that the exact functionals are known. For example, to calculate the ground state energy, one simply needs to know the functional form of F(n). However, obtaining an exact functional F(n) is obviously impossible. Kohn and Sham proposed the simplest, and surprisingly, the most successful approximation to the energy functional, which is now known as the local density approximation (LDA).

Kohn and Sham first partitioned the functional F(n) into three parts:

$$F(n) = T^0(n) + E^h(n) + E^{xc}(n),$$

where $T^0(n)$ is the kinetic energy of a system of noninteracting electrons with density n(r), $E^h(n)$ is the Hartree energy and $E^{xc}(n)$ is the exchange-correlation energy functional, which remains to be approximated. They assumed a slowly varying charge density n(r) and approximated the exchange-correlation energy functional as

$$E^{xc}(n) = \int n(r) \varepsilon^{xc}(n(r)) dr,$$

where ε^{xc} is the exchange-correlation energy per electron of a uniform electron gas of density n(r). This expression can be regarded as the leading term of a more general Taylor expansion of $E^{xc}(n)$:

$$E^{xc}(n) = \int n(r) \varepsilon^{xc}(n(r)) dr + \int \varepsilon_2^{xc}(n) \left| \nabla n \right|^2 dr + \cdots$$

Therefore, in the slowly varying charge density limit, the above expression becomes exact. By expanding the charge density n(r) as a sum of single-particle-like densities

$$n(r) = \sum_{i=1}^{N} | \phi_i(r) |^2$$

and applying the variational principle to the energy functional, they reached a set of one-particle Schödinger equations, known as Kohn-Sham equations (in atomic units):

$$[-\frac{1}{2}\nabla^2 + V^H(r) + V^{xc}(r)]\phi_i(r) = \varepsilon_i \phi_i(r)$$

,

where $V^{xc}(r) = \frac{d(n\varepsilon^{xc}(n))}{dn}$ is the exchange-correlation potential and

$$V^H(r) = \int \frac{n(r')}{|r - r'|} dr'$$

is the Hartree potential. The total energy of the system is

$$E = \sum_{i=1}^{N} \varepsilon_i - \frac{1}{2}\int \frac{n(r)n(r')}{|r - r'|} dr dr' + \int n(r)[\varepsilon^{xc}(n(r)) - V^{xc}(n(r))]dr$$

The Kohn-Sham equations have to be solved self-consistently. Furthermore, the exchange-correlation energy ε^{xc} (n) needs to be approximated.

In their original work, Kohn and Sham did not expect this simple approximation of exchange and correlation energy, namely LDA, to work well for real systems, commenting “we do not expect an accurate description of the chemical bonding” (by LDA). Therefore, it is a rather surprising fact that LDA has been applied to a wide variety of systems with great success. In some cases, the charge densities are not at all slowly varying. LDA is computationally efficient, because it assumes that the exchange-correlations energy functional is purely local and it appears to give a single well-defined global minimum for the energy of a non-spin-polarized system of electrons. Several

existing parameterizations[30,27,31,32] for the exchange-correlation energy of a homogenrous electron gas often lead to similar results. Apart from the fact that LDA (somewhat unexpectedly) produces rather accurate ground state properties of materials, the Kohn-Sham orbitals ϕ_i, which are introduced as a variational basis and have no obvious connection with the quasiparticle wavefunctions, turn out to be surprisingly close to the latter. Also, the Kohn-Sham eigenvalues ε_i are often very close to quasiparticle energies. Therefore, although DFT was formally established for computing ground state properties, it is now almost universally applied to calculate and interpret the electronic structure of materials. However, one should bear in mind that calculations of the excited state properties are actually out of the scope of the DFT, and neither LDA nor DFT should be blamed for any inconsistency between the DFT (LDA) eigenvalues and the experimentally measured quasiparticle excitation energies. In fact, there are well known problems. For example, LDA usually underestimates the band gap of semiconductors and insulators. For simple metals such as lithium and sodium, LDA gives free-electron-like valence band widths which are typically 20~30% wider than the experimental ones.

1.3.3 Pseudopotential Approximation

The density functional theory, particularly the Kohn-Sham LDA form, greatly simplifies the calculation of materials properties and significantly reduces the computational effort. Many of the modern computational methods in solid state physics are based on DFT. However, if we need to represent highly localized wavefunctions such

as those of core electrons, calculation load will be formidable due to the very strong core electron interaction. Fortunately, the pseudopotential concepts introduced by Fermi[33] and Hellmann[34] make it possible to accurately describe the properties of materials without dealing explicitly with the core electrons.

The cancellation theorem derived from the orthogonalized plane wave (OPW) formalism by Philips and Kleinman[35,36] is very helpful in understanding the pseudopotential concepts. This theorem demonstrates that the requirement that valence states should be orthogonal to the core states effectively provides a repulsive potential for the valence states. If this effective repulsive potential is added to the attractive potential in the core region, they almost cancel out, leaving a relatively weak net potential or pseudopotential. In the OPW methods, the valence state wavefunctions are expressed as the sum of a smooth wavefunction ϕ and a sum over core states ϕ_c,

$$|\Psi\rangle = |\phi\rangle + \sum_c \alpha_c |\phi_c\rangle$$

with the requirement that the valence states Ψ are orthogonal to the core states ϕ_c, which yields

$$|\Psi\rangle = |\phi\rangle - \sum_c |\phi_c\rangle\langle\phi_c\|\phi\rangle \qquad (1)$$

We now find an effective Schrödinger equation that ϕ satisfies, assuming that Ψ satisfies the following Schrödinger equation

$$H|\Psi\rangle = (T + V_c)|\Psi\rangle = E|\Psi\rangle,$$

where T is the kinetic energy operator and V_c denotes the attractive core potential. Substituting (1) into the above equation, we have

$$H|\phi\rangle + \sum_c (E - E_c)|\phi_c\rangle\langle\phi_c\|\phi\rangle = E|\phi\rangle$$

where E_c is the energy of the core state ϕ_c, i.e.,

$$H|\phi_c\rangle = E_c|\phi_c\rangle .$$

The HK equation can be rewritten as

$$(T + V^{ps})|\phi\rangle = E|\phi\rangle$$

where the pseudopotential V^{ps} is

$$V^{ps} = V_c + \sum_c (E - E_c)|\phi_c\rangle\langle\phi_c| .$$

It can be shown that the second term of V_{ps} is strongly repulsive potential which almost cancels the strongly attractive core potential V_c, leaving a weak net pseudopotential. Fig 1.1 shows the typical shape of pseudopotentials. Compared with the -1/r behavior of the Coulomb potential, the potentials shown in the figure are much softer.

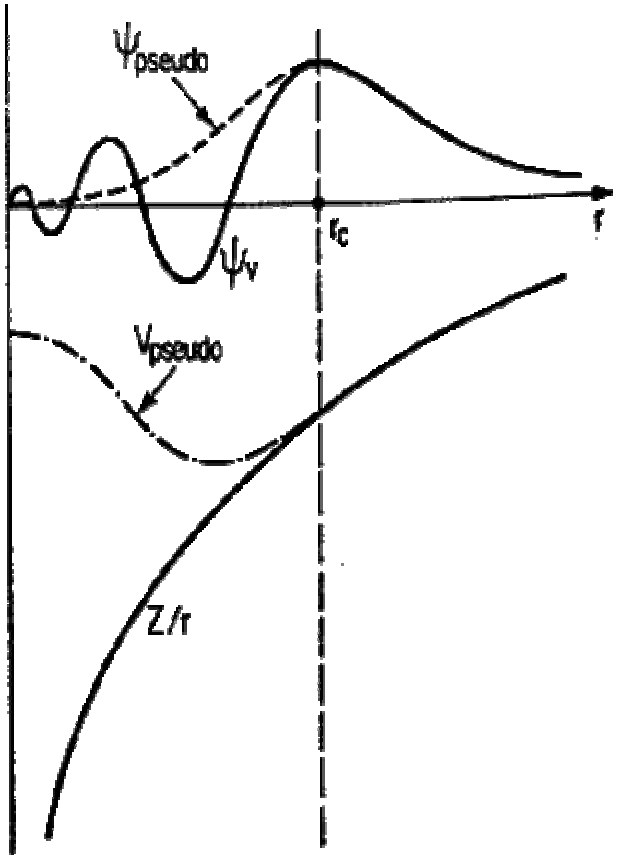

Figure 1 Pseudo-potential: A schematic illustration of all-electron (solid lines) and pseudo-(dashed lines) potentials and their corresponding wavefunctions. The radius at which all-electron and pseudopotential values match is R_{cutoff} . From Ref. 3.

A pseudopotential is constructed in such a way that it matches the true potential outside a given radius, designated the core radius. Similarly, each pseudo-wavefunction must match the corresponding true wavefunction beyond this distance. The eigenvalues calculated with the pseudopotential must be identical to the all-electron eigenvalues. In addition, for most modern pseudopotentials, the charge densities obtained outside the core region must be identical to the true charge density. Thus, the integral of the squared amplitudes of the real and pseudowavefunctions over the core region must be identical.

This is why these pseudopotentials are called norm-conserving. The resulting pseudo-wavefunction contains no radial nodes.

The atomic properties of the element must be preserved, including phase shifts due to scattering from the core. These phase shifts will be different for different angular momentum states and so, in general, a pseudopotential must be non-local, with projectors for different angular momentum components. The pseudopotential is often represented using the form,

$$V = V_{loc} + \sum_{l,m} (V_l - V_{loc}) \hat{P}_{l,m} \quad ,$$

where $\hat{P}_{l,m}$ are the projectors which project the electronic wavefunctions onto the eigenfunctions of different angular momentum states. The choice of V_{loc} is arbitrary and if it is made equal to one of the V_l, this avoids the need for the corresponding set of angular momentum projectors. Work has also been done by Lee *et al.* on further reducing the number of projectors needed. The evaluation of the non-local potential in reciprocal space requires a computational time which is proportional to the cube of the system size. The projections may be carried out in real-space instead, using the method of Kleinman-Bylander *et al.*,[36] which reduces the computational cost to the order of the system size squared.

Pseudopotentials are constructed using an *ab initio* procedure. The `true' wavefunctions are calculated for an isolated atom using an all-electron DFT approach. The resulting valence wavefunctions are then modified in the core region to remove the

oscillations while obeying the norm-conservation constraint. The Schrödinger equation is then inverted to find the pseudopotential which will reproduce the pseudowavefunctions. This procedure produces a pseudopotential which can be transferred between widely varying systems. This contrasts with semi-empirical potentials, which are constructed to describe a particular atomic environment and may not be simply transferred to different environments.

The Kleinman and Bylander (KB)[36] approach is almost widely used in pseudopotential constructions. It provides an elegant prescription that transforms the semi-nonlocal pseudopotential into a fully separable, truly nonlocal pseudopotential, with only O(N) operations in the real-space formalism when applied on the wavefuntions. However, in the use of KB nonlocal pseudopotentials, extra care need to be paid to avoid unphysical "ghost" states at energies below or near those of the physical states. These "ghosts" are artifacts of the KB potential in which the nodeless pseudo-wavefunctions need not be the lowest possible eigenstates, unlike in the case of the semi-local form. Those ghost states can be avoided by properly chosing the local pseudopotential component and/or varing the cutoff radii R_l^{cut} of the pseudopotentials.

1.3.4 Iterative minimization techniques in *ab initio* method

It has been demonstrated that the total-energy pseudopotential technique gives accurate and reliable values for total energies of solids. However, as described above, the power of the pseudopotential method is severely restricted when using conventional

matrix diagonalization techniques to solve for the Kohn-Sham eigenstates. Alternative techniques are proposed for minimizing the Kohn-Sham energy functional and lead to the same self-consistent Kohn-Sham eigenstates and eigenvalues as conventional matrix diagonalization. The popular Car-Parrinello molecular-dynamics (CPMD) method,[37,38] conjugate-gradients methods[39,40,41] and other approaches allow pseudopotential calculations to be performed for much larger systems than was possible using conventional matrix diagonalization methods. They allow, for the first time, tractable *ab initio* quantum-mechanical simulations to be performed for systems at nonzero temperatures and large systems with noble and transition-metal atoms and first-row elements such as oxygen.[42,43,44,45,46] Furthermore, for real-space grid based solutions, multi-grid preconditioning techniques[47,48,49,50] can provide systematic acceleration to reduce the number of iterations.

In the Car-Parrinello scheme, the Kohn-Sham energy functional E is a function of the wavefunction coefficients. These coefficients can be regarded as the coordinates of a classical "particle". To minimize the Kohn-Sham energy functional, these "particles" are given a kinetic energy, and the system is gradually cooled until the set of coordinates reaches the values that minimize the KS energy functional. Thus the problem of solving for the Kohn-Sham eigenstates is reduced to one of solving for a set of classical equations of motion. It should be emphasized, however, that the KS energy functional is physically meaningful quantum mechanically only when the coefficients take the final minimization values.

The Car-Parrinello method makes use of the following lagrangian for the electronic system:

$$L_{cp} = \sum_i \mu_i \left\langle \dot{\psi}_i \middle\| \dot{\psi}_i \right\rangle + \frac{1}{2}\sum_I M_I R_I^2 + \frac{1}{2}\sum_n \beta \dot{\alpha}_n - E[\{\psi_i\},\{R_I\},\{\alpha_n\}],$$

where μ_i are fictious masses associated with the electronic wave functions, E is the Kohn-Sham energy functional, R_I is the position of ion I, M_I is the mass of ion I, and β is the fictitious mass associated with coordinates α_n, which define the size and shape of the unit cell. The second and third terms are only needed in relaxation of the ionic system. Here we just fix the unit cell for simplification. To generate trajectories for the ionic and electronic degrees of freedom via the coupled set of equations of motion

$$M_I \ddot{R}_I = -\frac{\partial E[\{\psi_i\},\{R_I\},\{\alpha_n\}]}{\partial R_I},$$

$$\mu_i \left| \ddot{\psi}_i \right\rangle = -\frac{\partial E[\{\psi_i\},\{R_I\}]}{\partial \left\langle \psi_i \right|}.$$

The electronic wave functions are subject to the constraints of orthonormality, $\int \psi_i^*(r)\psi_j(r)d^3r = \delta_{ij}$. These constraints are incorporated in the molecular-dynamics Lagrangian by using the method of Lagrange multipliers. When damping is applied to the equations of motion, the ionic coordinates and wavefunctions will evolve to the values that minimize the Kohn-Sham energy functional. The total computational time for the processes in CPMD is dominated by the $N_B N_{PW}^2$, improved from the N_{PW}^3 scaling in conventional matrix diagonalization techniques.

To perform a total-energy pseudopotential calculation it is necessary to find the electronic states that minimize the Kohn-Sham energy functional. Searching for the self-consistent Kohn-Sham Hamiltonian indirectly can lead to instabilities. These instabilities would not be encountered if the Kohn-Sham energy functional were minimized directly because the Kohn-Sham energy functional normally has a single well-defined energy minimum. The methods of steepest descents (SD)[51] and conjugate-gradients (CG)[51] are two general direct minimization techniques to perform total-energy pseudopotential calculations tractably and stably for large systems. The conjugate-gradients method is particularly powerful.

In the steepest descents (SD) method, a linear search is done along the direction of steepest descent at any given configuration. The location of the lowest value of the testing function (KS energy) on the searching line is the start point for next search. In some implementations, a fixed step is used instead of linear search. The size of the SD step needs to be chosen carefully in order to enhance convergence. Iteratively, the system gets closer and closer to the minimum of the testing function.

It might seem surprising that there can be a better direction to minimize a function than the one in which the function decreases most rapidly. By making each minimization step independent of each other, the conjugate-gradients method avoids reintroduction of errors proportional to the previous gradient. The initial direction is taken to be the negative of the gradient at the starting point. A subsequent conjugate direction is then constructed from a linear combination the new gradient and the previous direction that minimized the energy functional. It is interesting that the current gradient and the

previous direction vector would maintain all of the information necessary to include minimization over all previous directions in a multidimensional space. The proof that directions generated in this manner are indeed conjugate is the important result of the conjugate-gradients derivation. The precise search direction d^i generated by the CG method is obtained from the following algorithm:

$$d^m = g^m + \gamma^m d^{m-1}$$
$$\gamma^m = \frac{g^m \bullet g^m}{g^{m-1} \bullet g^{m-1}} \qquad \text{with} \quad \gamma^1 = 0.$$

The following is a complete description of CG method for a symmetric and positive-definite matrix A and function $f(x) = 1/2x^T Ax - b^T x + c$ minimized by the solution to Ax=b.

$$d_0 = r_0 = b - Ax_0,$$
$$\alpha_i = \frac{r_i^T r_i}{d_i^T A d_i},$$
$$x_{i+1} = x_i + \alpha_i d_i,$$
$$r_{i+1} = r_i - \alpha_i A d_i,$$
$$\beta_{i+1} = \frac{r_{i+1}^T r_{i+1}}{r_i^T r_i},$$
$$d_{i+1} = r_{i+1} + \beta_{i+1} A d_i.$$

In practice, accumulated floating point roundoff error causes the residual to gradually lose accuracy, and cancellation error causes the search vectors to lose A-orthogonality. This suggests restarting after certain iteration steps. Iterative methods like CG are well-suited for use with sparse matrices, which is the case for solving KS equations. Although the CG method performs much better for an ill-conditioned matrix than SD does, it is critical to the speed of convergence to find a good preconditioner, especially in the real-

space grid-based local orbital order-N method that we will describe later. In mathematics, parallel multilevel preconditioners for discretized partial differential equations can systematically speed-up the convergence rate in self-consistent calculations. For real-space grid-based *ab initio* methods, we have used multiple grids with varying resolutions to solve the KS equations and the Poisson equation. The solution is obtained on a grid fine enough to accurately represent the pseudopotentials and the electronic wavefunctions. If the solution error is expanded in a Fourier series, it may be shown that iterations on any given grid level will quickly reduce the components of the error with wavelengths comparable to the grid spacing but are ineffective in reducing the components with wavelengths large relative to the grid spacing. The solution is to treat the lower frequency components on a sequence of auxiliary grids with progressively larger grid spacing, where the remaining errors appear as high frequency components. This procedure provides excellent preconditioning for all length scales present in a system and leads to very rapid convergence rates.

1.3.5 Real-space grid-based order-N DFT method

Traditional total-energy pseudopotential calculations scale at least cubically with the number of atoms in the simulation system. In practice, an *ab initio* simulation for a system with hundreds of atoms becomes slow even with today's massively parallel supercomputers. In this work, to study the complicated electronic structure of carbon nanotube composites, we need a new *ab initio* method with better scaling with the

number of atoms in the system. Following our group's early exploration in order-N DFT method, we found that the real-space grid-based nonorthogonal orbital DFT method[52] proposed by J. L. Fattebert and J. Bernholc scales roughly linearly, and with proper implementation and improvements, this method could push *ab initio* calculation well beyond a thousand atoms. The basic idea is to use the uniqueness of the representation of the ground state of the system in terms of nonorthogonal orbitals to find an optimally localized basis that accurately describes the energetics. This approach is real-space oriented, and it is more general in the basis set. In our implementation, it includes a multigrid preconditioner and it allows for unoccupied or partially occupied states, which substantially accelerates convergence. The local orbital description is also very helpful in orbital-based quantum transport calculations proposed by Marco Buongiorno Nardelli.

Here is the basis-invariant matrix formulation of this order-N method derived by J. L. Fattebert et al. We start from minimizing the Hohenberg-Kohn total energy functional

$$E_t = \sum_{i=1}^{N} f_i \langle \psi_i | -\frac{1}{2}\nabla^2 | \psi_i \rangle + \frac{1}{2}\int V_H(\rho)\rho dr + \frac{1}{2}\int V_{ion}(\rho)\rho dr + E_{xc}[\rho] + E_{ion-ion}$$

for N-occupied orbitals in the system, each represented by a one-body wave function ψ_i, with the electron charge density $\rho(r) = \sum_{i=1}^{N} f_i |\psi_i(r)|^2$. The first term represents the kinetic energy, the second the electrostatic repulsion due to the classical Hartree potential $V_H(r) = \int \frac{\rho(r')}{|r-r'|} dr'$, the third the interactions of the electrons with all the nuclei, the fourth the exchange and correlation contributions, and the fifth the classical electrostatic interactions between all nuclei.

The orbitals ψ_i satisfy that Kohn-Sham equations

$$H\psi_i = [-\frac{1}{2}\nabla^2 + V_{ion} + V_H(\rho) + \mu_{xc}(\rho)]\psi_i = \varepsilon_i\psi_i$$

which must be solved self-consistently for the N lowest eigenvalues ε_i, while imposing the orthonormality constraints $\langle \psi_i | \psi_j \rangle = \delta_{ij}$. $\mu_{xc} = \frac{\delta E_{xc}[\rho]}{\delta\rho}$ is the exchange and correlation potential. Kleinman-Bylander (KB) form norm-conserving nonlocal pseudopotentials are used for V_{ion} in our simulations.

Using the KS equations, the total energy expression is easily rewritten as

$$E_t = \sum_{i=1}^{N} f_i\varepsilon_i - \frac{1}{2}\int V_H(\rho)\rho dr - \frac{1}{2}\int \mu_{xc}(\rho)\rho dr + E_{xc}[\rho] + E_{ion-ion}$$

Consider a trial basis of normalized functions, $\{\phi_1, ..., \phi_N\}$, which will define the subspace of the occupied orbitals. This basis will be refined by iterative updates, and at convergence will accurately describe the true Kohn-Sham ground state of the system. In order to derive basis-invariant expressions for the updates, it is convenient to use matrix notations. The functions ϕ_j will thus be written as columns of a matrix Φ

$$\Phi = (\phi_1 ....., \phi_N).$$

An orthonormal basis of approximate eigenfunctions (Ritz functions) can be obtained by a diagonalization in this subspace of dimension *N* (Ritz procedure). We denote by *C* the $N \times N$ matrix that transforms into the basis of orthonormal Ritz functions,

$$\mathbf{\Psi} = (\psi_1, ..., \psi_N) = \mathbf{\Phi C}. \qquad \textbf{(2)}$$

This matrix satisfies

$$CC^T = S^{-1},$$

where $S = \Phi^T\Phi$, is the overlap matrix.

In the following, for an operator A we will use the notation

$$A^{(\Psi)} = \Psi^T A \Psi,$$

$$A^{(\Phi)} = \Phi^T A \Phi,$$

We then have the relation

$$A^{(\Psi)} = C^T A^{(\Phi)} C \ .$$

In order for Eq. (2) to define a transformation to a Ritz basis, C has to be a solution of the generalized symmetric eigenvalue program.

$$\mathrm{H}^{(\Phi)} C = SC\Lambda \qquad (3)$$

where Λ is the diagonal,real $N \times N$ matrix that satisfies

$$\Lambda = \Psi^T H \Psi \ ,$$

The matrix C can actually be decomposed as a product $\mathrm{C} = \mathrm{G}^{-\mathrm{T}}\mathrm{U}$, where G is the Cholesky factorization of S,

$$S = GG^T,$$

and U is an orthogonal matrix. Knowing G, the generalized eigenvalue problem (3) is reduced to a standard symmetric eigenvalue problem

$$G^{-1} H^{(\Phi)} \ G^{-T} U = U\Lambda \qquad (4)$$

In the basis Ψ, the *SD* directions, along which the energy functional decreases at the fastest rate, are easy to compute. They are given by the negative residuals of the Kohn-Sham equations, with the current potential kept fixed, and can be expressed as the $N \times M$ matrix

$$\mathrm{D}^{(\Psi)} = \Psi \Lambda - H\Psi \ , \qquad (5)$$

which satisfies the relation

$$\Psi^T D^{(\Psi)} = 0.$$

In the following, we consider a SD algorithm with a linear preconditioning operator K. Without preconditioning, the convergence rate can be very slow, especially if M » N. For real-space finite difference (FD) discretizations, the multigrid preconditioner greatly improves the convergence. Introducing a pseudo-time-step η, Ψ should thus be corrected at each step according to

$$\Psi^{new} = \Psi + \eta K D^{(\Psi)} .$$

Note that in this algorithm all the trial wave functions are updated simultaneously. Without preconditioning, η has to be very small (for numerical stability reasons) and the convergence can be very slow.

For optimum convergence rate, it is important to preserve the true descent direction when working with the nonorthogonal orbitals Φ. This direction can differ substantially from the derivative with respect to $\phi_j(\mathbf{r})$, when the basis Φ is highly nonorthogonal. Since the direction $D^{(\Psi)}$ is easy to compute, the simplest way to obtain the SD direction in the basis Φ is to use the matrix C

$$D^{(\Phi)} = D^{(\Psi)} C^{-1} = (\Psi \Lambda - H \Psi) C^{-1} = \Phi\Theta - H\Phi , \qquad (6)$$

where

$$\Theta = S^{-1} H^{(\Phi)}, \qquad (7)$$

The preconditioned steepest descent (PSD) direction in the nonorthogonal basis is thus

$$\delta\Phi = K D^{(\Psi)} C^{-1} = K(\Phi\Theta - H\Phi), \qquad (8)$$

and the basis Φ is updated according to $\Phi^{new} = \Phi + \eta\delta\Phi$. In the particular case K = Identity, equation (8) is equivalent to the result given by Galli and Parrinello.[53] Note that $\delta\Phi$ does not depend on C and therefore does not require the solution of the eigenvalue problem (3).

Note that since by definition

$$\Phi^{new} = (\Psi + \eta K D^{(\Psi)}) C^{-1} = \Psi^{new} C^{-1},$$

the same subspace is generated at each iteration, independently of the basis, if the same pseudotime step is used. In our simulations, we found that although the above SD works well for some systems, its convergence rate becomes bad for large system. When the conjugate gradient (CG) method is used, the system converges faster. In actual calculations, the basis functions Φ are corrected at each iteration using the PSD directions. A new electronic density $\rho(\mathbf{r})$ is then generated according to

$$\rho(\mathbf{r}) = 2 \sum_{j,k=1}^{N} (\mathrm{S}^{-1})_{jk} \phi_j(\mathbf{r}) \phi_k(\mathbf{r}),$$

as well as the new Hartree and exchange-correlation potentials. However, the old and the new potentials are then mixed linearly. The KS functional is minimized iteratively until self consistency is achieved.

At each step, the kinetic energy E_{kin} can be evaluated in the nonorthogonal basis Φ as

$$E_{kin} = 2 \sum_{j,k=1}^{N} (\mathrm{S}^{-1})_{jk} \langle \phi_j | \tfrac{1}{2} \nabla^2 | \phi_k \rangle .$$

To obtain the ground-state energy E_t, the first term on the right-hand side of Eq. (3) can be expressed as a trace of Θ ,

$$\sum_{j=1}^{N} 2\varepsilon_j = 2Tr(\Lambda) = 2Tr(\Theta).$$

The inclusion of unoccupied or partially occupied orbitals can substantially enhance the convergence rate. The PSD algorithm described above can be used to improve the trial subspace of N computed orbitals, regardless whether they are occupied or empty. In the

computation of the electron density and the total energy, however, one needs to account for the occupations. Therefore, a density-matrix formalism is introduced in the nonorthogonal basis. The details are in the ref. 52.

In our simulations, the new method does show nearly linear behavior. However, due to the local orbital representation and the related stability problem, the method's convergence rate and its adaptation to modern supercomputer architectures has to be treated carefully for applications to large systems. However, quantum simulations are always being improved. We believe the order-N real-space grid-based DFT method will bring *ab initio* simulations to a new level.

1.4 Summary

With the fundamental laws of quantum mechanics and statistical physics, the availability of high-performance computers and continuing improvements in simulation methods and software, the goal of predicting materials from first principles seems to be closer than ever. Yet the complexity of real materials with their intriguing interplay between chemical composition, atomic arrangements, microstructures, and macroscopic behavior seems to elude any attempt of using first-principles as "one size fits all" solution. In this dissertation, we investigate not only the stability of topological defects of different carbon nanotubes under large strain, but also the energetics of the activation process. This challenging problem needed appropriately combined different simulation

techniques with correct physical intuition. Here I provide an assessment of the major atomistic simulation methods we used.

Major atomistic simulation methods

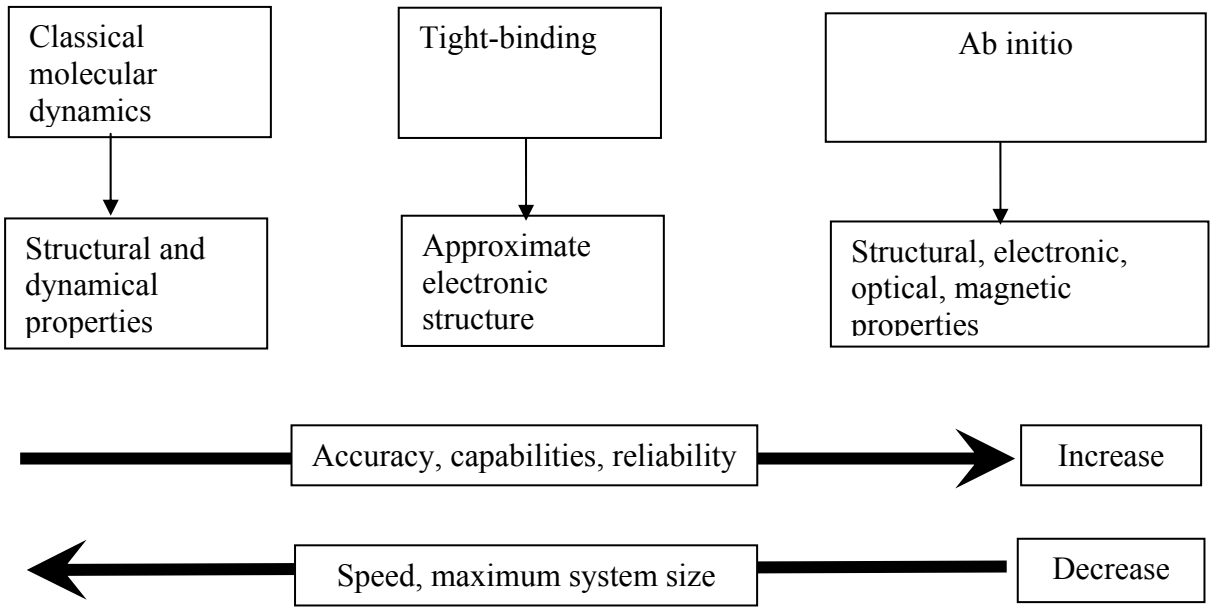

For the three atomistic simulation methods, each has particular strengths and limitations. As the fastest method, the classical molecular dynamics (MD) is the best for the first stage of fast modeling of dynamical processes. However, one needs to be aware that the generality and transferability of classicals potential cannot be taken for granted and that the results obtained from MD need to be carefully evaluated. Usually, classical molecular dynamics results need be confirmed by more reliable methods. Furthermore, classical molecular dynamics cannot give any information about the electronic structure.

The Brenner-Tersoff[54,55] model used in our carbon nanotube study shows good accuracy for stable structures, but it fails to give reliable description in the energetics of defect activation processes. The TB methods described in the previous section represents the early efforts to incorporate realistic quantum mechanics effects into a model Hamiltonian. Although TB models have been successfully applied to a number of systems and have advantages over empirical potentials, there are limitations. For example, it is very difficult to obtain TB parameters for systems containing more than two species. Also, there are few accurate and transferable TB parameters available. TB parameters constructed by fitting data from one phase might not be readily applied to the study of other phases or the transitions among them, i.e., TB parameters are not very transferable. Although nonorthogonal TB schemes improve the transferability of TB by relaxing the orthogonallity assumption to some extent, the improvements are limited by their empirical nature. Finally, the assumption that the Hamiltonian matrix does not depend upon the distribution of electrons creates severe difficulties when dealing with systems where charge transfer is important (this problem is partially addressed by the so-called self-consistent tight binding (SCTB) methods[56]). The Xu's model[12] has had great success in simulating carbon materials. We found that this model can yield very good agreement for topological defect formation in carbon nanotubes. The deviation from *ab initio* results increases with strain, which can be due to the fact that the parameterization has obtained for largely unstretched carbon materials. Because it is not easy for tight binding method to handle systems with different elements and charge transfer, we did not use tight binding in the study of electric transport properties of carbon nanotube-metal cluster assemblies.

As the most accurate and powerful technique, *ab initio* method is extensively used in this work. To simulate large carbon nanotube systems, a new linear scaling local orbital based *ab initio* methodology is used. The pseudopotential total energy calculations based on DFT are applicable to all elements and produce very reliable and accurate description of the behavior of atomic systems, provided that appropriate basis sets and pseudopentials are used. However, in LDA binding energies are typically overestimated. This is because LDA tends to overemphasize the metallic character and one needs to be careful in the interpretation of the density functional one-electron energies. Although the inclusion of gradient corrections for the exchange-correlation term (GGA[57,58,59,60]) does not always provide systematic improvement over LDA, it does perform better where LDA does not.

The accessible system size of *ab initio* method is limited to about 1000 atoms and the tractable time scale is in the range of picoseconds even with today's supercomputers. At this time, significant effort is dedicated to the development of order-N methods. Although such methods have been successfully demonstrated, the pre-factor is too large to make them competitive with conventional methods for systems with less than one hundred atoms. There are also quite a few implementation issues which must be addressed to make order-N methods routine.

Chapter 2

Carbon Nanotube Systems

2.1 Introduction to carbon nanotubes

Carbon is rather special element which can form very flexible bonding networks, for example, one dimensional (sp^1) carbon chains and rings, two dimensional sp^2 layered structures such as graphite, and three dimensional (sp^3) diamond. In contrast, no sp^2 silicon phases are known to exist. It is remarkable that both graphite and diamond are very stable. (Under normal conditions, graphite is just slightly more stable than diamond.) Whereas graphite is a zero-gap semimetal and has the highest in-plane stiffness, diamond is a wide-gap insulator and is the hardest three-dimensional material available so far. Diamond and graphite also have the highest thermal conductivity of known materials in 3-D and 2-D. However, the story of carbon seems to not have been completed yet. The discovery of the nearly spherical molecule C_{60}[61] and related fullerenes,[62,63,64] and the subsequent synthesis of carbon tubules,[67] now referred to as carbon nanotubes, have inspired another wave of research into carbon-based materials. There are already a couple excellent reviews and books on various forms of carbon materials (for example, carbon fibers, glassy carbon, carbon black, amorphous carbon, etc.).[65,66]

In 1991, Iijima[67] reported the synthesis of a new type of carbon structure, "needle-like tubes", using an arc-discharge vaporization method similar to that used for fullerene

synthesis. The original carbon tubules consisted of several (ranging from 2 to about 50) concentric graphitic shells, and had diameters of a few nanometers. These multi-shelled carbon microtubules are now called multi-walled carbon nanotubes. Single-walled carbon nanotubes were later synthesized by arc-discharge vaporization,[68,69,70] laser ablation of carbon targets[71] and chemical vapor deposition (CVD)[72,73,74] in the presence of catalysts (Fe, Ni, or Co). With the progress in synthesis of carbon nanotubes,[75,76,77,78,79,80,81,82,83] carbon nanotube can be obtained in high quality and quantity at reasonable cost.

From a purely geometrical perspective, a sigle-walled carbon nanotube (SWCNT) is formed by rolling up a graphene (single-layer graphite) sheet into a cylinder (see the following Figures).

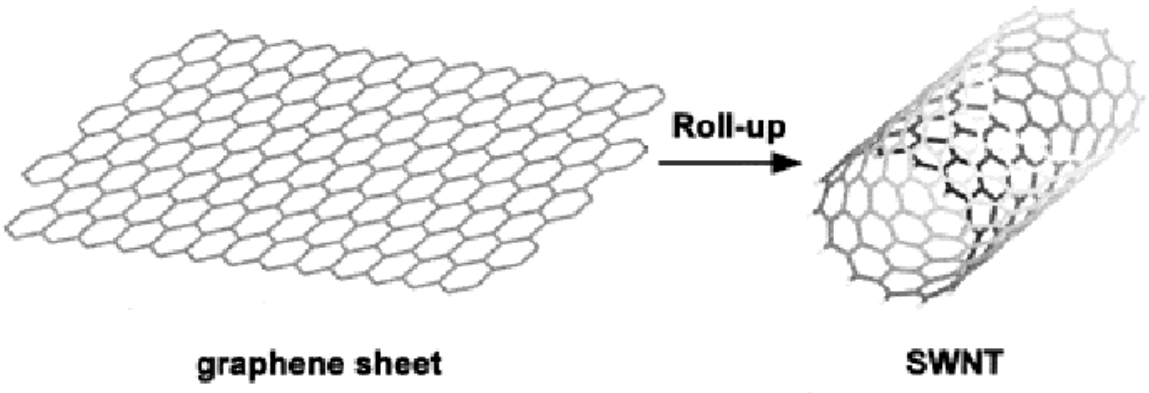

Figure 2 Graphene sheet is rolled up into carbon nanotube.

Please note that it is not likely that carbon nanotubes are formed this way in real experiments. In fact, the nucleation and growth mechanisms of carbon nanotubes are still an active research topic.[84,85,86,87,88,89] The followings are some experimental TEM images of carbon nanotubes.

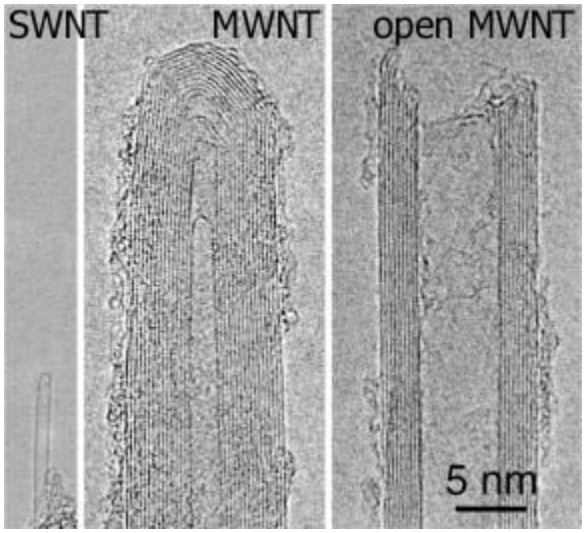

Figure 3 SWNT and MWNT TEM images

A single-walled carbon nanotube is uniquely specified by its circumferential vector $C=nA_1+mA_2$ as shown in Fig. 2.2, where A_1 and A_2 are the unit vectors of graphite, and n and m are integers. A single-walled carbon nanotube with $C=n\mathbf{a}_1+m\mathbf{a}_2$ is called an (n, m) nanotube.

Two particular classes of single-walled nanotubes are worth mentioning. One is (n, 0), also called zigzag nanotubes, and the other is (n, n) or armchair nanotubes. Generic (n, m) nanotubes are called chiral nanotubes. In contrast, (n, 0) and (n, n) nanotubes are achiral (non-chiral). The diameters d of an (m, n) nanotube can be calculated by

$$d = \sqrt{3}a_{C-C}\frac{\sqrt{m^2+mn+n^2}}{\pi},$$

where $a_{c\text{-}c}$ is the C-C bond length. The chiral angle (or wrapping angle) θ is

$$\theta = \tan^{-1}[\frac{\sqrt{3}m}{m+2n}].$$

For (n, 0) nanotubes, θ is zero. However, the wrapping angle of (n, n) nanotubes is not zero but $\theta = 30^o$. A double walled nanotube can be specified by indexing each of the

walls starting from inner layer, for example, (5, 5)@(10, 10).

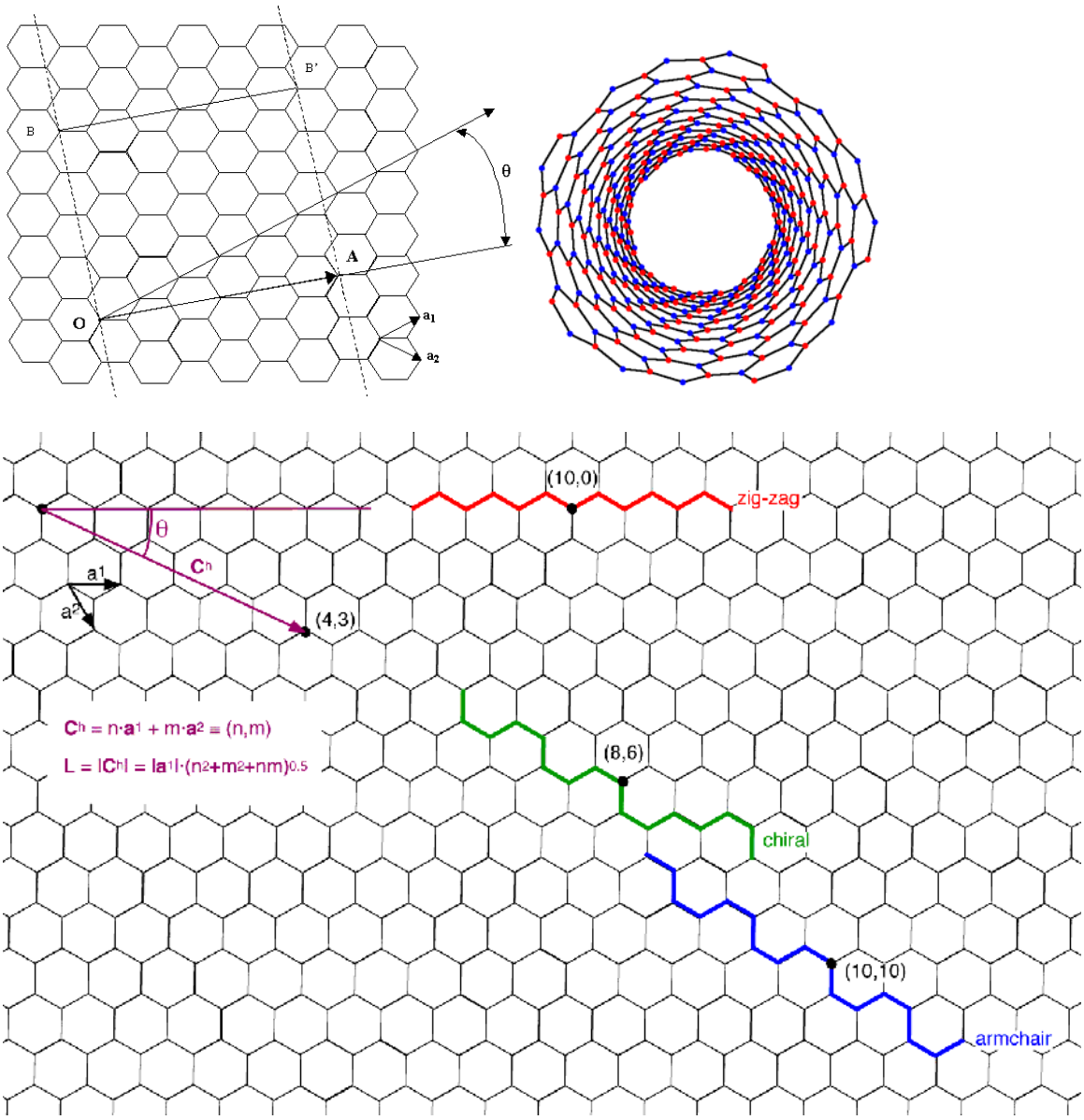

Figure 4 **Structure specification of single-walled carbon nanotubes. The circumferential vectors shown in the figure correspond to different types of carbon nanotubes.**

Carbon nanotubes have been the focus of intensive research for the past decade due to their unique properties that could have impact on broad areas of science and technology.[90,91] Many times, carbon nanotubes have been on the cover pages for major

research journals, such as Science and Nature. The following table summarizes carbon nanotube's main properties and potential applications.

Properties	Potential Applications
Mechanical	
- extraordinary elastic properties[92]: 1000 times stronger than steel (stress) and 6 times lighter. - High flexibility of carbon nanotubes,[93,94,95,96,97] unlike carbon fibers - Expansion by charge injection	- Reinforcement for composite materials,[98,99] space elevator... - Actuators[100] - Atomic Force Microscope (AFM) tips[101,102]
Electrical	
- Metallic or semiconductor, depends on chirality[103,104,105] - Ideal ballistic conductor[106] - Easily tunable field emission[107,108]	- Conductive plastics (Electro Magnetic Shielding, protection against antistatic discharges) - Electronical nanocomponents (diodes, transistors...) - Electron gun, field emission display[109], lamps,[110] x-ray[111] or microwave[112,113] generators

Physico-chemical	
- High specific area (several hundreds of sqm per gram) - Cavities enabling molecular storage inside the carbon nanotube - High thermal stability (up to 1500 °C under vaccum) - Chemical treatment on carbon nanotubes, enabling attachment of other molecules to carbon nanotubes	- Hydrogen[114]/Lithium[115] storage for fuel cell or batteries - Nanometric test tubes[116] - Electronical nanocomponents, material protection.... - Chemical sensors and biosensors, ultra fast gas detection...

The study of carbon nanotubes has greatly broadened the scope of nanoscience and nanotechnology. Carbon nanotube stimulated non-stop discoveries of new materials, like carbon nanohorns[117], peapods, boron nitride nanotubes, etc. Carbon nanotube is becoming the popular icon nano-materials.

2.2 Superior Mechanical Properties

Due to the extremely strong sp^2 bonding network of carbon and the flexible orbital hybridization of carbon atoms, both SWCNT and MWCNT have been seen to exhibit unique mechanical properties: carbon nanotubes are not only quite stiff and exceptionally strong, but also very flexible to mechanical stimuli. With the fact that carbon is a very

light element and CNTs are hollow structures, CNTs make ultra-light and super strong materials unmatched by any other known material.

It is by now well established in theoretical and experimental studies that carbon nanotubes have a high Young's modulus and high tensile strength. However, the published mechanical parameters can be very confusing, because some groups use the total occupied cross-sectional area and others use the much smaller van der Waals area for defining Young's modulus and tensile strength. Using the total area per nanotube in a nanotube bundle for normalizing the applied force to obtain the applied stress, Gao *et al*[118] calculated the Young's modulus for an individual (10,10) nanotube as ~0.64 TPa, which is consistent with experiment measurements by Yu *et al.*[119] Up to now the measured elastic limit for tensile strain is ~5.8% before breaking.[119,120] Using the measured in-plane Young's modulus of graphite 1.06 TPa, this would lead to an even greater strength per NT wall than that of silicon carbide nanorods (~53 GPa).[121] Yu *et al* also measured Young's modulus under tensile loading MWCNTs, obtaining 270 to 950 GPa.[122] In another experiment, Lourie and Wagner[123] used micro-Raman spectroscopy to measure the compressive deformation of a nanotube embedded in an epoxy matrix. For SWCNT, they obtained a Young's modulus of 2.8-3.6 TPa, while for MWCNT, they measured 1.7-2.4 TPa. Early theoretical predictions[124,92] of Young's modulus, assuming a thickness of 0.34nm for the nanotube, are in the range of 1.5 to 5.0 TPa (in-plane modulus of graphite 1.06 TPa). In the very early energetics analysis of CNTs, using elastic theory, Tibbetts[125] pointed out that the strain energy of the nanotube is proportional to $1/R^2$ (where R is the radius of the CNT). Soon after the discovery of CNT, Robertson et al examined the energetics and elastic properties of SWCNTs with radii less

than 0.9 nm using both Brenner's potential and first-principles total energy methods. Their results showed a consistent linear proportionality to $1/R^2$ of the strain energy, which implies that small deformation beam theory is still valid even for the small radius limit. Gao et al carried out a similar study on SWCNTs of larger radius (up to 17 nm) with a potential that is derived from quantum mechanics. A similar linear relation of the strain energy of $1/R^2$ was found, with Young's modulus from 640.30 GPa to 673.49 GPa. Yakobson et al compared particular molecular dynamics simulation results to the continuum shell model and thereby fitted both a value for Young's modulus (~5.5 TPa) and for the effective thickness of the CNTs (t=0.066 nm). Lu derived elastic properties of SWCNTs and MWCNTs using an empirical model in his MD simulation. A Young's modulus of ~ 1 TPa and a shear modulus of ~ 0.5 TPa were reported based on a simulated tensile test. (The product of shell thickness and Young's modulus is still equal to that of Ygraphite, i. e. $Y_h = Y_{graph} * c_{graph}$.) Lu also found from his simulation that factors such as chirality, radius and the number of walls have little effect on the value of Young's modulus. Similar results are obtained by other methods. Zhou et al estimated strain energy and Young's modulus based on electronic band theory. They computed the total energy by taking account of all occupied band electrons. The total energy was then decomposed into the rolling energy, the compressing or stretching energy and the bending energy. By fitting these three values with estimates based on the continuum elasticity theory, they obtained Young's modulus of 5.1 TPa for SWCNT having an effective wall thickness of 0.71 Å. Note that this is close to the estimate by Yakobson et al, since the rolling energy and stretching energy terms were also included in the shell theory that Yakobson et al used. In addition, the accuracy of the continuum estimate was

validated by the derivation of a similar linear relation of the strain energy to $1/R^2$. Although no agreement has been reached among these publications regarding the value of the Young's modulus at this moment, it should be pointed out that a single value of Young's modulus cannot be uniquely used to describe both tension/compression and bending behavior. The reason is that tension and compression are mainly governed by the in-plane σ-bond, while pure bending is affected mainly by the out-of-plane π bond. It may be expected that different values of elastic modulus should be obtained from these two different cases unless different definitions of the thickness are adopted, and that is one reason that accounts for the discrepancies described above. However, the main reason for the discrepancies is still due to different cross sections used in deriving the Young's modulus.

Direct observations, mostly using high-resolution TEM, have shown that carbon nanotubes can bend, twist, and kink without fracturing. When bent or twisted, the nanotubes appear to flatten in cross section. Local or global buckling can occur in both the axial and transversal direction. The first simulation of the bent nanotube was stimulated by the experimental observation of a kink of a bent nanotube in a high-resolution transmission electron microscope (HRTEM). Classical molecular dynamics simulations using a realistic many-body potential, namely the Brenner potential that reproduces the lattice constants, the binding energies, and the elastic constants of both graphite and diamond, reproduced well the overall shape of the bent nanotube and predicted that the bending is highly reversible. The first bucking pattern starts at a nominal compressive strain of 0.05. Buckling due to bending and torsion was demonstrated in Ref. [37, 60-62]. In the case of bending, the pattern is characterized by

the collapse of the cross-section in the middle of the tube, which confirms the experimental observations by Iijima et al and Ruoff et al, also used HRTEM, and by Wong et al, who used AFM. When the tube is under torsion, flattening of the tube, or equivalently a collapse of the cross-section, can occur due to the torsional load. Using a nanomanipulator, Falvo et al bent MWCNTs repeatedly through large angles without causing any permanent damage to the tube. Similar methods were used by Hertel et al to buckle MWCNTs due to large bending. Lourie et al captured the buckling of SWCNTs under compression and bending by embendding them into a polymeric film. Unlike the single kink seen by Iijima et al, the buckling pattern under bending was characterized by a set of local rippling modes.

The studies of the radial deformation of carbon nanotube have also yielded unexpected results. Ruoff et al were the first to discover that CNTs are not necessarily perfectly cylindrical. They observed partial flattening due to van der Waals forces in TEM images of two adjacent and aligned MWCNTs along the contact region. This encourages the guess that in an anisotropic physical environment, all CNTs are likely to be, at least to some degree, not perfectly cylindrical due to mechanical deformation. Tersoff and Ruoff studied the deformation pattern of SWCNTs in a close-packed crystal and concluded that rigid tubes with diameters smaller than 1 nm are less affected by the van der Waals attraction and hardly deform. But for diameters over 2.5 nm, the nanotubes flatten against each other and form a honeycomb-like structure. Similar geometry dependence on the tube radius was found in the study of isolated nanotubes by Gao et al using an energetics analysis. The flattening of larger diameter SWCNTs could have a profound effect on factors such as storage of molecular hydrogen in SWCNT crystals

comprised of large diameter tubes, if they can be made, because the interstitial void space is dramatically altered. Lopez et al have reported a HRTEM observation of polygonized SWCNTs in contact. Chopra et al observed fully collapsed MWCNTs with TEM and showed that the collapsed state can be energetically favorable for CNTs with certain critical radii and overall wall thicknesses.

It is interesting to speculate whether larger diameter SWCNTs would ever remain completely cylindrical in any environment. A nearly isotropic environment would be a liquid comprised of small molecules, or perhaps a homogeneous polymer comprised of relatively small monomers. However, because the CNTs have such small diameters, fluctuations are present in the environment on this length, locally destroying the time-averaged isotropy present at longer length scales, which may trigger collapse. Alternatively, if full collapse does not occur, the time-averaged state of such a CNT in a (time-averaged) isotropic environment might be perfectly cylindrical. Perhaps for this reason, CNTs might be capable of acting as probes of minute fluctuations in their surrounding (molecular) environment.

Shen et al conducted a radial indentation test of ~10 nm diameter MWCNTs with scanning probe microscopy. They observed deformability (up to 46%) of the tube and resilience to a significant compressive load (20 μN). The radial compressive elastic modulus was found to be a function of compressive ratios and ranged from 9.0 to 80.0 GPa. Yu et al performed a nano-indentation study by applying compressive force on individual MWCTs with the tip of an AFM cantilever in tapping-mode and demonstrated a deformability similar to that observed by Shen et al. They estimated the effective elastic modulus of a range of indented MWCNTs to be from 0.3 GPa to 4 GPa by using the

Hertzian contact model. Note that the difference between this effective elastic modulus and the elastic modulus from Shen et al is that the effective modulus refers to the elastic response to deformation of an anisotropic indentation load applied in the radial direction.

Outstanding reversible volume compression of SWCNTs was observed by Chesnokov et al. The applied quasi-hydrostatic pressure was up to 3 GPa and the obtained volume compressibility was 0.0277 GPa^{-1}, which suggests the use of the CNT as energy-absorbing materials. The volume compressibility of SWCNTs having a diameter of 1.4 nm under hydrostatic pressure was also studied by Tang et al by in situ synchrotron x-ray diffraction. The studied SWCNT sample, which consisted primarily of SWCNT bundles and thus not individual or separated SWCNTs, showed linear elasticity under hydrostatic pressure up to 1.5 GPa at room temperature with a compressibility value of 0.024 GPa^{-1}, which is smaller than that of graphite (0.028 GPa^{-1}). However, the lattice structure of the SWCNT bundles became unstable for pressure beyond ~4 GPa, and was destroyed upon further increasing the pressure to 5 GPa.

A very subtle point that comes into the picture is the effect of interlayer interactions when CNTs collapse. This effect can produce some results that cannot be described by traditional mechanics. For instance, Yu et al observed fully collapsed MWCNT ribbons in the twisted configuration with TEM. One such cantilevered MWCNT ribbon had a twist present in the freestanding segment. Such a configuration cannot be accounted for by elastic theory since no external load (torque) is present to hold the MWCNT ribbon in place and in the twisted form. However, it is known that a difference of approximately 0.012 eV/atom in the interlayer binding energy of the AA and the AB stacking configurations exists for two rigid graphitic layers spaced 0.344 nm apart. The analysis

by Yu et al suggests that the elastic energy cost for the twist formation of this particular CNT ribbon can be partially compensated by achieving more favorable atomic registry. The observation of the existence of this freestanding twist in the ribbon thus suggests that there is an energy barrier keeping the twisted ribbon from untwisting. The mechanics analysis performed suggests that this twisted structure is metastable.

The strength of a CNT will likely depend on the distribution of defects and geometric factors. Breakage is due to bond breaking or plastic yielding. For perfect nanotubes, the strength could approach the theoretical limit due to the small density of the defects in nanotubes, unlike bulk graphite. However, determining the ultimate tensile strength of CNT is challenging for both theory and experiments study. We mentioned earlier that Yu et al has obtained tensile strain limit 5.3% for SWCNTs and 12% for MWCNTs in their tensile load experiments. Early classical MD simulations give quite high breaking tensile strain at 30% and 18.7%. When Buongiorno Nardelli et al studied the strain release mechanism under tensile loading using both classical and quantum molecular dynamics, they found that the bond rotation leading to the 5-7-7-5 defect formation is the major limiting factor for CNT strength. For tensile strain greater than about 5%, the formation of 5-7-7-5 defect occurs, which leads to further defects and eventual breakage. They also point out that CNTs can exhibit either brittle or ductile behavior depending on their chirality, diameter and temperature. Their result leads to a ductile-brittle domain map of CNTs. Our recent large-scale quantum calculations show that the activation barriers for the formation of 5-7-7-5 defects are much larger than estimated previously. Our theoretical results indicate a substantially greater resilience and strength, and show that the ultimate strength limit of carbon nanotubes has yet to be reached experimentally. The

details will be given in next chapter. In the end, it is also interesting to mention that the Stone-Wales transformation[126] (bond rotation) and subsequent ductile deformations change the chirality of the carbon nanotube, which creates carbon nanotube heterojunction useful for nanotube electronics.

As a brief summary, compared with their high rigidity in the axial direction, CNTs are observed to be much more compliant in the radial direction. Thus a CNT readily takes the form of a partially or fully collapsed nano-ribbon when the radius and wall thickness are in particular ranges, when either isolated in free space or in contact with a surface. A CNT may also locally flatten when surrounded, as for example occurs in SWCNT bundles. The ultimate strength of CNT has been investigated both theoretically and experimentally. The results indicate that CNT is the strongest material known.

2.3 Unique Electronic Structure and Extraordinary Transport Properties

The electronic properties of carbon nanotubes are fascinating. They can be either metallic or semiconducting depending on their wrapping index and diameter. The one-dimensional metal is stable under the so-called Peierls instability. The energy gap for a semiconductor nanotube, which is inversely proportional to its diameter, is directly observed by scanning tunneling microscopy measurements. The unique electronic structure of CNTs is directly related to the unique Fermi surface structure of graphene, combined with the quasi one-dimensional nature of carbon nanotubes and their rich geometries.

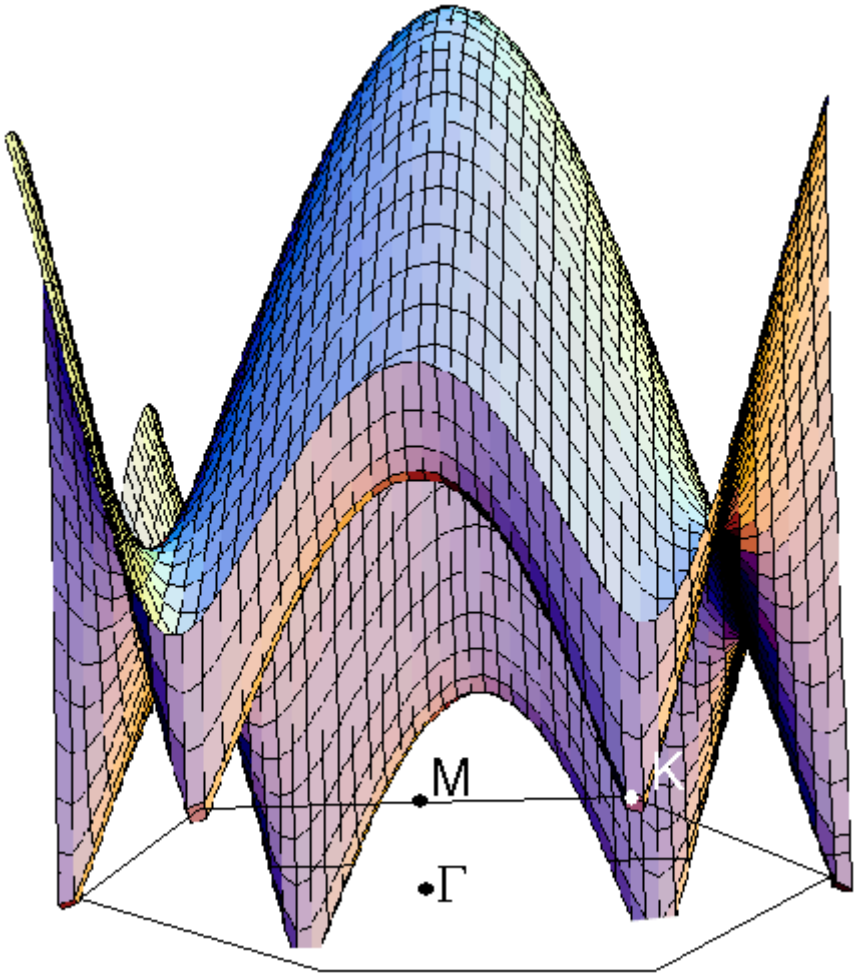

Figure 5 The energy dispersion relation of conduction band for a graphene sheet from equation (2.1) .

When the curvature effect is neglected, a single-walled carbon nanotube is considered as a graphene sheet rolled up into a cylinder. Therefore, the electronic structure of a SWCNT can be derived simply from that of two-dimensinal graphite. Figure 5 shows the energy dispersion relation of the π^* band for 2D graphene, considering only the p_z orbital of carbon. The commonly used energy dispersion relations for the electronic structure, considering only π and π^* band, of a graphene sheet is

$$E_{g2D}(k_x, k_y) = \pm t\{1 + 4\cos(\frac{\sqrt{3}k_x a}{2})\cos(\frac{k_y a}{2}) + 4\cos^2(\frac{k_y a}{2})\}^{\frac{1}{2}} \quad (2.1)$$

This relation shows that the π and π* bands meet at K point, which is the Fermi level. Therefore, the graphene sheet is a zero-gap semiconductor. Because of the periodic boundary condition along the circumferential direction C_h of the nanotube, the wave vector associated with the C_h direction is quantized. Since the wave vector associated with the direction of the translational vector T remains continuous, the allowed wave-vectors of carbon nanotube in the Brillouin zone become parallel lines. If the allowed lines pass the Fermi points K (corresponding to (n, m) nanotubes with n-m=3k, where k is an integer) the nanotube is metallic, otherwise it is semiconducting. Furthermore, since the dispersion of bonding and anti-bonding π bands around the Fermi-points is almost linear, the band gaps of the semiconducting nanotubes must have an envelop-function proportional to 1/r, where r is the tube diameter.

Although the above model is relatively simple, it works remarkably well, as has been discovered by comparisons with more complex models and experimental results. Even the 1/r behavior agrees well with experiment data. However, deviations from this simple model could arise when the mixing of in-plane σ and out-of-plane π orbitals increases in smaller diameter tubes. Early theoretical analysis show that a metallic carbon nanotube with n-m=3k and k≠0 is not stable against the perturbation induced by the curvature. A small band gap can occur in CNTs with radii less than 10 Å. For all metallic nanotubes with radii in the range of 2.5 to 10 Å except the armchair ones, the band gap decreases with the second power of the radius. For nanotubes with even smaller radii (such small diameter nanotubes have been synthesized recently inside MWCNTs or freestanding), the above model is no longer valid, and more fundamental, first-principles calculations are

needed to adequately describe their electronic properties. As a result, only (n, m) nanotubes with n=m remain metallic and free from the Peierls distortion at room temperature. (The Peierls distortion is strongly suppressed due to the rigidity of the sp^2 bonding network and the low density-of-states (DOS) of graphene near the Fermi level, therefore it can be easily destroyed by thermal effects.) Therefore, we have the following general rules for predicting the band gap of a carbon nanotube:

(1)if n = m, metallic,

(2)if n-m = 3k, where k is an integer and $k \neq 0$, a small gap semiconductor,

(3)if other, semiconducting with a band gap proportional to 1/r

The classification of SWCNT is for isolated tubes. Experimentally synthesized single-walled nanotubes usually tend to self-assemble as bundles called "ropes", due to van der Waals attraction. The inter-tube interactions introduce small pseudogaps in ropes of normally metallic tubes.

The electron transport behavior of carbon nanotube systems have been investigated comprehensively by different theoretical and experimental groups. From carbon nanotubes' electronic structure, armchair nanotubes have two extended electron bands crossing at the Fermi level. They are expected to behave as an ideal two-channel ballistic conductor with quantum conductance $2G_0$ ($G_0=2e^2/h\approx12.9K\Omega^{-1}$). The first experiment for carbon nanotubes to show quantized conductance was carried out by Frank et al[127]. They performed transport measurements between MWCNT and liquid mercury. Their results show that the MWCT is indeed a ballistic conductor with a single conductance quantum G_0. The difference between the measured and the theoretically predicted value of $2G_0$ is believed to be due either to a back-scattering mechanism from the metal[128] or to possible

inter-wall interactions within the multi-walled nanotubes.[129,130] The most recent measurements[131,132] on well-contacted metallic SWCNT show conductance values close to $2G_0$, which is consistent with band structure predictions. Recent theoretical analysis[133] of the conductance of MWCNT's shows that the tunneling current between states on different walls of a defect-free, infinitely long MWCNT is vanishingly small in general, which leads to quantization of the conductance of MWCNT's. The estimated generic interwall conductance is negligible compared to the intrawall ballistic conductance.

Structural deformations have significant effect on the electronic properties of nanotubes. It was shown that uniaxial stress, while not greatly affecting the band structure of armchair nanotubes, significantly alters the band structure of zigzag nanonotubes.[134] In fact, it is possible to use the simple analytical relations for the π band structure of graphene to derive the strain-induced changes in the electronic structure of nanotubes. The resulting relations predict a transition from semiconducting to metallic behavior as a function of strain and vice versa.[135] The same effects are obtained in more sophisticated calculations, with only some quantitative modifications. Tight-binding calculations, considering $sp^2\pi$ orbitals, shows that bent carbon nanotubes maintain their basic electrical properties even in the presence of large mechanical deformations.[136] The conductance sensitivities to mechanical deformations of chiral nanotubes may lead to switch or strain sensor applications.

Disorder effects also play an important role in 1D transport. White and Todorov[137] predicted that in contrast to normal metallic nanowires, where electrons can become localized due to the 1D nature of the system, conduction electrons in metallic armchair nanotubes experience an effective disorder averaged over the tube circumference, leading

to electron mean free paths that increase with nanotube diameter. This increase in mean free paths can lead to extraordinary ballistic transport properties and localization lengths of the order of hundreds of nanometers and more, which has been observed experimentally.[106] Similarly, theoretical studies by Anantram and Govindan[138] have revealed that weak uniform disorder does not radically alter the conductance near the band center. Both theoretical and experimental studies of the effects of disorder on the transport properties of metallic and semiconducting carbon nanotubes have been carried out by McEuen et al.[139] They verified that the mean free path is much larger in metallic tubes than in doped semiconducting tubes, and pointed out that this result can be understood theoretically if a long-rang disorder potential is present.

Experiments showed that molecule adsorption can dramatically changes the conductance of carbon-nanotube-based systems. For example, the electrical resistance of a semiconducting carbon nanotube can respond quickly and drastically to some gas molecules, such as NH_3, NO_2.[140] This makes the carbon nanotubes very promising as chemical/biological sensor in the size range of nanometer. Furthermore, oxygen adsorption can have substantial effect on transport measurements.[141,142,143,144,145] For specific defects and impurities in carbon nanotubes, they can introduce different scattering and bound states, and their effects on conductance can differ significantly. For example, B doping,[146] as expected, mainly affects the lower part of the metallic plateau, as does the vacancy, while N reduce conductance only in the upper part. A complex topological defect, the pentagon-heptagon pair, can reduce conductance at both ends of the plateau. In a recent experiment,[147] resonant electron scattering by structural defects has been observed, although it has not been possible to resolve the structure of the

defects.

Carbon nanotubes hold other important properties. For example, recent thermal transport measurements[148] of individual MWCNT at room temperature show that the carbon nanotubes' thermal conductivity (>3000 W/m•K) is greater than that of natural diamond and the basal plane of graphite (both about 2000 W/m•K). Therefore, carbon nanotube could be the best heat conductor in the world. Even superconductivity of carbon nanotubes was found at very low temperatures.[149,150] There are too many extraordinary electronic properties for carbon nanotubes to list here. Readers can consult the carbon nanotube books[66] and review articles[65] to find out more.

Chapter 3
Ultimate strength of Carbon nanotubes

The ultimate strength of carbon nanotubes is investigated by large-scale quantum calculations. While the formation energy of strain-induced topological defects determines the thermodynamic limits of the elastic response and of mechanical resistance to applied tension, it is found that the activation barriers for the formation of such defects are much larger than estimated previously. The theoretical results indicate a substantially greater resilience and strength, and show that the ultimate strength limit of carbon nanotubes has yet to be reached experimentally. Nanotubes are indeed the strongest material known. This chapter is organized in the following order: first, an introduction is given to the strain-introduced topological defect, 5-7-7-5 defect; second, theoretical methods used in our calculations are listed and discussed; in the third section, simulations results are presented and discussed; conclusions and implications of our theoretical investigation of carbon nanotube's ultimate strength are given at the end of this chapter.

3.1 Introduction

The mechanical response of carbon nanotube to severe deformations and strains has attracted much attention since their discovery[67] in 1991. As discussed in the last chapter, carbon nanotubes have already demonstrated exceptional mechanical properties: their excellent flexibility during bending has been observed experimentally and studied

theoretically. Nanotubes combine high stiffness with resilience and the ability to buckle and collapse in a reversible manner: even largely distorted configurations (axially compressed or twisted) can be due to elastic deformations with virtually no atomic defects involved. For these reasons, it has been suggested that carbon nanotubes could be promising candidates for a new generation of extremely light and superstrong fibers. Although it is conceptually simple, measuring the strength of nanotubes is very challenging in experiments, because it is difficult to grow and characterize defect-free nanotubes. Furthermore, the manipulation and measurement on such small objects, like nanotubes, is still far from trivial. Theoretically, investigating the ultimate strength of carbon nanotubes requires modeling of inherently mesascopic phenomena, such as plasticity and fracture, on a microscopic, atomistic level, which presents its own set of challenges. The current MD methods have severe limitations in time scale and system time, compared to what is used in experiments. Moreover, the reliability of widely used classical MD under conditions of large deformations, bonds breaking and reforming is questionable. However, the initial stages of strain-induced transformations can be deduced from quantum simulations and these results can be further refined by detailed investigations of the potential energy landscape.

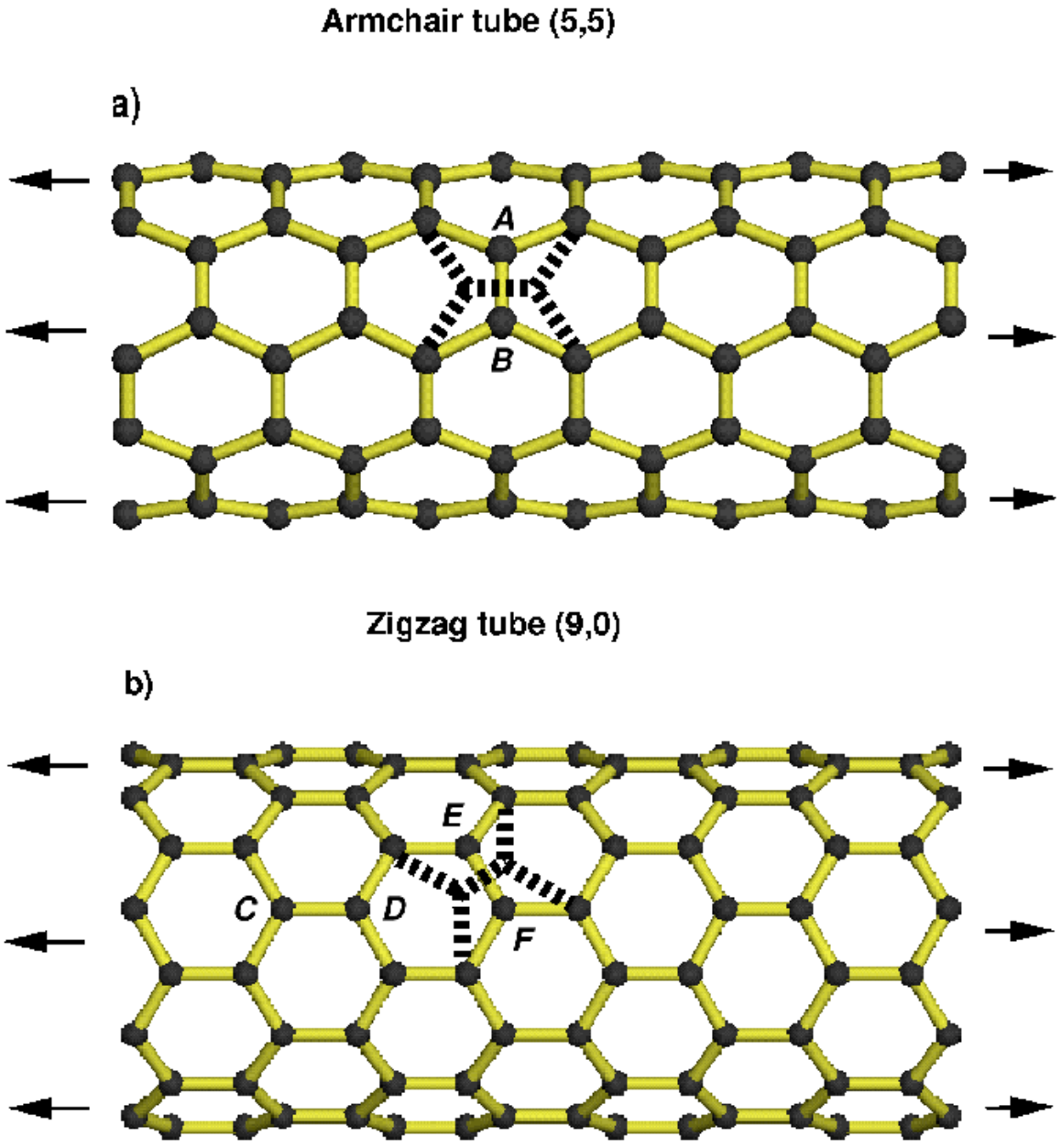

Figure 6 Bond rotation in strained carbon nanotubes: (a) Side view of a (5,5) armchair tube under axial strain: rotating the bond "AB" by 90° forms a (5-7-7-5) defect (dashed lines). (b) Side view of a (9,0) zigzag tube where the bond "EF" is responsible for the formation of the (5-7-7-5) defect (dashed lines).

It is now well established from simulations that beyond a certain value of the applied strain, around 5-6%, single-walled carbon nanotubes respond to the mechanical stimuli

via the spontaneous formation of topological defects.[151] Given the well-known 1 TPa Young modulus of graphite and a similar modulus of nanotubes[152] when rescaled to the density of graphite, the range of elastic response indicates enormous strength, unmatched by any other known material. It has also been shown that the mechanical response depends critically on tube geometry: zigzag tubes display a higher strain resistance than armchair tubes with same diameter.[153,154] Different orientations of the carbon bonds with respect to the strain axis in tubes of different symmetry lead to completely different scenarios: ductile or brittle behaviors can be observed in nanotubes of different indices under the same external conditions. Furthermore, the behavior of nanotubes under large tensile strain strongly depends on their symmetry and diameter[151,153] and the initial stages of strain-induced transformations can be explained by dislocation theory.[151,155] Recently, some of these predictions have been confirmed by two independent experiments: a number of carbon nanotubes do not exhibit mechanical failure and breakage up to about 5% strain.[119,120] These results, although important in addressing the problem of strength of carbon nanotubes, do not clearly determine the ultimate limit of their mechanical response, due to the quality of the samples and experimental limitations.

In order to determine the ultimate limits of the elastic response of strained carbon nanotubes, one needs to address not only the problem of the stability of topological defects under strain, but equally importantly, as it turns out, the energetics of the activation process.

We have therefore carried out extensive large-scale quantum calculations of the mechanism of formation of strain-induced topological defects in carbon nanotubes. Our results indicate that although the topological defects become energetically stable at

strains of the order of 5-6%, the activation barriers for their formation are extremely high, thus hindering the creation of such defects even at relatively large strains. This implies that ideal, structurally perfect single-walled carbon nanotubes should be kinetically stable and resist strains well beyond the 5% observed experimentally, and that they can indeed be considered the strongest materials known.

3.2 Methodology

The quantum simulations were carried out with a multigrid-based total-energy method that uses a real-space grid as the basis.[50] The Perdew-Zunger parameterization[32] of the Ceperley-Alder[156] exchange-correlation energy was used. The Kleinman-Bylander approach[36] was chosen to include non-local, norm-conserving pseudopotentials.[157,158,159] The convergence in both k-space sampling and grid size was carefully evaluated, and the supercell containing the nanotube included a large vacuum region of 7 Å, in order to ensure that the interactions between tube images can be neglected.

In order to extend this study to a larger class of systems and to overcome the computational limitations of calculations, we have carried out extensive comparisons between the accurate but expensive *ab initio* approach and the less computationally demanding semi-empirical tight-binding and classical molecular dynamics methods. The tight-binding and classical potential methods use adjustable parameters, which are usually determined by fitting experimental data for diamond, graphite and carbon chains in their equilibrium configurations. The reliability of these parameters for describing the properties of strained carbon nanotube structures needs thus to be verified by full

calculations. In the tight-binding simulations we used an orthogonal sp^3 model of Xu *et al*.[12] This model is able to describe the dynamical and elastic properties of nanotubes with good accuracy and reliability. The classical molecular dynamics calculations used the Tersoff-Brenner many-body potential to model interactions between carbon atoms.[54,55] Although this potential is not as accurate as the quantum-mechanical methods, it is very useful for qualitative and semi-quantitative estimates, and for explorations of the long-time evolution or of large portions of the potential energy landscape.

3.3 Computational Results and Discussion

From the geometrical point of view, carbon nanotubes are hollow cylinders consisting of "rolled-up" graphite sheets (graphene). Therefore, imposing an axial tension on a nanotube is geometrically similar to imposing a lateral strain on a graphene sheet. Since the hexagons comprising the nanotube walls have different orientations with respect to the tube axis (the so-called wrapping angle), an axial tension translates into lateral strains at varying angles in the graphene sheet. In particular, an axial strain in an armchair tube corresponds to a planar tension which is applied perpendicular to the bond marked ”AB” in Figure 6(a), while in a zigzag tube the planar tension is parallel to the bond indicated as “CD" in Figure 6(b). We call the tension in armchair tubes “transverse” while the one in zigzag tubes will be called ``longitudinal." The transverse tension finds natural release in a 90^o rotation of the “AB” bond in Figure 6(a). This rotation changes four neighboring hexagons into two pentagons and two heptagons, forming a pentagon-

heptagon-heptagon-pentagon (5-7-7-5) defect (indicated by dashed lines in Figure 6(a)), and is known as the Stone-Wales transformation.[126] The Stone-Wales transformation effectively elongates the tube in the strain direction, releasing the excess strain energy.[151,155] In a zigzag tube, which experiences longitudinal strain, the "EF" bond in Figure 6(b) forms a 60^{o} angle with the tube axis, and a similar (5-7-7-5) defect (indicated by a dashed line in Figure 6(b)) cannot effectively release the excess strain. This implies that a greater resistance to axial strain should be expected in zigzag nanotubes.

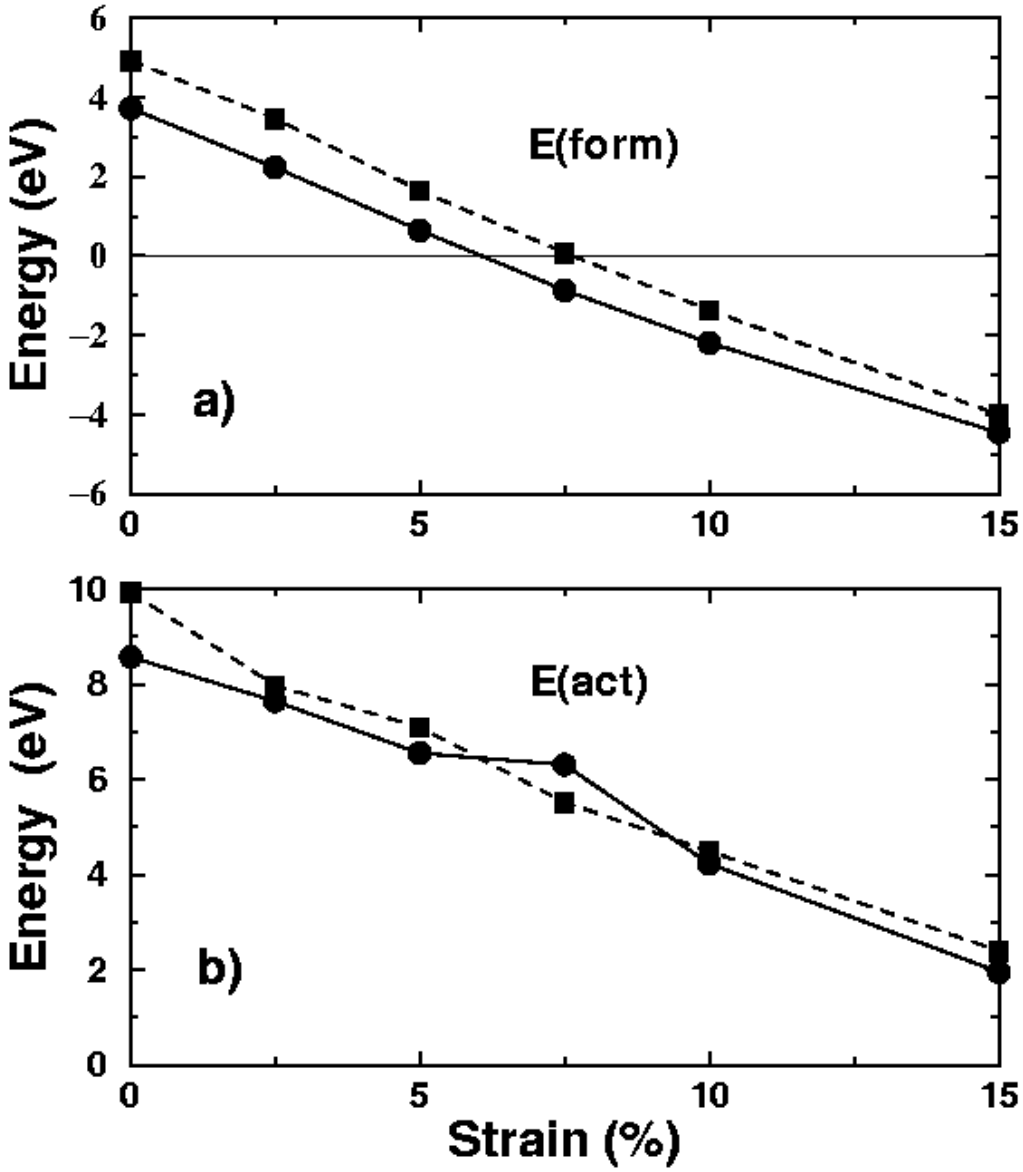

Figure 7 (a) Formation energy of the (5-7-7-5) defect in a (5,5) nanotube (circles) and a graphene sheet (sqares) as function of uniaxial strain. (b) Activation energy for the formation of the (5-7-7-5) defect.

We have carried out extensive *ab initio* calculations, investigating the formation and activation energies of the (5-7-7-5) defect in a (5, 5) carbon nanotube and a graphene

sheet subject to strains of up to 15%. We used constant-strain instead of constant-stress conditions for computational simplicity. However, constant-stress conditions do not produce significant differences at the onset of nonelastic behavior. While the formation energy (the difference in total energies between a defective and an ideal carbon nanotube) is the quantity that determines the stability of a topological defect, the activation energy (the energy barrier that a system has to overcome to form a defect) is the quantity that determines the ultimate limit of the elastic response. If this barrier is sufficiently high, the defect will not be created even if its formation is thermodynamically preferred, and the elastic response will extend into the metastable regime.[151] The activation barriers for the Stone-Wales transformation have been computed by forcing the angle of the C-C bond to rotate about its center while relaxing all the remaining internal degrees of freedom of the tube at each step.

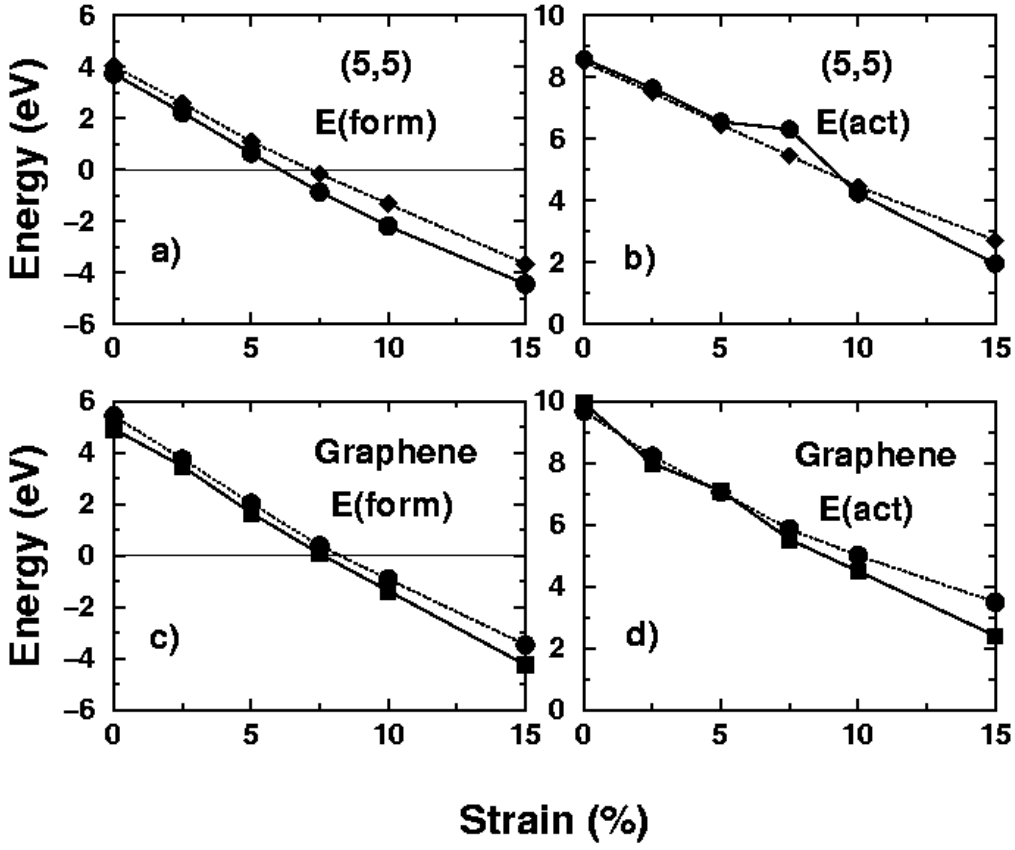

Figure 8 Comparison between *ab initio* and tight-binding results for a (5,5) nanotube and a graphene sheet. (a), (c) Formation energies; (b), (d) activation energies. The *ab initio* results are connected by a solid line, while a dashed line connects the tight-binding results.

The formation energies obtained from calculations are shown in Figure 7(a) for both the (5, 5) tube (solid line) and the graphene sheet (dashed line). The formation energy of the (5-7-7-5) defect decreases almost linearly with strain and the defect becomes energetically favored at strains above 6%. The same trend is observed for the graphene sheet, although the defect energies are about 1eV higher than in the (5, 5) tube. The lower energy of the defects in the nanotube can be attributed to its curvature, which allows for a better relaxation of bond angles. The absence of curvature in the flat graphene sheet makes the formation of the (5-7-7-5) defects less favorable, since the bond angles

between the atoms comprising the defect are forced to deviate from the ideal sp^2 geometry. However, once the (5-7-7-5) defects are formed, their stabilities in the (5, 5) tube and the graphene sheet are comparable. In Figure 7(b) we display the activation energies for defect formation in both the nanotube and the sheet. These energies are very high: at 0% strain they are 8.6 eV in the (5, 5) tube and 9.9 eV in the graphene sheet. The latter value is in good agreement with the "concerted exchange" diffusion process in graphite, where a value of 10.4 eV was obtained.[160] Since the activation energies are so high, the strain relaxation process is kinetically controlled at room temperature. However, the barriers to defect formation decrease significantly with strain. For example, the activation energy for the Stone-Wales transformation in a (5,5) tube becomes 1.95 eV at 15% strain. In general, although the formation energies of the (5-7-7-5) defect in the (5,5) tube are lower than those in graphene with transverse strain, the activation energies in both systems are very close.

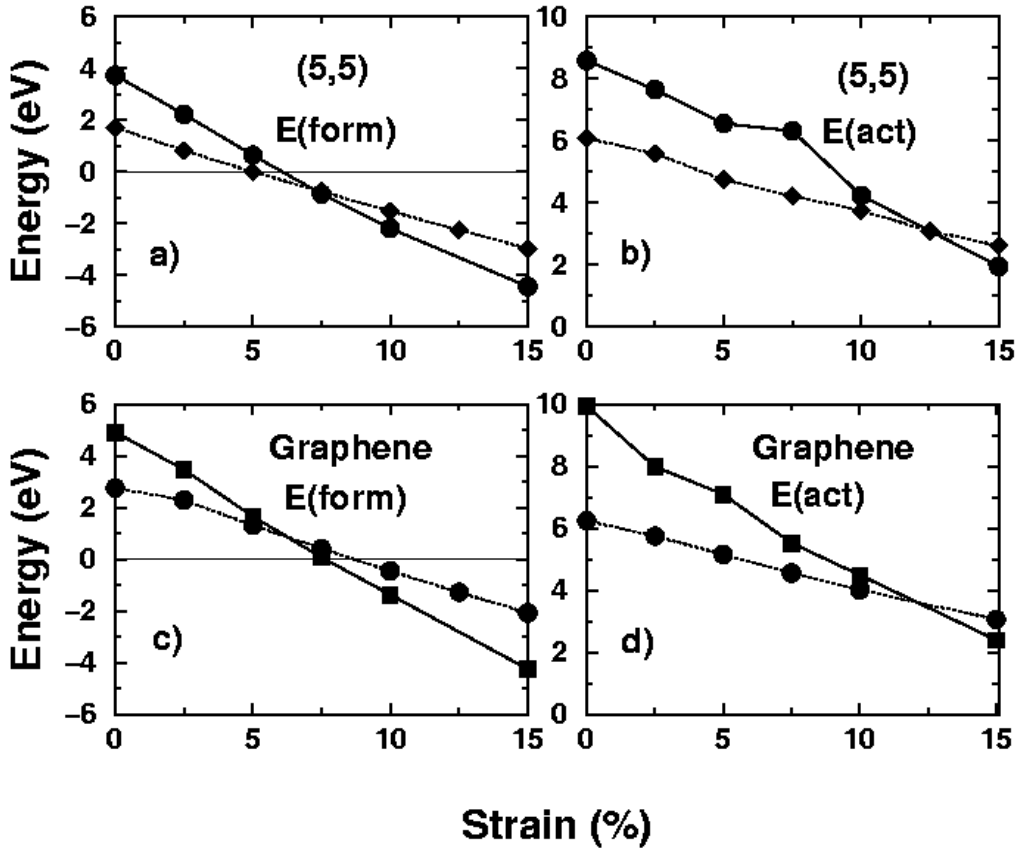

Figure 9 **Comparison between *ab initio* and classical potential results for a (5,5) nanotube and a graphene sheet. (a), (c) Formation energies; (b), (d) activation energies. The *ab initio* results are connected by a solid line, while a dashed line connects the classical potential results.**

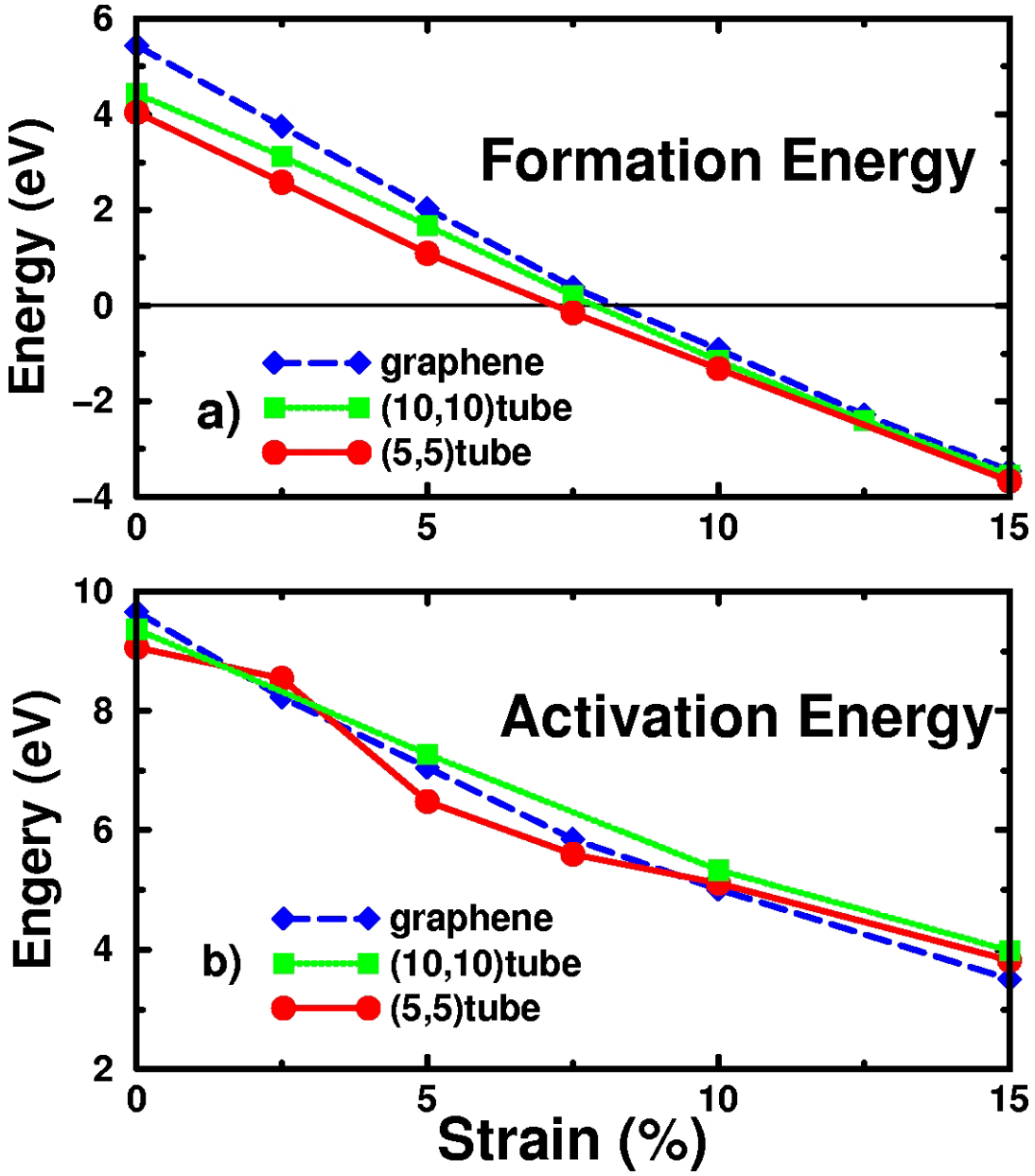

Figure 10 Curvature effects on the formation and activation energies of the (5-7-7-5) defect in strained armchair nanotubes and graphene under transverse strain. Circles correspond to a (5,5) tube, squares to a (10,10) tube, and diamonds to a graphene sheet.

The high activation energies suggest that the perfect hexagonal network is kinetically stable even for strain values substantially larger than 5%. The use of a simple Arrhenius

expression $\Gamma = N_{bonds}\bar{\nu}e^{\frac{-\Delta E}{k_B T}}$ confirms that the tubes are extremely stable at room temperature in their hexagonal equilibrium configuration due to the large value of the activation energy ΔE. The quantities that enter in the Arrhenius expression are the activation energy for the bond rotation ΔE, the absolute temperature T, the Boltzmann constant k_B , the number of bonds N_{bonds} , and an effective frequency $\bar{\nu}$, which is associated with the vibration of the bond in the direction of the saddle point. We estimate the latter using the frequency of the bond rotation mode[161] in a carbon nanotube, 10^{-13} sec^{-1}. The same conclusion can be drawn on the basis of the only two published experiments that have measured the strength of carbon nanotubes. In both cases, some carbon nanotube samples have supported maximum strain values above 5%. These values, although in remarkable agreement with the prediction of the thermodynamic stability of the (5-7-7-5) defect,[151] do not represent the ultimate strain limit for the system. The presence of frozen-in defects that were formed during growth can certainly limit the maximum sustainable strain, since they act as nucleation centers for further topological modifications.[151,153] Moreover, the appearance of a (5-7-7-5) defect can be interpreted as a nucleation of a degenerate dislocation loop in the planar hexagonal network of the graphite sheet.[153,155] The configuration of this primary dipole is a (5-7) core attached to an inverted (7-5) core. The (5-7) defect behaves thus as a single edge dislocation in the graphitic plane. Once nucleated, the (5-7-7-5) dislocation loop can ease further relaxation by separating the two dislocation cores, which glide through successive Stone-Wales bond rotations. This corresponds to a plastic flow of dislocations and gives rise to ductile behavior in the nanotube. Moreover, the 5-7 defect is the smallest defect that can change the tube index without drastically altering the local curvature of the

nanotube.[162,163,164,165] In fact, the dissociation of the (5-7-7-5) defects results in seamlessly connected nanotube sections of different symmetry. The relevance of this process for the production of all-nanotube microelectronic devices has been recently demonstrated experimentally[166] and was also discussed theoretically in conjunction with adatom adsorption.[167]

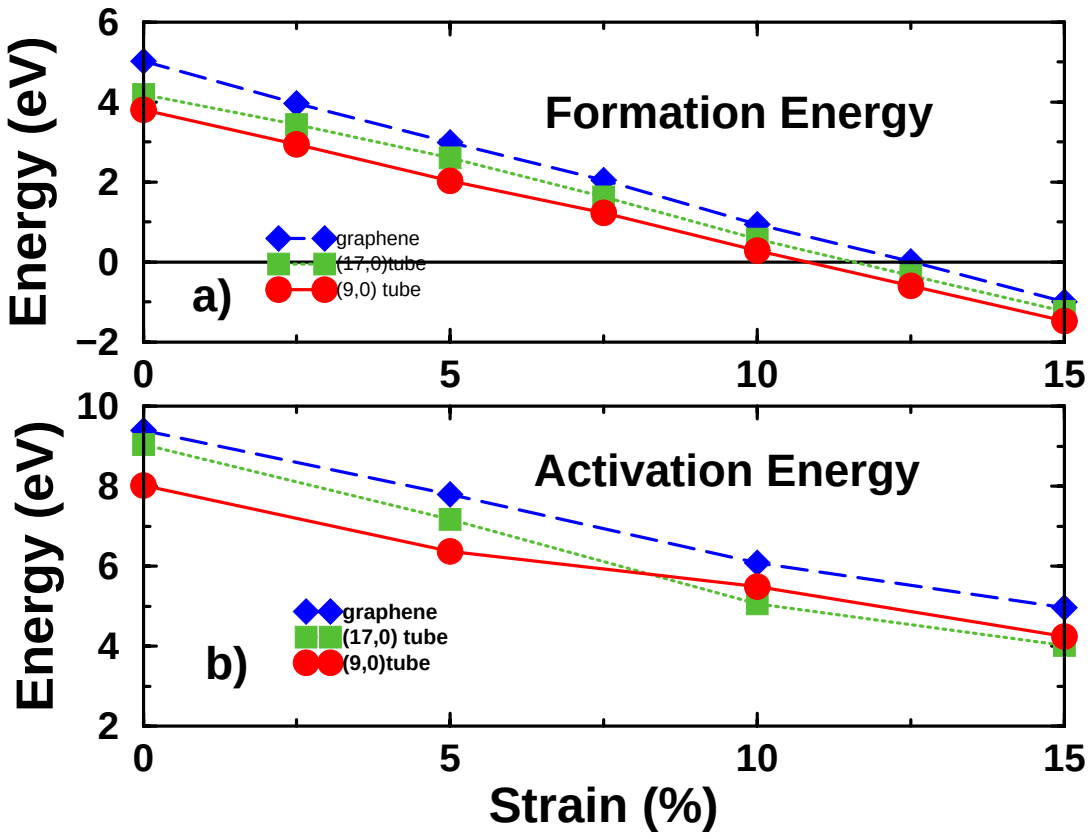

Figure 11 Curvature effect on the formation and activation energies of the (5-7-7-5) defect in strained zigzag nanotubes and graphene under longitudinal strain. Circles correspond to a (9,0) tube, squares to a (17,0) tube, and diamonds to a graphene sheet.

We have extended the present investigation to a larger variety of nanotubular systems using tight-binding and classical potential methods. These more phenomenological techniques are needed to overcome the substantial limitations of *ab initio* calculations

with regard to system size and the number of cases that can be studied.

We first turn to comparisons between *ab initio*, tight-binding and classical molecular dynamics results, in order to determine the reliability of the simpler techniques. Figure 8 compares the results of *ab initio* and tight-binding calculations for both the (5,5) tube and the graphene sheet. As is evident from the figure, the tight-binding results are in very good agreement with the *ab initio* ones, e.g., the formation energies of the (5-7-7-5) defect in graphene obtained from tight-binding calculations are only 0.4 ± 0.1eV higher than those from *ab initio* calculations. However, the differences between tight-binding and *ab initio* results increase with strain. For example, the formation energies of the Stone-Wales defect in the (5,5) tube differ by 0.3 eV at 0% strain and by 0.8 eV at 15% strain. This increase can be attributed to the fact that the tight-binding parameters were fitted to data for unstrained carbon systems. Therefore, their accuracy and reliability decreases with increasing strain. Moreover, the agreement between the tight-binding and *ab initio* results is much better for graphene than for the (5,5) tube. This is because graphite data were used in fitting the original tight-binding parameters, while carbon nanotube data were not. In general, however, the tight-binding method is a good alternative to the computationally costly *ab initio* method. Turning to the classical potential results, while they are able to give a qualitative and semi-quantitative description of the mechanical behavior of nanotubes, they tend to underestimate the ultimate limit of the elastic response. This is shown in Figure 9, where a comparison with *ab initio* results is displayed. Although the classical potentials accurately reproduce the lattice constants, the binding energies and the elastic constants of both graphite and diamond, our comparison shows that the lack of a quantum-mechanical description leads

to significant underestimates in both activation and formation energies.

We have investigated the curvature and helicity effects on the defect formation mechanism using the tight-binding method. Figure 10 and Figure 11 show the formation and activation energies of a (5-7-7-5) defect in armchair and zigzag tubes of different diameters, and compare it to graphene. In armchair tubes, the defect becomes stable at strain values of 7%-8%. (The *ab initio* result for the (5,5) tubes is 6%.) Furthermore, although the (5-7-7-5) defect formation is the dominant mechanism for strain release in armchair nanotubes, this is not true for zigzag tubes. From Figure 11, this defect is thermodynamically unfavorable up to a very high strain value (about 10%). Therefore, zigzag nanotubes are expected to be even more resilient than armchair ones and tolerate very high values of axial tension. They thus extend the limit of ultimate strength to unprecedented values, far beyond that of any other known material. The results in Figure 10 and Figure 11 also show the effect of curvature: the lower defect formation energy in (5,5) tube suggests that (5-7-7-5) defects are more favorable in smaller diameter nanotubes. The curvature effect decreases with strain and seems to vanish at a high strain value.

3.4 Conclusions

In summary, we have investigated the mechanism of strain-induced defect formation in carbon nanotubes through extensive quantum-mechanical and molecular mechanics calculations, focusing on the ultimate strength of these systems. Our results show that the excess elastic energy in a strained nanotube is released via a spontaneous formation of

topological defects whose characteristics depend upon the geometry and the diameter of the nanotube. The activation energies for the defect formation are found to be significantly higher than previously estimated, which increases the theoretical predictions of the elastic response and of the onset of mechanical failure in carbon nanotubes to unprecedented values, well beyond those of other known materials. According to the theoretical estimates, carbon nanotubes are by far the strongest material known.

Chapter 4

Electronic transport in carbon nanotube-metal cluster assemblies

Using large scale O(N) real-space DFT-based *ab initio* method, we carried out a theoretical study of SWNT-aluminum cluster assemblies. Structure optimizations show that a thirteen atoms aluminum cluster and SWNTs can form stable structures. While the aluminum cluster brings little change to the nanotube's atomic structure, it affects the SWNT's electrical properties. However, a dramatic change in the assembly's electrical resistance can be introduced by adsorbing gas molecules onto the metal cluster. For example, for a metallic (5,5) tube with an adsorbed Al_{13} cluster, subsequent NH_3 adsorption can drastically decreases the system's conductance, while for the (8,0) semiconducting tube-Al_{13} assembly's conductance increases significantly after the same gas adsorption. The sensitivity of electrical resistance of SWNT-metal cluster assembly to gas adsorption could make them good molecular sensors and may have impact on nanotube electronics. The proposed carbon nanotube-metal cluster assemblies open a new dimension to functionalize carbon nanotubes.

This chapter is organized in the following order: First we discuss the importance of carbon nanotube's electron transport properties to nanotube applications, with focus on sensor applications. In the second section, theoretical simulation methods, mainly

quantum conductance calculations based on Green's function formalism will be presented in detail. In section three, a general introduction to metal clusters will be given. The structures and properties of aluminum metal clusters, especially the one we chose in this work, Al_{13}, is discussed in detail. After that, quantum simulations results for carbon nanotube-metal cluster assemblies are presented. In that section we will look at the structural and electronic properties of both metallic and semiconducting nanotube formed assemblies. In the last section, NH_3 adsorption on such complicated systems is explored. We investigate the changes in the system's conductivity due to the alteration in atomic and electronic structures of CNT-aluminum cluster assemblies induced by the adsorbed NH_3. At the end, we present brief conclusions based on our theoretical results and comment on future theoretical and experimental work.

4.1 Electronic transport properties of CNT based systems and their applications

As shown in Chapter 2, carbon nanotubes combine a full range of extraordinary physical properties, extremely small size and high aspect ratio, high stiffness and excellent flexibility under different mechanical stimuli, high structural and chemical stabilities, and rich and amazing electrical properties. This makes carbon nanotubes out of the most promising materials for next generation applications based on nano-technology. Many potential applications have been proposed and developed for carbon nanotubes, including superstrong composites, energy storage and energy conversion devices (based on H and Li), field emission displays, mechanical, chemical and

biological probes and sensors, radiation sources, nanoelectronic devices and much more. Among all those applications, carbon nanotubes as sensors and probes have attracted much attention after some astonishing experimental and theoretical investigations in recent years. Hongjie Dai's group[140,168] has shown that at room temperature an individual semiconducting carbon nanotube is a good NO_2 and NH_3 sensor with some excellent properties, such at fast response time, high sensitivity, selectivity, reversibility, room temperature operation and small size. The sensing mechanism comes from the fact that semiconducting SWNT's resistance is very sensitive to adsorbed gas molecules. Quickly after this work, extreme oxygen sensitivity of electronic properties of carbon nanotubes was discovered by Collins *et al.*[141] Extensive theoretical and experimental work has been carried out towards understanding of O_2 adsorption on carbon nanotubes.[142,143,144,145] Other groups have also witnessed significant change in CNT's resistance with adsorption of different material.[169,170] Recently, carbon nanotube based single-molecule biosensors or probes have been proposed[171,172,173] to compete with other nanowire nanosensors[174] for highly sensitive and selective detection of biological and chemical species. With some chemical modifications, carbon nanotubes even have the ability to recognize proteins and DNA.[175,176,177] All of the sudden, carbon nanotubes are recognized as the most promising nanometer-sized probes and sensors in chemistry and biology. Recently, carbon nanotube-based resonant-circuit wireless gas sensors have been realized by different groups.[178,179]

Early carbon nanotube sensor layouts are based on a semiconducting SWNT field-effect transistor,[180] proposed by Tans *et al*. in 1998. They found that when two metal contacts were used to connect an S-SWCNT on SiO2/Si substrate, the metal/S-

SWCNT/metal system demonstrates p-type transistor characteristics with resistance change under various gate voltages of up to several orders of magnitude. Based on this transistor layout, several groups have built SWNT nanosensors,[181] where the solid state gate is replaced by nearby molecules that modulate the tube conductance. The sensing capability comes from the sensitivity of the conductance of the carbon nanotube to chemical environment under such layout, although the reason for the conductance change is still subject to debate.

After these experimental discoveries, it is necessary to systematically examine carbon nanotubes' capability and potential as chemical or biological sensors. First of all, due to the strong sp^2 bonding and near-perfect hexagon network, carbon nanotubes are generally stable, it is hard to form strong chemical bonds with carbon nanotubes for most molecules. However, due to their unique electronic structure, the conductance of carbon nanotube-based system can undergo drastic changes in specific chemical/biological environments. Because of their extremely small sizes, carbon nanotube-based sensors can make ultrasmall sensors (even smaller than other nanowires, like SiNW.[174]). Since all carbon atoms are on surface (for SWCNT), if carbon nanotubes' side-walls interact with some specific molecule, they will have very high reaction area. Compared the more stable sidewall, the open or closed end of carbon nanotube could be more chemically reactive. Because carbon nanotubes are mechanically strong and flexible, the small size and high aspect ratio make them suitable to probe very small caves or other complicated geometries.[172,173] Furthermore, experimental work shows that carbon nanotube-based sensors can provide high sensitivity with high selectivity.[171,140] With appropriate chemical modification, carbon nanotubes can thus make unique sensors for special

purposes. Furthermore, the sensitivity of carbon nanotube conductance to the chemical environment makes the idea of chemical modification for tailoring and controlling nanotube transport properties more attractive.

Since carbon nanotubes are chemically stable in general, they have weak or no interaction with a lot of gases or chemical molecules. Simply using carbon nanotube alone as sensor will limit its sensing range and capability. In experiments, some special bio/chemical molecules have been used as functional units on carbon nanotube walls to extend carbon nanotube's reactivity and selectivity.[171,172,173,175] In this work, we propose another way to functionalize the sidewalls of carbon nanotubes. Instead of using molecules, we choose metal clusters to enhance carbon nanotube system's chemical reactivity. Metal clusters are also nanosized materials, and they have a huge family of members, which can provide a full range of reactivity with different materials. We call the carbon nanotube and metal cluster formed new composite, carbon nanotube-metal cluster assembly in this chapter (or assembly in short). Our idea is to use the metal cluster surface as the reactive sites and to monitor the assembly's conductance change in chemical environment. If the metal cluster can physisorb or chemisorb the tested molecule, and the adsorbed molecules on metal cluster surface also effectively change the electronic properties of a stable carbon nanotube-metal cluster assembly, then the carbon nanotube-metal cluster assembly makes a good chemical sensor. Eventually, specific receptors could be attached to the clusters, leading to high sensor specificity. Although the idea sounds promising, theoretical analysis and simulations, backed with experimental work, must be carried out to prove this concept. While there is a huge amount of literature about metal clusters and also a few studies of interactions between

carbon nanotubes and metal atoms, chains or substrate, there is little experimental and theoretical work related to the interaction of metal cluster and carbon nanotubes. Therefore, it will be very interesting to explore the interactions of two big families in the nanomaterial world: the nanotubes and metal clusters.

The first question we need answer about carbon nanotube-metal cluster assembly is if they interact and form stable structures. If so, in what way the stable structures will change carbon nanotubes' atomic and electronic structures. To answer these general questions using large-scale *ab initio* simulations, we investigate the physical properties of tube-aluminum cluster assembly. We choose the 13 atom aluminum cluster as an example to study the interactions between clusters and carbon nanotubes (metallic or semiconducting). Both the atomic and electronic structures of this new material are studied. After the stable structures of CNT-metal cluster assemblies are identified, we examine the carbon nanotube-metal cluster assemblies' transport properties under NH_3 adsorption. Our simulation results show that for both metallic and semiconducting CNT-metal cluster assemblies the conductance is very sensitive to NH_3 gas adsorption. It can be dramatically increased or depleted upon NH_3 adsorption. Therefore, a new way to functionalize carbon nanotube systems as molecular sensors is proposed.

4.2 Quantum transport

In the last two decades, the electronic and transport properties of all kinds of nano-sized structures have been intensively studied due to their great potential in future nano-

scale electronic devices. This has stimulated the theoretical study of quantum conductance in nano-systems, and a variety of theoretical methods have been proposed to deal with this problem. Most methods are based on the Landauer formula,[182,183] which relates the conduction and transmission of electrons to give an intuitive view of the transport problem. The majority of existing methods is based on phenomenological tight binding models, which may not provide a sufficiently reliable and accurate description of complex structures. Recently, some new methods based on *ab initio* calculations have been proposed to solve the quantum scattering problem for the electronic wave functions through the conductor using a number of related techniques: Lippman-Schwinger and perturbative Green's function methods have been used to study conductance in metallic nanowires and recently in small molecular nanocontacts;[184,185] conduction in nanowires, junctions and nanotube systems has been addressed using local[186] or nonlocal[187,188] pseudopotential methods and through the solutions of the coupled-channel equations in a scattering-theoretic approach.[189,190,191] However, based on plane wave representation, these new techniques are severely restricted in terms of the accessible system size due to the poor scaling of plane wave based *ab initio* methods. Recently, Marco Buongiorno Nardelli has proposed a local orbital based algorithm[192,136,193], and this efficient scheme of conductance calculation has been extended to local orbital based order-N method. Since the *ab initio* method provides a complete and consistent description of the interaction between the leads and the conductor in full atomic detail, this method makes large scale quantum transport calculation reliable and realistic. It works with any system described by a Hamiltonian with a localized orbital basis. The complete microscopic description of the "open" system is allowed. The computational cost is very small since

the quantities entering the conductance calculation are the matrix elements of the Hamiltonian operator.

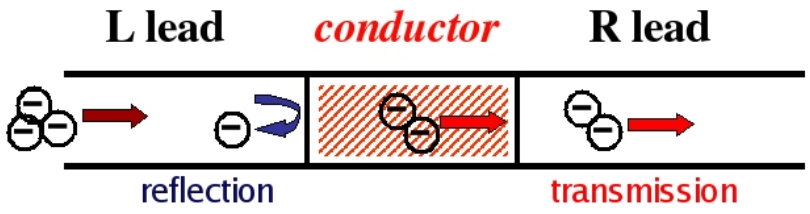

Figure 12 "Open" system in quantum transport

In electronic transport problem, the studied system is considered "open", because that the system is composed of a conductor *C* connected to two semi-infinite leads, *R* and *L*, as in Figure 12. The Landauer formula discloses the fundamental physics by linking the conductance through a region of interacting electrons (the C region) to the scattering properties of the region itself as the following[182]:

$$C=\frac{2e^2}{h}T,$$

where *T* is the transmission function and *C* is the conductance. The transmission function is the probability with which an electron entering at one end of the conductor will transmit to the other end. The transmission function can be obtained with the knowledge of the Green's functions of the conductors and the coupling of the conductor to the leads by the following formula:

$$T=\mathrm{Tr}(\Gamma_L G_C^r \Gamma_R G_C^a),$$

where $G_C^{\{r,a\}}$ are the retarded and advanced Green's functions of the conductor, and $\Gamma_{\{L,R\}}$ are functions that describe the coupling of the conductor to the leads. The Green's function of the conductor can be derived from the equation for the Green's function of

the whole system:

$$(\varepsilon S - H)G = I,$$

where ε=E+iη with η arbitrarily small, I is the identity matrix and S is the overlap matrix. In matrix representation, the solution will be the inversion of an infinite matrix for the open system, consisting of the conductor and the semi-infinite leads. To invert the infinite matrix, it has to be partitioned and truncated. The Green's function of the whole "open" system can be naturally partitioned into submatrices that correspond to the individual subsystems,

$$\begin{pmatrix} G_L & G_{LC} & G_{LCR} \\ G_{CL} & G_C & G_{CR} \\ G_{LRC} & G_{RC} & G_R \end{pmatrix} = \begin{pmatrix} (\varepsilon S_L - H_L) & h_{LC} & 0 \\ h_{LC}^{\dagger} & (\varepsilon S_C - H_C) & h_{CR} \\ 0 & h_{CR}^{\dagger} & (\varepsilon S_R - H_R) \end{pmatrix}^{-1}$$

where the matrix ($\varepsilon S_C - H_C$) represents the finite isolated conductor, ($\varepsilon S_{\{R,L\}} - H_{\{R,L\}}$) represent the infinite leads, and h_{CR} and h_{LC} are the coupling matrices that will be nonzero only for adjacent points in the conductor and leads, respectively. From this equation it is straightforward to obtain an explicit expression for G_C:

$$G_C = (\varepsilon S_C - H_C - \sum_L - \sum_R)^{-1}$$

where we define $\sum_L = h_{LC}^{\dagger} g_L h_{LC}$ and $\sum_R = h_{RC} g_R h_{RC}^{\dagger}$ as the self-energy terms due to the semi-infinite leads and $g_{\{L,R\}} = (\varepsilon S_{\{L,R\}} - H_{\{L,R\}})^{-1}$ are the leads's Green's functions. The self-energy terms can be viewed as effective Hamiltonians that arise from the coupling of the conductor with the leads. Once the Green's functions are known, the coupling functions $\Gamma_{\{L,R\}}$ can be easily obtained as

$$\Gamma_{\{L,R\}} = \left[\sum\nolimits^{r}_{\{L,R\}} - \sum\nolimits^{a}_{\{L,R\}}\right],$$

where the advanced self-energy $\sum^{a}_{\{L,R\}}$ is the Hermitian conjugate of the retarded self-energy $\sum^{r}_{\{L,R\}}$. With the help of principal layers in the framework of the surface Green's function-matching theory, we get the self-energies:

$$\Sigma_L = (\varepsilon S_{LC} - H_{LC})^{+}[\varepsilon S^{L}_{00} - H^{L}_{00} + (\varepsilon S^{L}_{01} - H^{L}_{01})^{+}\bar{T}_L]^{-1}(\varepsilon S_{LC} - H_{LC})^{+},$$

$$\Sigma_R = (\varepsilon S_{CR} - H_{CR})^{+}[\varepsilon S^{R}_{00} - H^{R}_{00} + (\varepsilon S^{R}_{01} - H^{R}_{01})^{+}T_R]^{-1}(\varepsilon S_{CR} - H_{CR})^{+},$$

where $H_{nm}^{L,R}$ are the matrix elements of the Hamiltonian between layer orbitals of the left and right leads, respectively. $S_{nm}^{L,R}$ are the corresponding overlap matrices and $T_{L,R}$ and $\bar{T}_{L,R}$ are the appropriate transfer matrices. The latter are easily computed from the Hamiltonian and overlap matrix elements via an iterative procedure. Correspondingly, H_{LC}, H_{CR}, S_{LC} and S_{CR} are the coupling and overlap matrices for the conductor-lead assembly.

The matrix elements of Hamiltonian and overlap matrices come from the real-space local orbital based order-N *ab initio* method which we introduced in chapter 1. Since the system size of SWNT-metal cluster has to be very large (~200 atoms with very large vacuum), only very efficient methods can make computational load manageable.

We use the local density exchange-correlation functional and the Perdew-Zunger parametrization of the Ceperley-Alder exchange-correlation energy. The Kleiman-Bylander approach was chosen to include nonlocal, norm-conserving pseudopotentials. In our *ab initio* simulations, the typical simulation supercell dimension is 17.3x14.8x24.7 Å for an assembly with a 140 carbon atom (5,5) tube and a thirteen aluminum atom metal cluster with one absorbed NH_3 molecule. The supercell contains a large vacuum region

(>8Å) to ensure that image interactions can be neglected. Small grid spacing about 0.15Å is used throughout, corresponding to a high energy cutoff of about 58 Rydbergs.

4.3 Metal clusters and Al_{13}

Metal clusters are small particles consisting of a limited number of atoms, ranging from the diatomic molecule to a vaguely defined upper bound of several hundred thousand atoms. Although metal clusters are not totally a new type of material since, for example, the glaziers of the Middle Ages discovered how to produce beautiful stained glasses by special treatments of metal containing glasses, people knew little about metal clusters till 1960s. The early investigations[194,195] of metal clusters were focused mainly on materials related to metal particle contaminants in glass. Things start to change in the 1960s and 1970s after new cluster sources were introduced to for making clusters composed of only a few atoms in the gas phase.[196] The early results indicated that these extremely small particles had properties that could be totally different from the bulk. They were thought of as small molecules, and we know that each molecule is unique. This is reasonable, since for these very small particles the surface is important and their structures may be complicated and quite different from each other. From solid state physicists' points of view, even for a cluster with up to 1000 atoms, there are a quarter of the atoms on the surface, which make the surface play a much more important role in determining the material's properties than what it does in the bulk. However, the pioneering work in the early 1980s found new phenomena in the cluster world and

eventually gives the birth to a new research field: cluster physics.

In late 1983, Walter Knight's group, with Keith Clemenger, Walt de Heer, and Winston Saunders has successfully produced and detected clusters of alkali metals with up to about 100 atoms. After analyzing the cluster abundance spectra they immediately found that there are some magic numbers in which the metal clusters were produced more abundantly. The explanation of these magic numbers reflects the fundamental rule that the electronic structure of these clusters appears to be determined by a spherical potential well.[197] This leads to the shell model[198] which considers the electrons to be nearly free and confined in a potential well. The shell model yields a series of magic numbers, like 2, 8, 20, 40, 58..., in which the electrons just finished filling degenerate energy levels. Theoretically, the ionic cores are considered to provide a uniformly charged positive background, and the electronic structure is subsequently calculated using various approximations for the interacting electron gas, such as in the self-consistent jellium calculations.[199] Almost at the same time, Ekardt[200] independently found the shell structure in his model for alkali clusters using the jellium approach. Since its discovery, the electronic shell structure is found in many simple and noble-metal cluster systems. Furthermore, people found that these characteristic abundance patterns appear even in clusters with up to thousands of atoms.[201] This is the so called supershell. In numerous experiments, the electronic shell structure was verified in the electronic response properties (ionization potentials, polarizabilities, collective excitations, etc.), and the jellium model was further developed to models with a high degree of sophistication, like the Clemenger-Nilsson model,[202] which takes into account the effect of the deformation of spherical potential for open-shell clusters. For open-shell clusters, the spherical shape

is unstable towards distortions due to the Jahn-Teller effect,[203] which has important and readily observable consequences.

The shell model achieves surprising success in describing the metal clusters. The most important is that it provides essential insight into the fundamental physics involved and the electronic shell structure becomes the unifying principle linking cluster systems as diverse as lithium and gold. The experimental evidence for electronic shell structure is overwhelming, and the shell model looks like to be able to withstand more and more experimental and theoretical tests. In fact, people are becoming more interested in finding the deviations and failures from the simple shell model. In general, shell model works well in simple and noble-metal clusters where valence electrons are more or less free-electron-like, and it fails where the interactions between valance electrons are more directional and complicated, as in transition metal clusters. The atomic structure is of cause influenced by the electronic shell structure, and the clusters with closed shells are the most stable.

There is a lot of literature about metal clusters in the past few decades. For complete coverage of all aspects of metal clusters, the proceedings[204] of the ISSPIC conferences (International Symposium on Small Particles and Inorganic Clusters) are very helpful resources. For quick reviews, Walt A. de Heer[205] and Matthias Brack[206] have excellent review articles, covering experimental and theoretical issues.

To study the interactions between metal clusters and carbon nanotubes, we start with aluminum clusters. This is because that aluminum sits between simple alkalis and complex noble-metals in terms of physical properties. Aluminum clusters[207,208,209,210,211,212,213,214,215,216,217,218,219,220,221,222,223,224,225,226,227,228,229,230] are also the

most studied systems among simple metals except alkalis. Like the alkali metals, aluminum has their valence electrons nearly free. However, unlike the alkalis, aluminum is trivalent[231] and Al atom has 3s and 3p orbit with energy separation at about 3.6 eV.[232] For the shell model to hold, one of the 3s electrons has to be promoted to a 3p orbital. Furthermore, the +3 ionic cores of Al clusters could cause large perturbations to the spherical jellium potential. Photoelectron spectroscopy study clearly shows the process of s-p hybridization and the deviations from shell models.[229] Small aluminum clusters ($n<11$) differ significantly from what jellium model describes due to the large 3s-3p energy separation. But shell closing signatures are shown at Al_{11}^-, Al_{13}^-, up to Al_{56} and Al_{73}^-. The electron shell effect diminishes above Al_{73}^-, and new spectral features appearing in large clusters ($n>100$) suggest a possible geometrical packing effect. Among so many aluminum clusters, we select Al_{13} to interact with SWNT. This is because Al_{13} needs only one electron to close the electron shell at 40 and it also assumes a highly symmetric geometry. In experiment, Al_{13}^- with 40 valence electrons exhibits the strongest shell closing effect and it is very stable (it does not react with oxygen). Al_{13} and its derived binary clusters $Al_{13}X$ or $Al_{12}X$ (X=Cu, Ag, Au, C, *et al*.)[233,234,235,236,237] show enhanced stability and are thought as the possible building blocks for future metal cluster crystals. Several theoretical investigations show that Al_{13} have several isomers with different geometries, and some of them could be nearly degenerate. Most of theoretical simulations[234,238,239,240] tend to suggest that the slightly Jahn-Teller distorted icosahedral structure is the ground state, which appears to be close to what the experimental data indicates. In our real-space LDA ab init simulations, the Al_{13} cluster starts from perfect icosahedral structure, and ends with slight Jahn-Teller distortion after full geometry

relaxation.

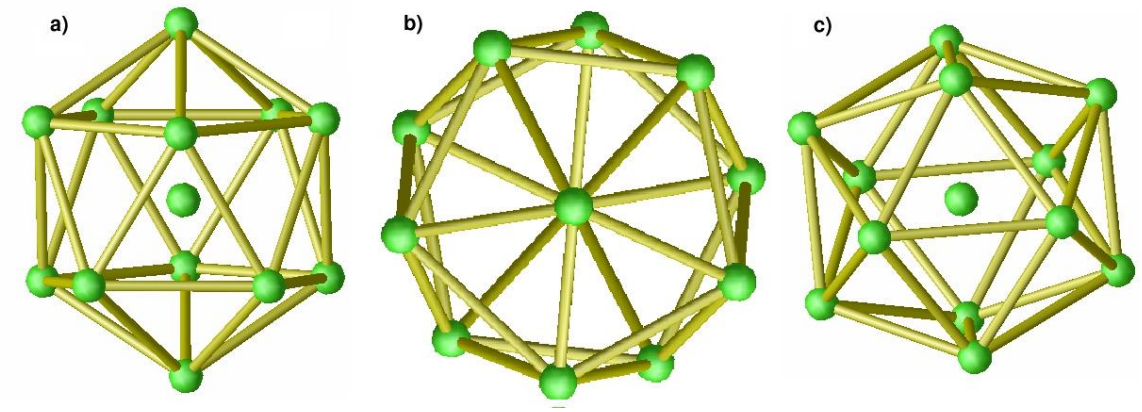

Figure 13 Icosahedrical structure of the Al_{13} cluster viewed from different angles.

The relaxed atomic structure of Al_{13} is shown in Figure 13. The three subfigures are views from different angles. If the structures were not Jahn-Teller distorted, the two-dimensional projection of the icosahedron (showed in subfigure b) would have all the ten peripheral atoms placed exactly equidistant from each other as in the first projection. It appears that the Jahn-Teller distortion is very small. The binding energy is 3.1eV/atom, which agrees well with results from other groups. The average bond length for the bonds from surface atoms to the center atom is 2.62 Å (2.60 Å to 2.66 Å). The HOMO-LOMO gap in Al_{13} icosahedron is 1.3 eV. The 3D charge density plots of the nine lowest occupied electronic states are shown in Figure 14. It shows high symmetry in all electronic states, and in these states electrons are nearly uniformly distributed within a sphere, with more oscillations for higher energy states. Our first principle results imply that the jellium model is capable to describe aluminum clusters sufficiently well. It is easy to recognize the 1s, 1p and 1d states from Figure 14. It is interesting to see how tube-cluster interaction breaks the symmetry of these electronic states and to what degree

and which states hybridize with carbon nanotube states.

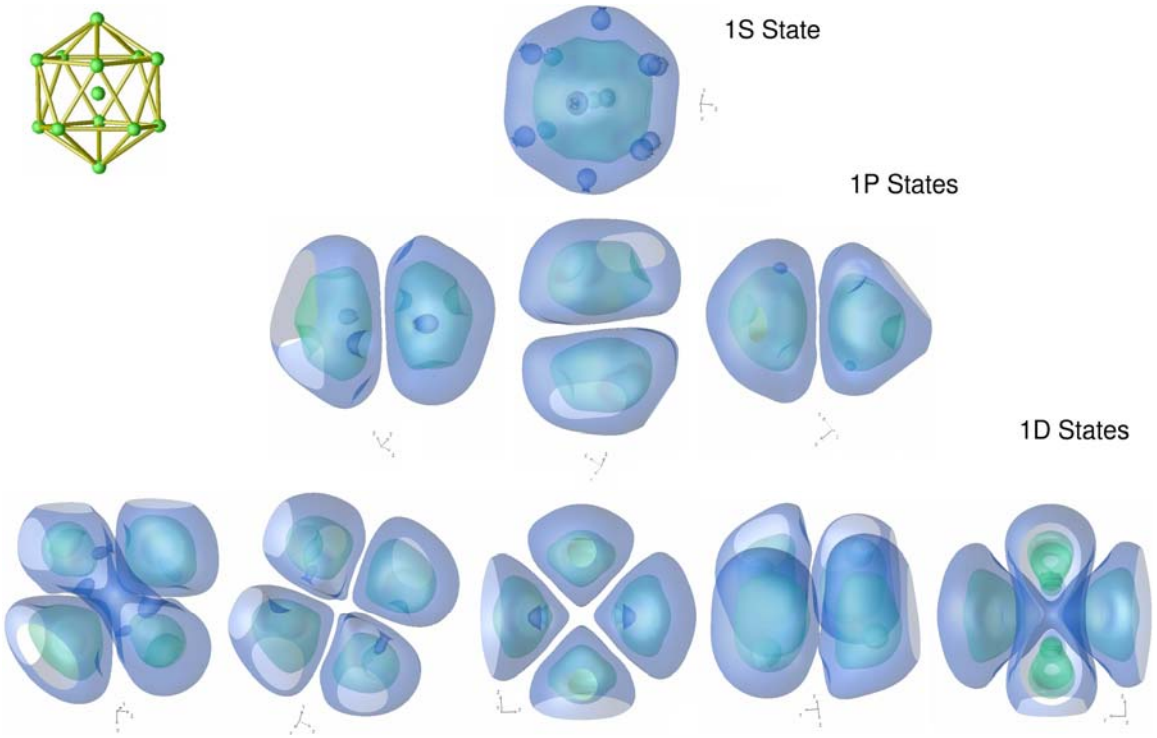

Figure 14 Some Al_{13} electron states from *ab initio* calculations. The plots are isosufaces of charge density. The inner green isosurface has charge density 10 times higher than the blue one.

4.4 Carbon nanotube and aluminum cluster assemblies

Although there is no published work on carbon nanotube-metal cluster assembly to the best of our knowledge, researchers started to investigate the interaction between nanotubes and metals in recent years. Using first-principles total-energy pseudopotential calculations, Rubio *et al.*[241] have investigated the electronic structure of one-dimensional

chains of metal atoms (Al and Pt) in carbon and BN nanotubes. For metal atom chains in small diameter nanotubes, there are two types of interactions: charge-transfer (dominant for alkali atoms) leading to strong ionic cohesion, and hybridization (for mulivalent metal atoms) resulting in a smaller cohesion. They found that both charge-transfer and hybridization can contribute to tube-Al chain interaction. In a more recent paper, O. Gülseren *et al.*[242] have studied single aluminum atom adsorption on the outside wall of SWCNT with *ab initio* calculations. They found that the aluminum atom is adsorbed on the center of a hexagon and that the adsorption is exothermic. The associated binding energy varies inversely with the radius of the zigzag tube. However, there are no experimental reports for Al-graphite intercalation compounds (GICs) and Al intercalation into carbon nanotubes.

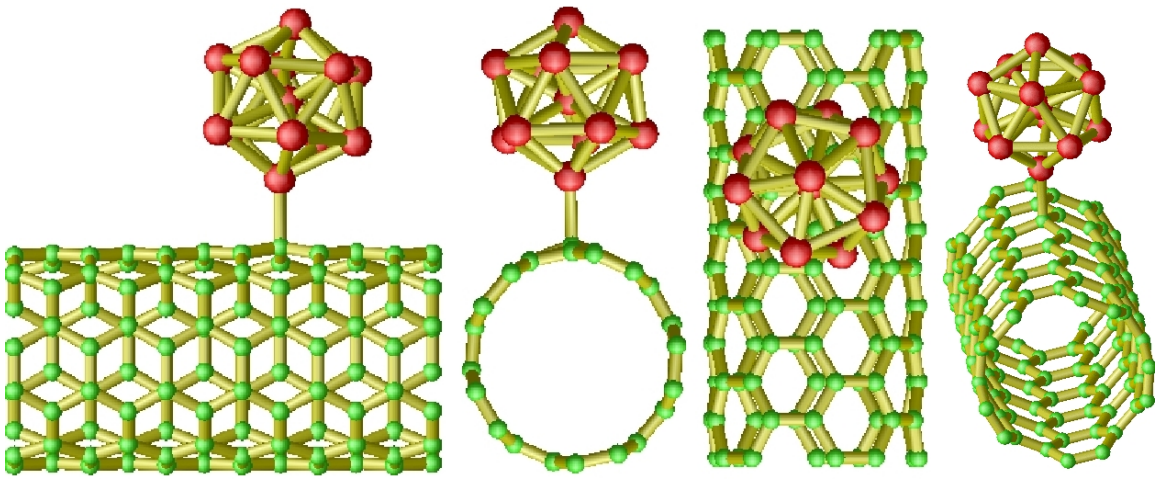

Figure 15 "On-top" structure of (5,5) SWNT- Al13 assembly viewed from different angles.

Since there was no information about the interaction between carbon nanotubes and metal clusters, we must carry out careful geometry optimizations for the studied systems. We apply first principles calculations throughout to make sure that the description of

tube-cluster interaction and of the corresponding charge transfer is reliable and accurate. We choose two SWNTs with similar diameter: one metallic (5,5) tube and one semiconducting (9,0) tube to interact with the Al_{13} cluster. To find the stable geometries of the nanotube-metal cluster assemblies, careful geometry optimization and energetic analysis have been performed. The metal cluster, Al_{13}, has been placed at different sites on the nanotube surface and at different distances. For example, the Al_{13} is placed on the center of the hexagon, the C-C bond center, the top of C atom, or with a configuration where one Al-Al bond parallel to one C-C bond. After relaxations, all initial configurations go to one final structure, where the Al_{13} stays right on top of one carbon atom with one aluminum atom binding/pointing to this carbon atom. We call this stable structure "on-top". During the relaxation to the "on-top" structure, both the (5,5) tube and Al_{13} cluster keep their basic geometry, while the bonding atoms are pulled slightly closer to each other. The formation energy (binding energy) is defined as: $E_f = E_{tot}(\text{ (5,5)tube }) + E_{tot}(\text{ } Al_{13}) - E_{tot}(\text{ (5,5)tube}+Al_{13}\text{ })$. The value of E_f is 0.46eV, which means that the "on-top" geometry is stable. The equilibrium C-Al bond length is 2.22 Å. Figure 15 shows the stable “on-top” structures of (5,5) tube-Al_{13} assembly from different directions.

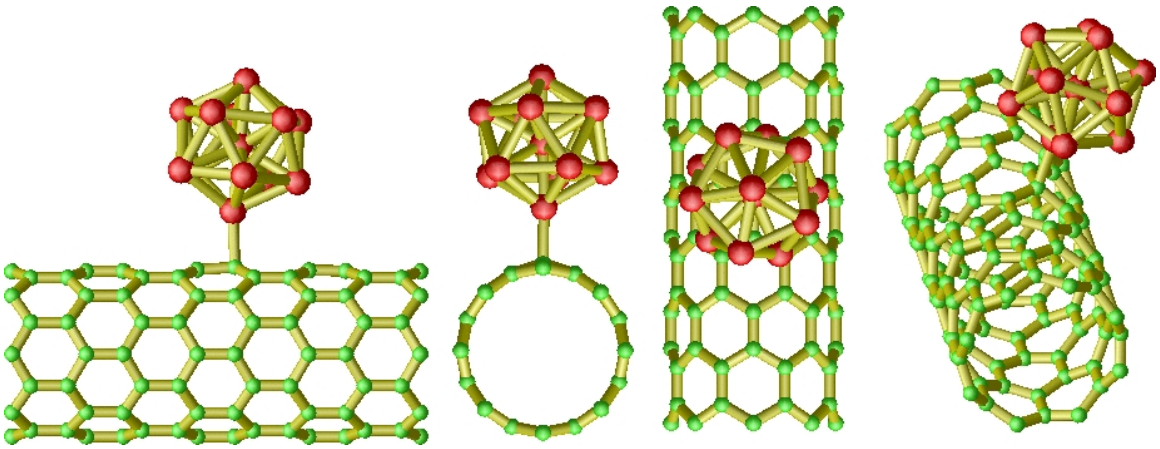

Figure 16 Stable structure of (8,0) tube- Al13 assembly viewed at different angles.

The (8,0) zigzag SWNT forms similar structure with Al_{13} assembly, but the interaction between Al_{13} and the zigzag tube is substantially stronger. This results in shorter C-Al bond (2.15Å) and higher binding energy (0.7eV). The atomic structure of (8,0)tube-Al13 assembly is shown in Figure 16.

4.5 Quantum transport of CNT-metal cluster assembly upon NH_3 absorption

As discussed in the last section of chapter 2 and the first section of this chapter, the conductance of carbon nanotubes is sensitive to molecular adsorption, which forms the sensing mechanism of nanotube-based chemical sensors. We are curious to see how

metal clusters can enhance and expand the sensitivities of nanotube sensors. Metal clusters including aluminum, have rich chemistry.[243,244,245,246,247,248] We expect that the chemical reaction (molecule adsorption) on metal clusters can affect nanotube-metal cluster assemblies' conductivity. Since we are interested in how the gas adsorption on metal cluster affects the electronic transport properties of carbon nanotube-metal cluster assembly, quantum transport calculations are performed with the method discussed in section 2. NH_3 is chosen as the studied adsorption gas simply because that it is one of the most important gases for research and industry interest. Bulky and slow NH_3 sensors[249,250,251,252,253,254] are widely used in environmental and industrial process monitoring. Aside from the early SWCNT ammonia sensing experiment,[140] wireless ammonia sensors[178,179] based on carbon nanotubes were developed recently.

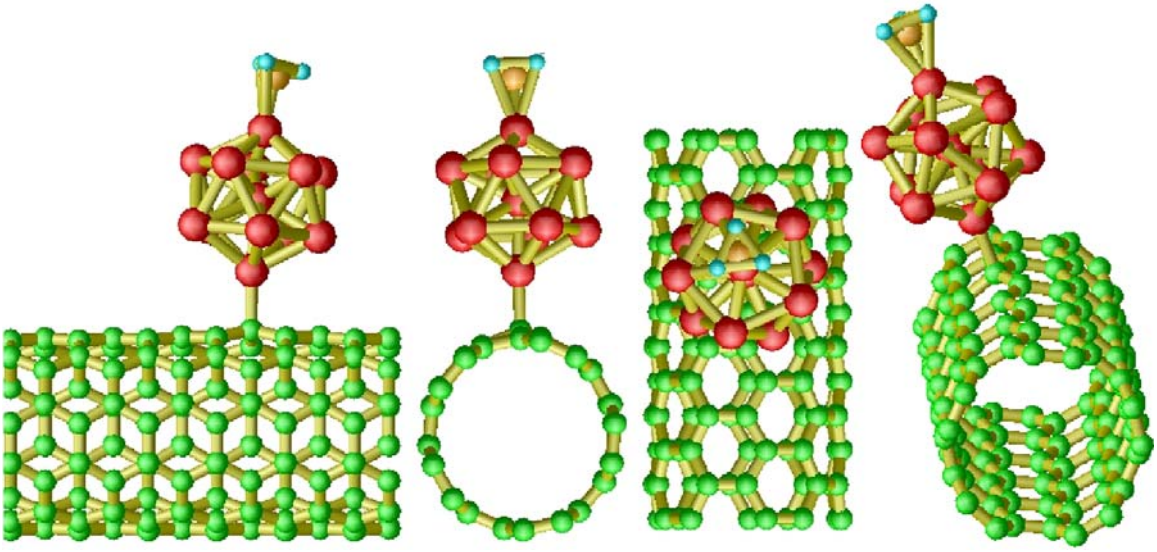

Figure 17 Atomic structure of (5,5)- Al_{13} with NH_3 adsorption

For the structure optimization of NH_3 absorption on Al_{13}, we start with configurations where the ammonia molecule is located far from carbon nanotube and the nitrogen atom

interacts with Al_{13} directly. After relaxation, the NH_3 stays on the top of one vertex of Al_{13}, and the adsorbed ammonia does enhance the bonding between the tube and metal cluster without altering their atomic structure significantly. Figure 17 shows the structure of (5,5)-Al_{13} after NH_3 adsorption. After adsorbing one NH_3 molecule, the aluminum cluster binds more tightly to the tube, and the formation energy increases from 0.46 eV to 1.6 eV and C-Al bond length is shortened from 2.22 Å to 2.13 Å.

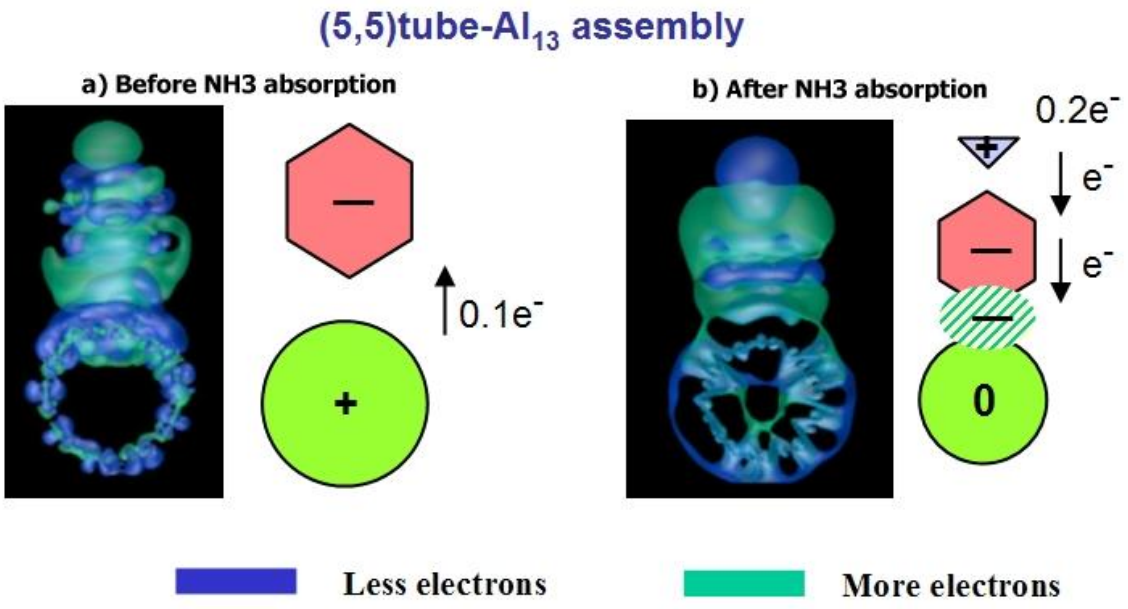

Figure 18 Charge transfer in (5,5) tube-Al_{13} assembly before and after NH_3 adsorption. Sub-figure a) is for (5,5)-Al13 and b) is for (5,5)-Al13 with NH3. In both a) and b), the left figure shows the redistributed electrons due to tube-metal cluster interaction, while the right one is a simplified view of charge transfer. The blue iso-surface indicates less electrons due to interactions, the green iso-surface more electrons.

The charge transfer between the tube and the metal cluster can provide important information for understanding the system's electric properties. The importance of chemical doping is well known for semiconductors. To obtain an accurate value of the

transferred electron charge, normally a surface has to be defined to separate the electron cloud into different parts, which belong to either the nanotube or the metal cluster. Since there is significant overlapping charge between the nanotube and Al13, the value of the charge transfer is very sensitive to the separating surface. We avoid this problem by looking at the difference in charge density between systems with and without tube-cluster interaction. We use the total charge density of the whole system and subtract the charge densities obtained form parts alone, like the charge density from the nanotube with the same geometry. The charge density difference gives the needed information for charge redistribution because of the tube-cluster interaction, and the deduced value of charge transfer is much less dependent on the definition of the separation surface. Figure 18 shows the electron redistribution of the (5,5) tube-Al_{13} assembly before and after NH_3 adsorption. Without NH_3, the charge goes from tube to the Al_{13} cluster with the amount of about 0.1 electrons (Figure 18 a). As a well-known electron donor, NH_3 does donate about 0.2 electrons to Al_{13}. Moreover, the (5,5) tube draws back its charge from Al_{13} and becomes electrically neutral. The adsorbed NH_3 also causes a substantial polarization of charge, shifting it from the "inside" of the nanotube wall to the "outside". Comparing the total charge density and the charge densities of parts, we also notice that there are about 1-2 electrons from Al_{13} overlapping with carbon nanotubes in all studied cases. The overlapping charge will cause orbital hybridization between tube and metal cluster states. Figure 19 shows the states with and without orbital hybridization in (5,5)-Al_{13} assembly after NH_3 adsorption. For the 20 Al_{13} states (39 electrons in Al_{13}), about half of the aluminum cluster states are significantly hybridized. We find that the NH_3 adsorption enhances orbital hybridization between the nanotube and the aluminum cluster, which is

a direct result of stronger interaction between the tube and the cluster after absorbing an ammonia molecule.

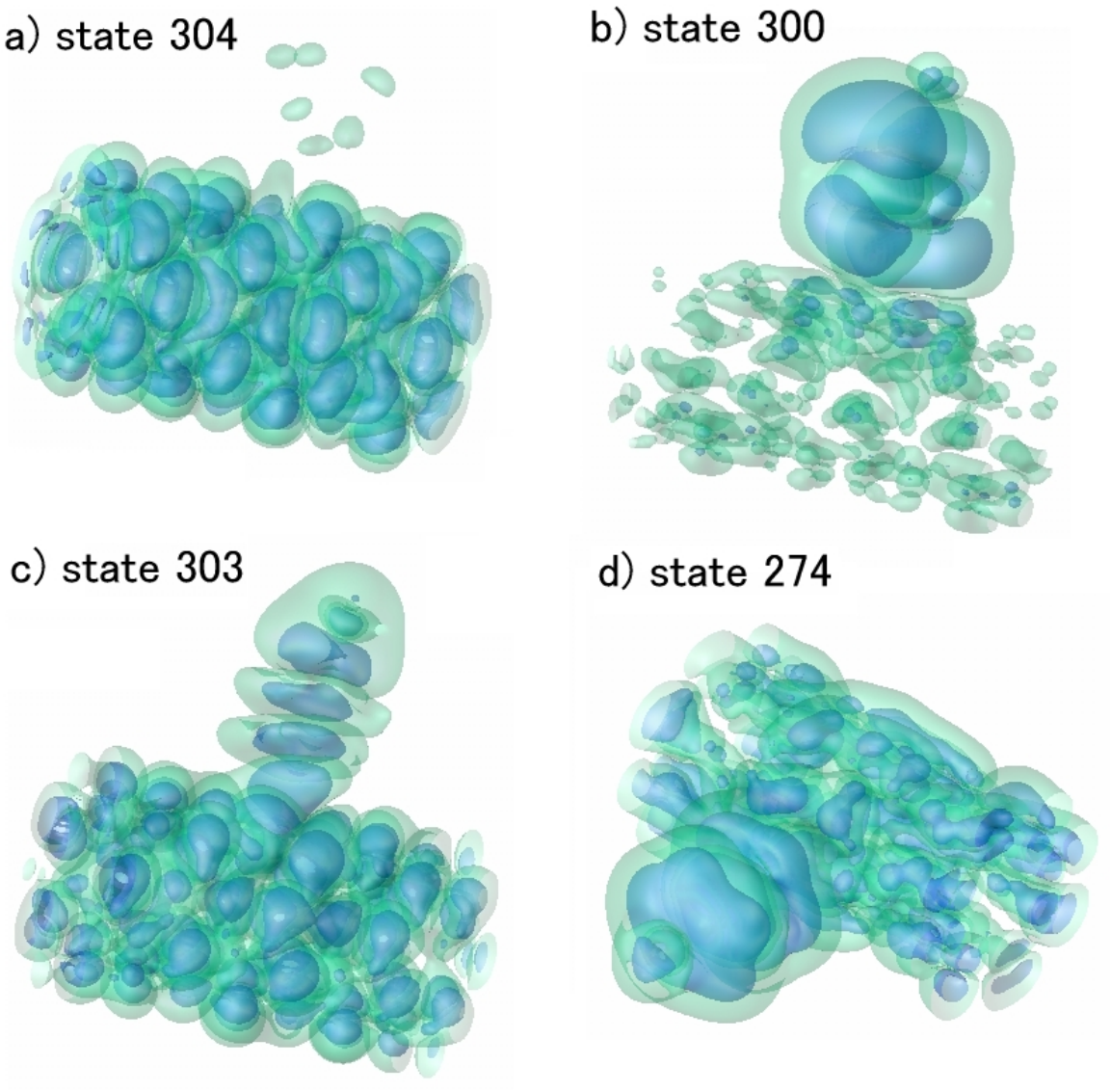

Figure 19 Iso-surfaces of charge density from selected electronic states showing orbital hybridization in (5,5) tube-Al_{13} with NH_3. The blue iso-surfaces have charge density 10 times greater than the green ones. Sub-figures a) and b) are states from (5,5) tube and Al_{13} without orbital hybridization. Subfigures c) and d) show highly hybridized states.

Turning to the electron transport properties, we start from a perfect (5,5) armchair tube. It is well known that armchair carbon nanotubes are excellent conductors, except

for tubes with very small diameter. Theoretical analysis predicts that an armchair nanotube has a quantized conductance of 2 (in units of $2e^2/h$) due to the two bands crossing at Fermi energy. This is confirmed by different experiments. Using the transport calculation method introduced in section 2, we calculated the conductance and density of states (DOS) of a perfect (5,5) armchair nanotube from local-orbital-based *ab initio* simulations. The results, shown in Figure 20, agree well with published data.

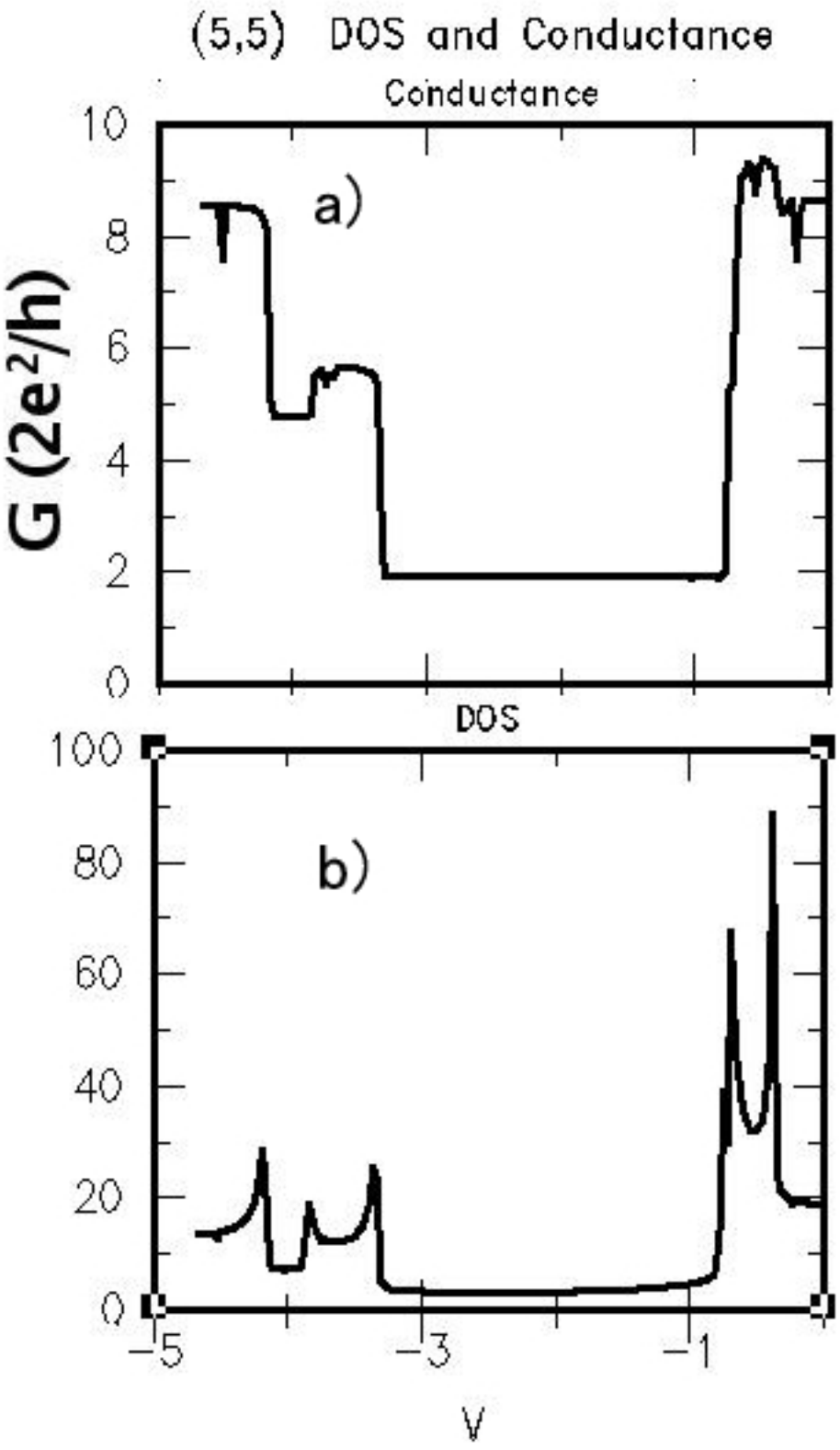

Figure 20 Conductance and DOS of (5,5) carbon nanotube from *ab initio* transport calculations

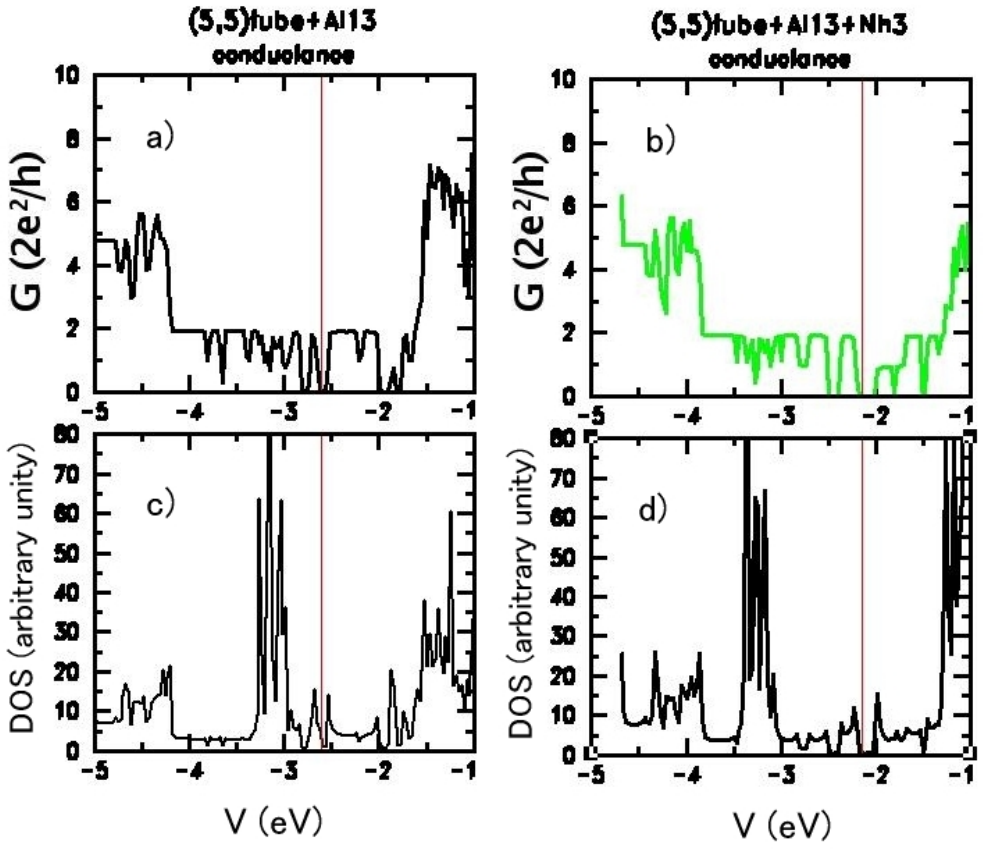

Figure 21 Conductance spectrum and DOS of (5,5) tube-Al13 cluster before and after NH3 adsorption. The red vertical lines are where the Fermi energies are located.

Figure 21 shows the calculated conductance spectrum and DOS for (5,5) tube and Al_{13} and (5,5) tube with Al_{13} and NH_3. The vertical lines show the location of Fermi energies. Although the conductance of (5,5)-Al_{13} (subfigure a) is not perfect 2 (in units of $2e^2/h$) anymore, the conductance is very close to 2 at most of the energy region. The conductance is reduced significantly in some parts of the region, especially near the Fermi level. In the (5,5)-Al_{13} assembly, there is also a very small gap created by the SWCNT-metal cluster interaction. The gap is clearly widened after NH_3 adsorption,

indicating that the interaction between the tube and the cluster gets stronger. The induced gap after ammonia adsorption leads to a conductor-semiconductor transition in (5,5)-Al_{13} assembly. The I-V curves of (5,5) based systems are shown in Figure 22. We see reduced conductivity in (5,5)-Al13 assembly compared to a pure (5,5) tube. After adsorbing one or more ammonia molecules on the aluminum cluster, the assembly's conductance is dramatically diminished and even zeroed at small bias. Due to the significant change in the conductivity of armchair-Al13 assembly after ammonia adsorption, it is very promising to make metallic carbon nanotube-based gas sensors.

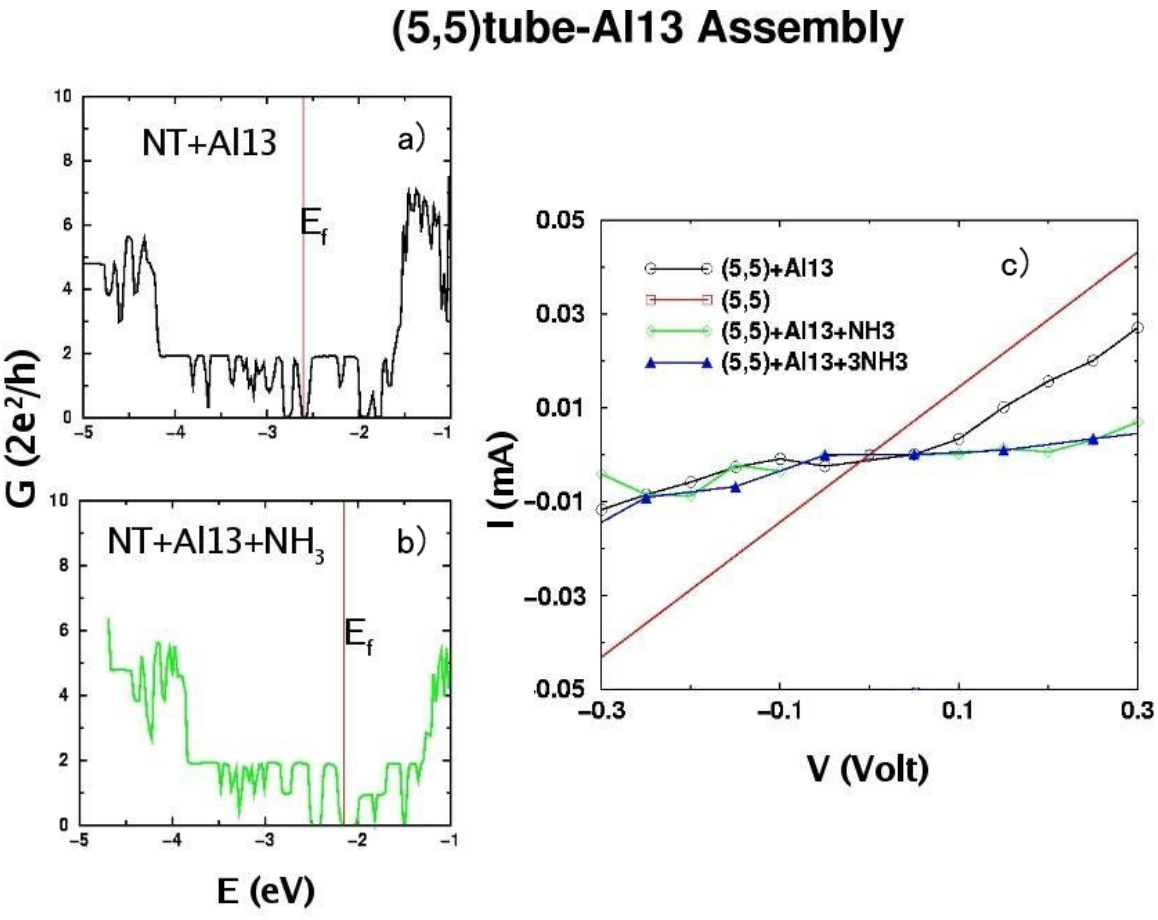

Figure 22 Transport properties of (5,5)- Al_{13} upon NH_3 adsorption

To study the effect of gas coverage, we also increased the adsorbed ammonia molecules to 2 and 3. The results do not show significant change from the case of absorbing one NH_3. Figure 23 shows the total change density of (5,5)tube-Al_{13} with 3 NH_3 adsorbed on. The iso-surfaces also illustrate the atomic structure well.

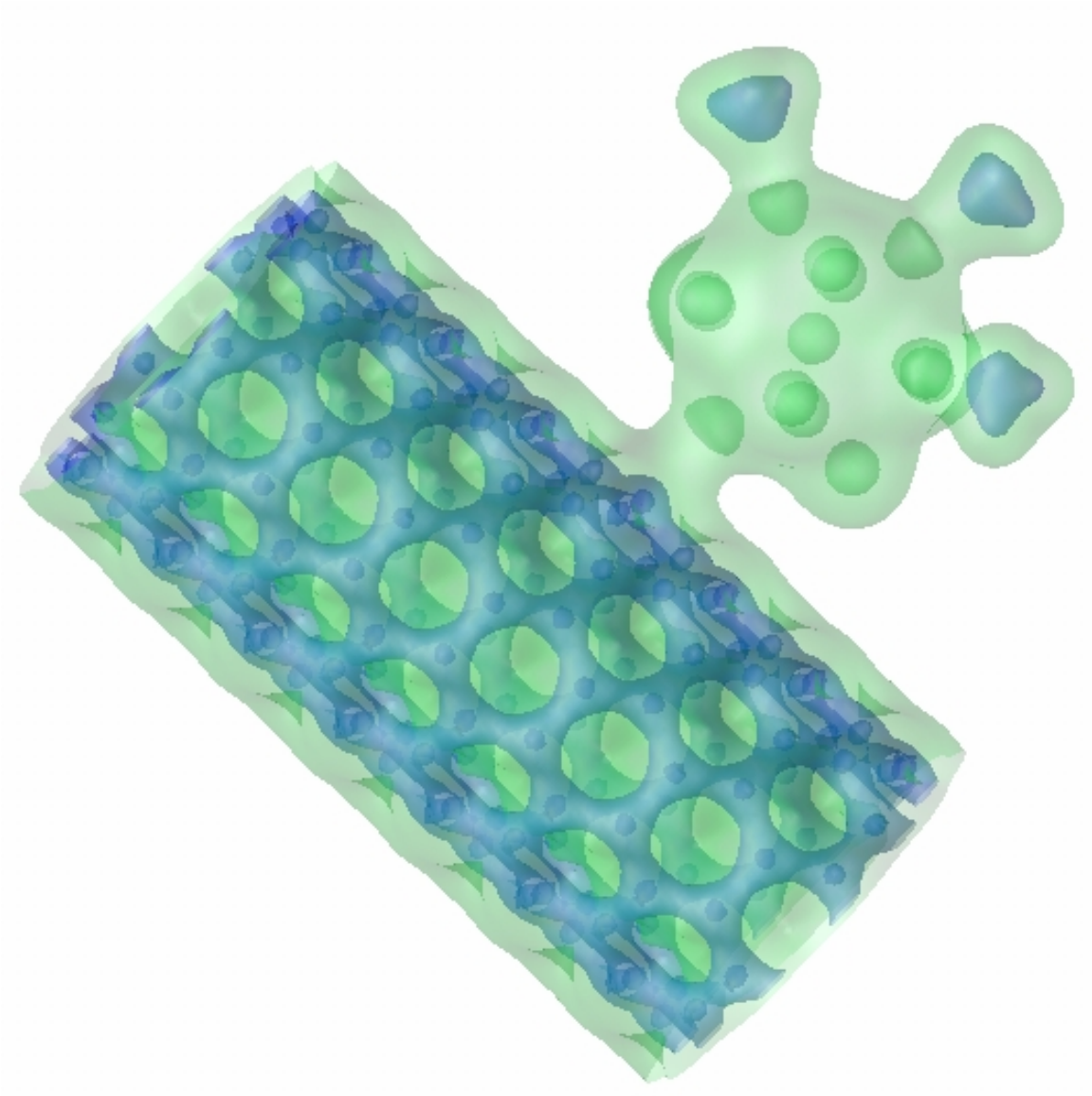

Figure 23 Total charge density of (5,5)-Al_{13} with 3 ammonia molecules. The blue iso-surface has charge density 10 times higher than the green one.

In addition to the situation of a large number of aluminum clusters on a long nanotube discussed above, we also investigated the case of a single metal cluster with a long carbon nanotube. To overcome the periodic condition, we implemented a "multi-parts" technique in our real-space grid-based *ab initio* code. We break the long 1D simulation system into three parts, left, center and right. The left and right parts can be chosen as infinite leads with perfect structure, which can be simulated separately. The central part is the conductor region, which is smoothly relaxed to the leads on either side. The three parts can be calculated separately under periodic conditions. Finally, they are combined together with their quenched local states, and the whole system is quenched with the following restrictions:

1. The eletrostatic potential and charge density in the leads (left and right parts) are fixed.
2. The eletrostatic potential and charge density in the conductor part is relaxed and smoothly converged to the leads on the boundaries.
3. The local orbitals in leads are fixed.

With these restrictions, we can simulate an open system with periodic conditions. The computational efficiency is high, since most of the calculations are concentrated in one part. The calculated conductance of one Al_{13} cluster on infinitely long (5,5) tube is shown in Figure 24. The conductance spectrum looks very similar to a typical one of defective tube. The conductance is reduced at most energy values with the lowest conductance close to 1 ($2e^2/h$). In this situation, the metal cluster acts like a local defect.

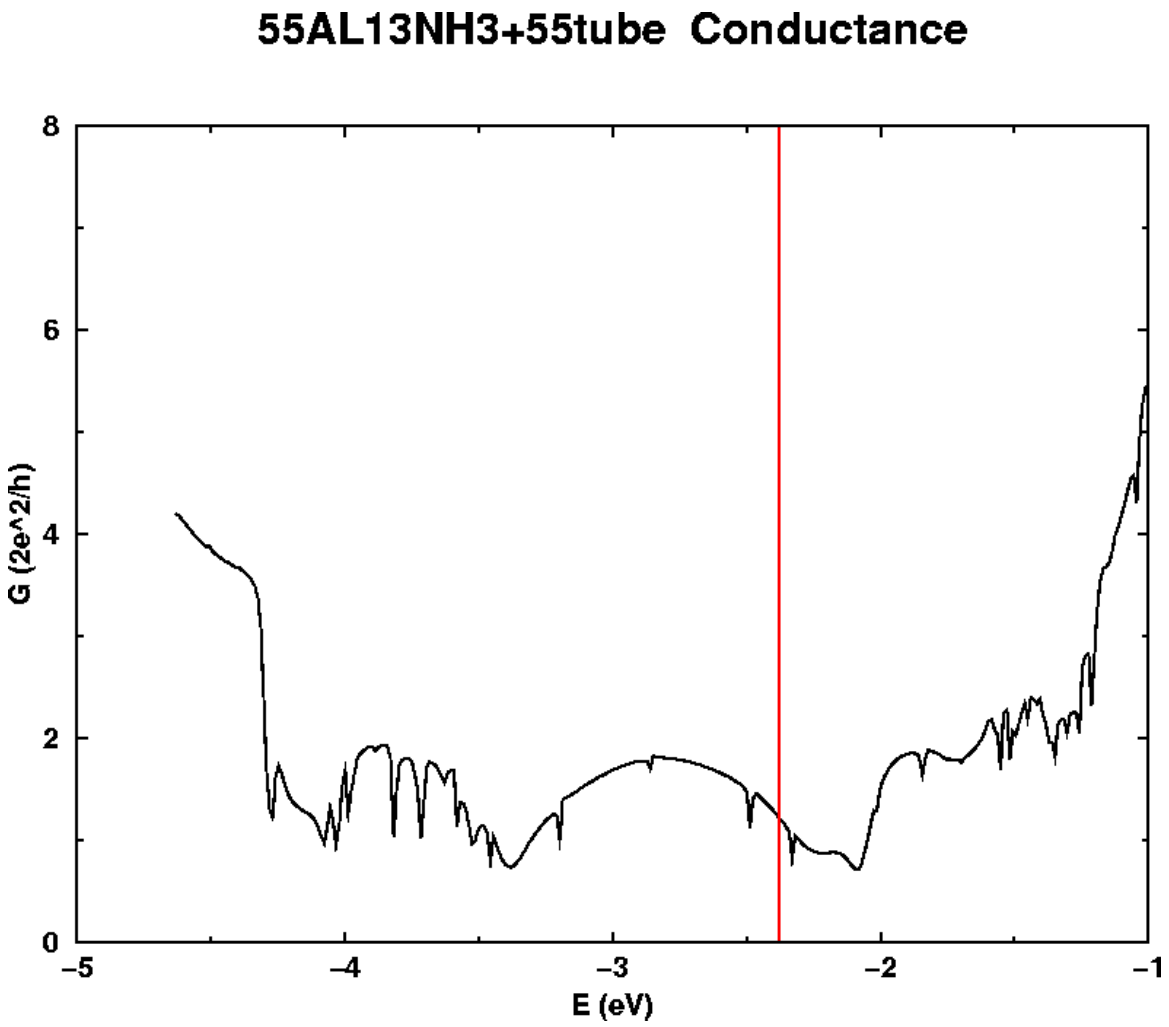

Figure 24 **Conductance of one Al_{13} on infinite long (5,5) tube. The red vertical line is the Fermi level.**

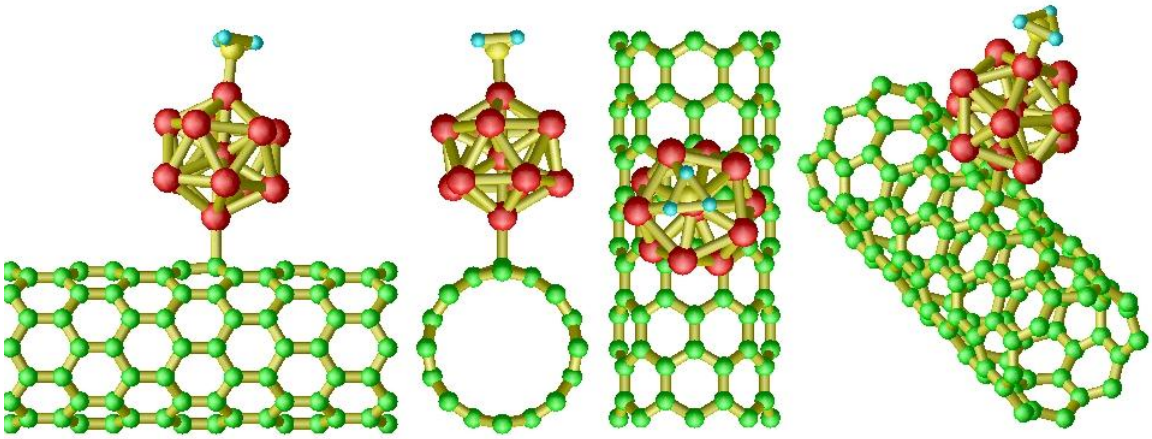

Figure 25 Atomic structure of (8,0) tube- Al_{13} after NH_3 adsorption

As we showed earlier, the semiconducting (8,0) SWNT has a stronger interaction with Al_{13}. This is shown again in Figure 25. The binding energy is 1.8 eV and the C-Al bond length is 2.11Å, the strongest in all studied cases. For the (8,0) semiconducting nanotube and Al_{13} cluster system, charge transfer happens in the same direction and with about the same amount of electrons as in the (5,5) plus Al_{13}. However, the picture of charge redistribution in the (8,0) tube- Al_{13} assembly after NH_3 adsorption is quite different. First, the Al_{13} draws more charge from NH_3 (about 0.4 electrons). Second, the (8,0) tube gets about 0.2 electrons from the metal cluster and becomes negatively charged. Furthermore, there is no extra charge attracted towards the metal cluster in (8,0) tube. The charge transfer pictures are shown in Figure 26. A comparison of structure and energy parameters in different tube-cluster assemblies before and after ammonia adsorption is given in table 1.

Table 1 Structure and energy parameters of tube-metal cluster assemblies

	(5,5)+ Al_{13}	(8,0)+ Al_{13}	(5,5)+ Al_{13}+ NH_3	(8,0)+ Al_{13}+ NH_3
formation energy	0.46 eV	0.7 eV	1.6 eV	1.8 eV
C-Al bond length	2.22 Å	2.15 Å	2.13 Å	2.11Å
N-Al			2.01 Å	2.01Å
Charge transfer	-0.1 e	-0.1 e	0/0.2 (NH_3)	0.2/0.4 (NH_3)

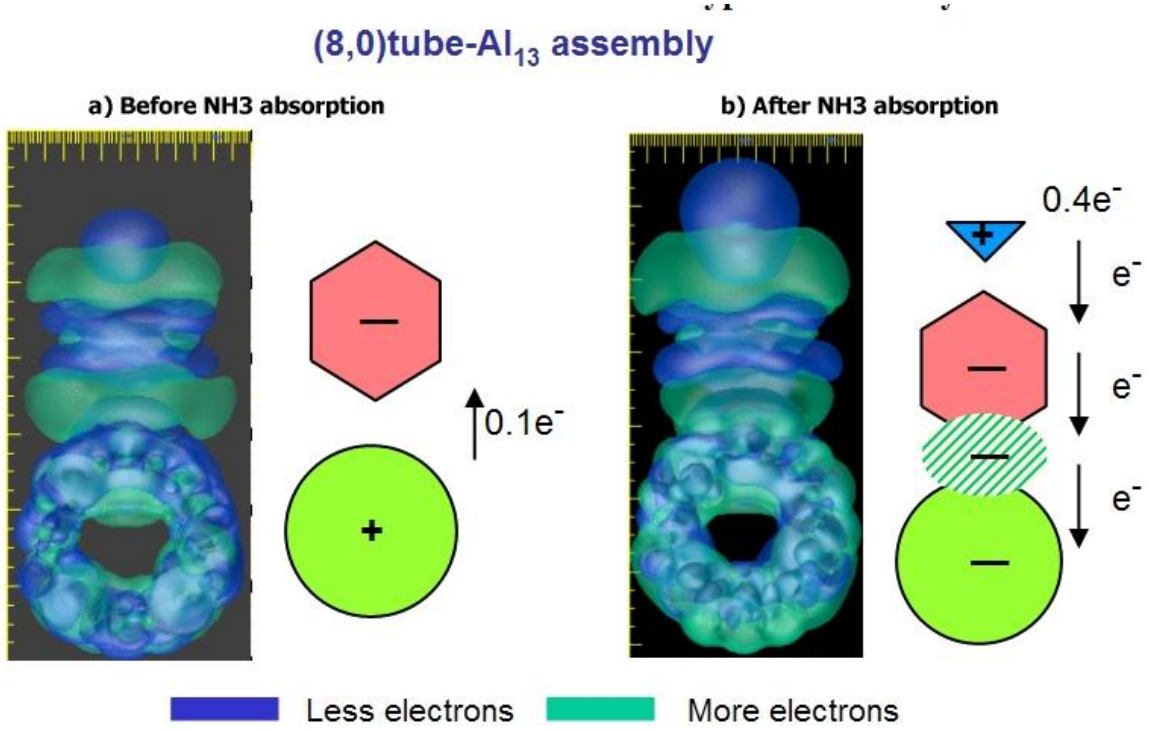

Figure 26 Charge transfer in (8,0) tube-Al_{13} assembly before and after NH_3 adsorption

When looking at the conductance of semiconducting nanotube-aluminum cluster

assemblies in Figure 27, we observed opposite effect in terms of conductivity after NH_3 adsorption. The (8,0) tube is a semiconductor with a 0.6 eV gap. The DOS figure of (8,0)-Al_{13} shows that there are some localized aluminum states (including HOMO) in the gap. The Fermi level is pinned at the HOMO of Al_{13}, which is energetically closer to the conduction band. This will improve the conductivity of (8,0)-Al_{13} system. However, a more significant change comes from NH_3 adsorption. With the adsorbed NH_3, the HOMO of Al_{13} shifts into the valence bands. Due to the charge transfer and orbital hybridization, the Fermi level is lifted to the edge of conduction band. This makes the (8,0)-Al_{13} assembly much more conducting after absorbing one NH_3 molecule, which is undoubtedly shown in the I-V curve (Figure 28). The transferred charge can be estimated from the picture of charge redistribution and the overlapped charge between (8,0) and Al_{13}. The estimated carrier (elections here) density is about 10^7/cm. The charge projections or 3D plots of electron states show that 1d orbitals of Al_{13} are highly hybridized and delocalized. Some carbon states become quasi-bound states also.

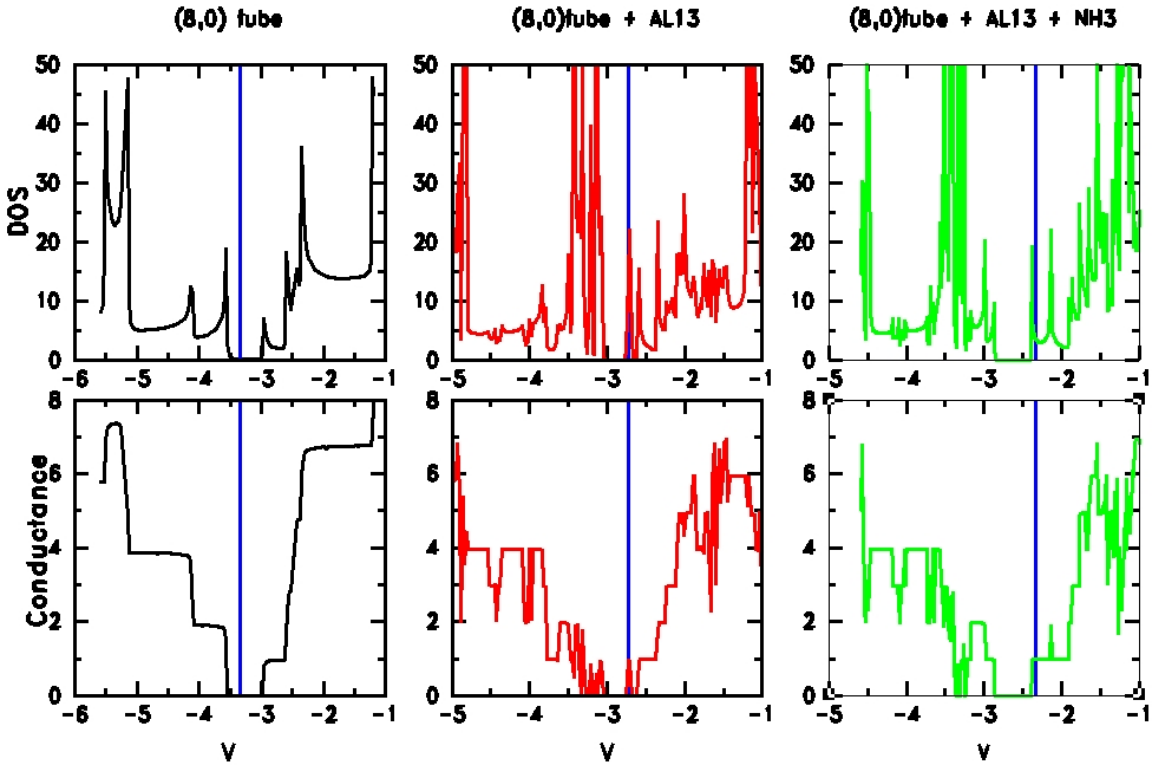

Figure 27 DOS and conductance of (8,0) tube based systems

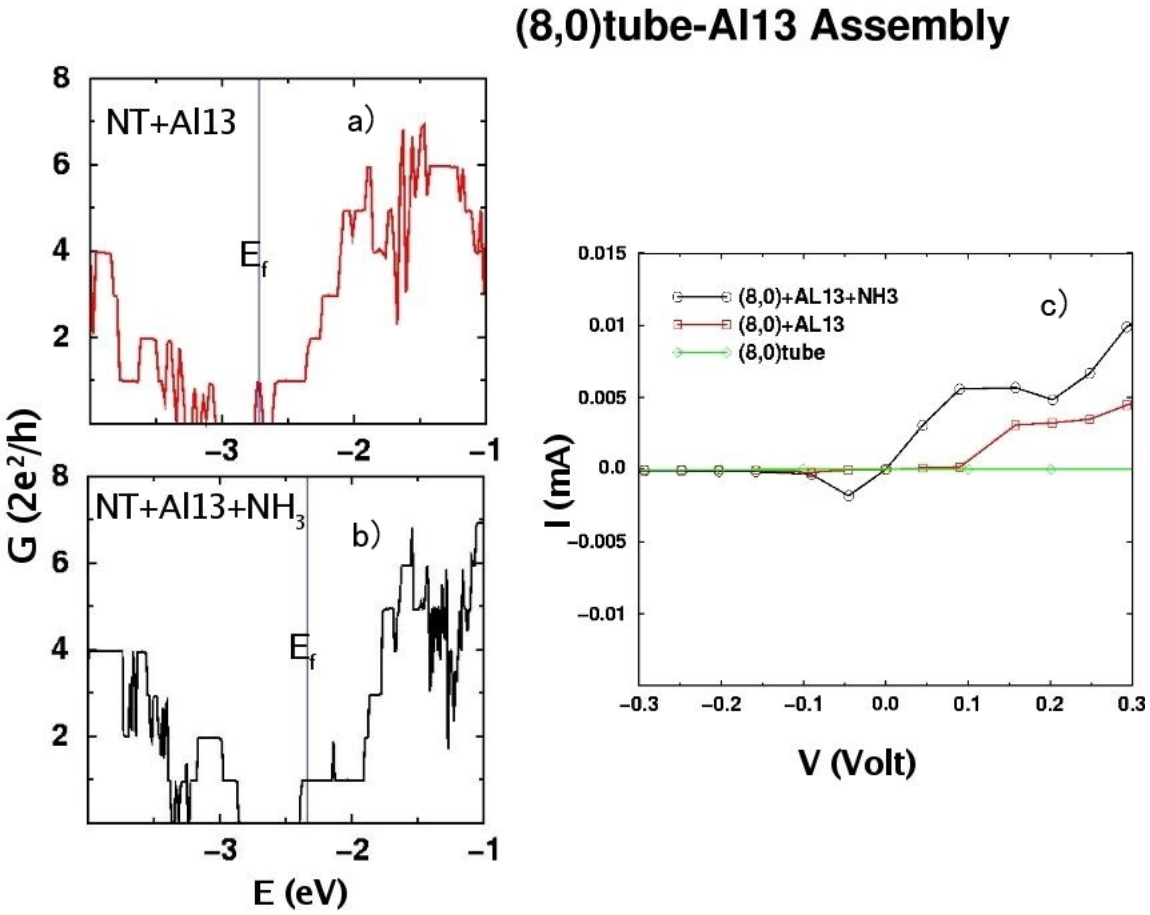

Figure 28 Conductance and I-V curves of (8,0) tube-Al_{13} assembly upon NH_3 adsorption

The above result clearly shows that SWCNT-aluminum cluster assembly can form stable structures, and that the SWCNT-Al_{13} assembly's electrical properties are very sensitive to NH_3 adsorption. This sensitivity to NH_3 gas adsorption applies to both metallic armchair and semiconducting zigzag tubes. Monitoring the resistance change of individual carbon nanotube-metal cluster assembly can detect NH_3 gas, making the nanotube- Al_{13} a good NH_3 sensor.

4.6 Conclusions

In our large-scale *ab initio* simulations, interactions between carbon nanotubes and metal clusters are explored with a paradigmatic Al_{13} metal cluster. Stable structures are recognized and their electrical transport properties are studied with and without NH_3 adsorption. We found that both metallic and semiconducting nanotubes change their conductance due to their interactions with Al_{13} and that a more dramatic change comes from NH_3 adsorption. When one or more ammonia molecule is absorbed on one vertex of Al_{13}, the conductance of (5,5)-Al_{13} assembly is reduced dramatically because of the emerging small gap. In the case of (8,0)-Al_{13} assembly, the adsorbed ammonia molecules provide significant charge to the metal cluster and the nanotube, which causes strong tube-cluster interaction. The electronic states of Al_{13} become more hybridized and delocalized, and the system's Fermi level is lifted to the edge of conduction band, which makes (8,0)-Al_{13} much more conducting after NH_3 adsorption. Through the amazing sensitivity of carbon nanotube-metal cluster assembly on NH_3 adsorption, we demonstrate the sensing capabilities of tube-metal cluster assemblies. Since both the metal clusters and the carbon nanotube are rich in members and/or structures, carbon nanotube-metal cluster assemblies could lead to a variety of chemical activities, and good selectivity may also be obtained in some cases. Therefore, the new proposed nano-materials, carbon nanotube-metal cluster assemblies, are promising molecular sensors. Furthermore, metal clusters, combined with molecular adsorption, can effectively tailor the conductance of carbon nanotubes, which is a new way of doing chemical doping. This may lead to new electronic devices based on carbon nanotube-metal cluster assemblies.

More theoretical and experimental investigations are needed to make this concept clearer. From experiment's point of view, the aluminum clusters are easily subjected to oxidization, compared to gold and silver clusters. However, it may be possible to do the transport measurement in vacuum or inert gas. With the fact that the Al_{13} is more stable than most other aluminum clusters and Al_{13}- does not interact with oxygen, we expect some experimental work toward carbon nanotube-aluminum cluster assemblies. The most important message this theoretical work brings is that the conductivity of carbon nanotube-metal cluster assembly is sensitive to gas adsorption, which has great implication for sensor applications of carbon nanotubes.

Bibliography

[1] D. Frenkel and B. Smit, *Understanding Molecular Simulation*, Academic Press, San Diego CA (1996).

[2] C. M. Moringe, D. R. Bowler and E. Hernández, Tight-binding modeling of materials, Rep. Prog. Phys **60**, 1447 (1997).

[3] M. C. Payne, M. P. Teter, D. C. Allan, T. A. Arias and J. D. Joannopoulos, Iterative minimization techniques for ab initio total-energy calculations: molecular dynamics and conjugate gradients, Rev. Mod. Phys. **64**, 1045 (1992).

[4] R. O. Jones and O. Gunnarsson, The density functional formalism, its applications and prospects, Rev. Mod. Phys. **61**, 689 (1989).

[5] K. Flurchick, A Tour of the foundations of computational chemistry and material science, online lecture (http://www.osc.edu/ASC/PET/CCM/skeleton/training/courses/foundations/foundations.html), (1997).

[6] F. Bloch, Über die quantenmechanik der electronen in kristallgittern, Z. Physik **52**, 555 (1928).

[7] J. C. Slater and G. F. Koster, Simplified LCAO method for the periodic potential problem, Phys. Rev. **94**, 1498 (1954).

[8] P. O. Lowdin, On the non-orthogonality problem connected with the use of atomic wave functions in the theory of molecules and crystals, J. Chem. Phys. **18**, 365 (1950).

[9] D. J. Chadi, (110) surface atomic structures of covalent and ionic semiconductors, Phys. Rev. B 19, 2074 (1979).

[10] S. Froyen and W. A. Harrison, Elementary prediction of linear combination of atomic orbitals matrix elements, Phys. Rev. B **20**, 2420 (1979).

[11] L. Goodwin, A. J. Skinner, and D. G. Pettifor, Generating transferable tight-binding parameters – application to silicon, Europhys. Lett. **9**, 701 (1989).

[12] C. H. Xu, C. Z. Wang, C. T. Chan, and K. M. Ho, A transferable tight-binding potential for carbon, J. Phys. C **4**, 6047 (1992).

[13] J. Dorantes-Dávila, A. Vega, and G. M. Pastor, Self-consistent theory of overlap interactions in the tight-binding method, Phys. Rev. B **47**, 12995 (1993).

[14] J. Dorantes-Dávila and G. M. Pastor, Alternative local approach to nonorthogonal tight-binding theory: Environment dependence of the interaction parameters in an orthogonal basis, Phys. Rev. B **51**, 16627 (1995).

[15] D. A. Mirabella, C. M. Aldao, and R. R. Deza, Effects of orbital nonorthogonality on band structure within the tight-binding scheme, Phys, Rev. B **50**, 12152 (1994).

[16] B. A. Mckinnon and T. C. Choy, Significance of nonorthogonality in tight-binding models, Phys. Rev. B **52**, 14531 (1995).

[17] R. S. Mulliken, Quelques aspects de la theorie des orbitales molecularires, J. Chem. Phys. 46, 497 (1949).

[18] R. S. Mulliken, Quelques aspects de la theorie des orbitales molecularires (suite et fin), J. Chem. Phys. 46, 675 (1949).

[19] M. Vanschilfgaarde and W. A. Harrison, Electronic-structure of boron, J. Phys. Chem. Solids 46, 1093 (1985).

[20] M. Vanschilfgaarde and W. A. Harrison, Theory of the multicenter bond, Phys. Rev. B 33, 2653 (1986).

[21] See any quantum mechanics textbook.

[22] P. J. H. Deteneer and W van Haeringen, The pseudopotential-density-functional method in momentum space: details and test cases, J. Phys. C **18**, 4127 (1985).

[23] J. Ihm, Alex Zunger and Marvin L Cohen, Momentum-space formalism for the total energy of solids, J. Phys. C **12**, 4409 (1979).

[24] J. C. Phillips, Energy-band interpolation scheme based on a pseudopotential, Phys. Rev. **112**, 685 (1958).

[25] N. W. Achcroft and N. D. Mermin, Solid State Physics (Holt Saunders, Philadelphia), p. 113 (1976).

[26] P. Hohenberg and W. Kohn, Inhomogeneous electron gas, Phys. Rev. **136**, B864 (1964).

[27] W. Kohn and L. J. Sham, Self-consistent equations including exchange and correlation effects, Phys. Rev. **140**, A1133 (1965).

[28] M. Levy, Proc. Natl. Acad. Sci. (USA) **76**, 6062 (1979).

[29] R. O. Jones and O. Gunnarsson, The density functional formalism, its applications and prospects, Rev. Mod. Phys. **61**, 689 (1989).

[30] E. P. Wigner, Trans. Faraday Soc. **34**, 678 (1938).

[31] S. H. Vosko, L. Wilk and M. Nusair, Can. J. Phys. **58**, 1200 (1980).

[32] J.P. Perdew and A. Zunger, Self-interaction correction to density-functional approximations for many-electron systems, Phys. Rev. B **23**, 5048 (1981).

[33] E. Fermi, Nuovo Cimento **11**, 157 (1934).

[34] H. J. Hellmann, J. Chem. Phys. **3**, 61 (1935).

[35] M. L. Cohen and J. R. Chelikowsky, Electronic Structure and Optical Properties of Semiconductors, (Springer-Verlag Berlin Heidelberg, 1989).

[36] L. Kleinman and D. M. Bylander, Efficacious form for model pseudopotentials, Phys. Rev. Lett. **48**, 1425 (1982).

[37] R. Car and M. Parrinello, Unified Approach for Molecular Dynamics and Density-Functional Theory, Phys. Rev. Lett. **55**, 2471 (1985).

[38] M. C. Payne, J. D. Joannopoulos, D. C. Allan, M. P. Teter and David H. Vanderbilt, Molecular dynamics and *ab initio* total energy calculations, Phys. Rev. Lett. **56**, 2656 (1986).

[39] Michael P. Teter, Michael C. Payne and Douglas C. Allan, Solution of schrödinger's equation for large systems, Phys. Rev. B **40**, 12255 (1989).

[40] I. Stich, R. Car, M. Parrinello and S. Baroni, Conjugate gradient minimization of the energy functional: A new method for electronic structure calculation, Phys. Rev. B **39**, 4997 (1989).

[41] M. J. Gillan, Calculation of the vacancy formation energy in aluminium, J. Phys: condens. Matter **1**, 689 (1989).

[42] D. C. Allan and M. P. Teter, Nonlocal pseudopotential in molecular-dynamical density-functional theory: application to SiO_2, Phys. Rev. Lett. **59**, 1136 (1987).

[43] Y. Bar-Yam and S. T. Pantelides, *Ab initio* pseudopotential solid-state calculations of highly electronegative first-row elements, Phys. Rev B **39**, 3396 (1989).

[44] A. M. Rappe, K. M. Rabe, Efthimios Kaxiras and J. D. Joannopoulos, Optimized pseudopotentials, Phys. Rev. B **41**, 1227 (1990).

[45] N. Troullier and José Luís Martins, Efficient pseudopotentials for plane-wave calculations, Phys. Rev. B **43**, 1993 (1991).

[46] D. Vanderbilt, Soft self-consistent pseudopotentials in a generalized eigenvalue formalism, Phys. Rev. B

41, 7892 (1990).

[47] A. Brandt, S. McCormick and J. Ruge, Multigrid methods for differential eigenproblems, J. Sci. Stat. Comput. **4**, 244 (1983).

[48] W. L. Briggs, A multigrid tutorial, the Society for industrial an applied mathematics, Lancaster Press, Lancaster, Pennsylvania (1987).

[49] A. Brandt, Math. Compt. **31**, 333(1977); GMD Studien **85**, 1 (1984).

[50] E. L. Briggs, D.J. Sullivan, and J. Bernholc, Large-scale electronic structure calculations with multigrid acceleration, Phys. Rev. B **52**, R5471 (1995); Real-space multigrid-based approach to large-scale electronic structure calculations, Phys. Rev. B **54**, 14362 (1996).

[51] P. E. Gill, W. Murray and M. H. Wright, p. 144, 1981, Practical Optimization(Academic, London).

[52] J.-L. Fattebert and J. Bernholc, Towards grid-based O(N) density-functional theory methods: Optimized nonorthogonal orbitals and multigrid acceleration, Phys. Rev. B **62**, 1713 (2000).

[53] G. Galli and M. Parrinello, Large scale electronic structure calculations, Phys. Rev. Lett. **69**, 3547 (1992).

[54] J. Tersoff, Empirical interatomic potential for carbon, with applications to amorphous carbon, Phys. Rev. Lett. **61**, 2879 (1988); New empirical approach for the structure and energy of covalent systems, Phys. Rev. B **37**, 6991 (1988).

[55] D.W. Brenner, Empirical potential for hydrocarbons for use in simulating the chemical vapor deposition of diamond films, Phys. Rev. B **42**, 9458 (1990).

[56] J. A. Majewski and P. Vogl, Crystal stability and structural transition pressures of sp-bonded solids, Phys. Rev. Lett. **57**, 1366 (1986); Simple model for structural properties and crystal stability of sp-bonded solids, Phys. Rev. B **35**, 9666 (1987).

[57] A. D. Becke, Density functional calculations of molecular bond energies, J. Chem. Phys. **84**, 4524 (1986).

[58] J. P. Perdew and W. Yue, Accurate and simple density functional for the electronic exchange energy: Generalized gradient approximation, Phys. Rev. B **33**, 8800 (1986).

[59] J. P. Perdew, Density-functional approximation for the correlation energy of the inhomogeneous electron gas, Phys. Rev. B **33**, 8822 (1986).

[60] J. P. Perdew, K. Burke and M. Ernzerhof, Generalized gradient approximation made simple, Phys. Rev. Lett. **77**, 3865 (1996).

[61] H. W. Kroto, J. R. Health, S. C. O'Brien, R. F. Curl, and R. E. Smalley, C60: Buckminsterfullerene, Nature **318**, 162 (1985).

[62] R. F. Curl, Dawn of the fullerenes: experiment and conjecture, Rev. Mod. Phys. **69**, 691 (1997).

[63] H. Kroto, Symmetry, space, starts and C60, Rev. Mod. Phys. **69**, 703 (1997).

[64] R. E. Smalley, Discovering the fullerenes, Rev. Mod. Phys. **69**, 723 (1997).

[65] J. Bernholc, C. Roland, and B.I. Yakobson, Curr. Opin. Solid State Mater. Sci. **2**, 706 (1997); J. Bernholc , D. Brenner, M. Buongiorno Nardelli, V. Meunier, C. Roland, Mechanical and electrical properties of nanotubes, Annu. Rev. Mater. Sci. **32**: 347-375 (2002).

[66] For carbon nanotube books, see the following: M.S. Dresselhaus, G. Dresselhaus, P.C. Eklund, Science of fullerences and carbon nanotubes, Academic Press, San Diego CA (1996); T. Ebbessen (ed.), Carbon nanotubes: preparation and properties, CRC Press, Boca Raton, FL (1997); R. Saito, M.S. Dresselhaus and G. Dresselhaus(ed.), Physical properties of carbon nanotubes, Imperial College Press, London (1998); M.S. Dresselhaus, G. Dresselhaus and Phaedon Avouris(eds.), Carbon nanotubes: Synthesis, Structure, Properties and Applications, Springer Verlag, Berlin (2001); Liesbeth C. Venema, Electronic structure of carbon nanotubes, Delft University Press, Delft (2000); Petter J. F. Harris, Carbon nanotubes and related structures: new materials for the 21st centrury.

[67] S. Iijima, Helical microtubules of graphitic carbon, Nature **354**, 56 (1991).

[68] S. Iijima and T. Ichihashi, Single-shell carbon nanotubes of 1-nm diameter, Nature **363**, 603 (1993).

[69] D. S. Bethune, C. H. Kiang, M. S. de Vries, G. Gorman, R. Savoy, J. Vazques, and R. Beyers, Cobalt-catalysed growth of carbon nanotubes with single-atomic-layer walls, Nature **363**, 605 (1993).

[70] C. Journet, W. K. Maser, P. Bernier, A. Loiseau, M. Lamy de la Chapelle, S. Lefrant, P. Deniard, R. Lee, and J. E. Fischer, Large-scale production of single-walled carbon nanotubes by the electric-arc technique, **388**, 756 (1997).

[71] A. Thess, R. Lee, P. Nikolave, H. Dai, P. Petit, J. Robert, C. Xu, Y. H. Lee, S. G. Kim, A. G. Rinzler, D. T. Colbert, and R. E. Smalley, Crystalline Ropes of Metallic Carbon Nanotubes, Science **273**, 483 (1996).

[72] J. Kong, A. M. Cassell, and H. Dai, Chemical vapor deposition of methane for single-walled carbon

nanotubes**,** Chem. Phys. Lett. **292**, 567 (1998).

[73] J. Kong, H. T. Soh, A. M. Cassell, C. F. Quate, C. F. Quate, and H. Dai, Synthesis of individual single-walled carbon nanotubes on patterned silicon wafers, Nature **395**, 878 (1998).

[74] A. M. Cassel, J. A. Raymakers, J. Kong, and H. Dai, Large scale CVD synthesis of single-walled carbon nanotubes, J. Phys. Chem. B **103**, 6484 (1999).

[75] T. W. Ebbesen and P. M. Ajayan, Large-scale synthesis of carbon nanotubes, Nature **358**, 220 (1992)

[76] D. S. Bethune, C. H. Kiang, M. S. DeVries, G. Gorman, R. Savoy and R. Beyers, Cobalt-catalysed growth of carbon nanotubes with single-atomic-layer walls, Nature, **363**, 605 (1993)

[77] R. S. Ruoff, D. C. Lorents, B. Chan, R. Malhotra and S. Subramoney, Single-crystal metals encapsulated in carbon nanoparticles, Science **259**, 346 (1993).

[78] M. Tomita, Y. Saito and T. Hayashi, LaC2 encapsulated in graphite nano-particle, Jap. J. Appl. Phys. **32**, L280 (1993).

[79] Z. F. Ren *et al.*, Synthesis of large arrays of well-aligned carbon nanotubes on glass, Science **282**, 1105 (1998).

[80] J. Liu *et al.*, Fullerene pipes**,** Science, **280**, 1253 (1998).

[81] Z. F. Ren *et al.*, Synthesis of large arrays of well-aligned carbon nanotubes on glass, Science **282**, 1105 (1998).

[82] Brigitte Vigolo, Alain Pénicaud, Claude Coulon, Cédric Sauder, René Pailler, Catherine Journet, Patrick Bernier, and Philippe Poulin, Macroscopic Fibers and Ribbons of Oriented Carbon Nanotubes, *Science*, **290**, 1331 (2000).

[83] H. W. Zhu, C. L. Xu, D. H. Wu, B. Q. Wei, R. Vajtai, and P. M. Ajayan, Direct Synthesis of Long Single-Walled Carbon Nanotube Strands, Science **296**, 884 (2002).

[84] M. Yudasaka, R. Kikuchi, T. Matsui, Y. Ohki, S. Yoshimura, and Etsuro Ota, Specific conditions for Ni catalyzed carbon nanotube growth by chemical vapor deposition, Appl. Phys. Lett. **67**, 2477 (1995).

[85] A. Maiti, C. J. Brabec and J. Bernholc, Kinetics of metal-catalyzed growth of single-walled carbon nanotubes, Phys. Rev. B 55, R6097 (1997).

[86] M. Buongiorno Nardelli, C. Brabec, A. Maiti, C. Roland, and J. Bernholc, Lip-Lip Interactions and the Growth of Multiwalled Carbon Nanotubes, Phys. Rev. Lett. **80**, 313–316 (1998).

[87] P. Zhang and V. H. Crespi, Nucleation of Carbon Nanotubes without Pentagonal Rings, Phys. Rev. Lett. **83**, 1791–1794 (1999).

[88] X. Fan, R. Buczko, A. A. Puretzky, D. B. Geohegan, J. Y. Howe, S. T. Pantelides, and S. J. Pennycook, Nucleation of Single-Walled Carbon Nanotubes, Phys. Rev. Lett. **90**, 145501 (2003).

[89] J. Gavillet, A. Loiseau, C. Journet, F. Willaime, F. Ducastelle, and J.-C. Charlier, Root-Growth Mechanism for Single-Wall Carbon Nanotubes, Phys. Rev. Lett. **87**, 275504 (2001).

[90] R. H. Baughman, A. A. Zakhidov, and W. A. de Heer, Carbon nanotubes—the route toward applications, Science **297**, 787(2002).

[91] D. Srivastava, M. Menon, and K. Cho, Computational nanotechnology with carbon nanotubes and fullerenes, Nanotechnology, **3**, 42 (2001).

[92] M. M. J. Treacy, T. W. Ebbesen and J. M. Gibson, Exceptionally high Young's modulus observed for individual carbon nanotubes, *Nature* **381**, 678 (1996).

[93] S. Iijima, C. Brabec, A. Maiti, and J. Bernholc, Structural flexibility of carbon nanotubes, J. Chem. Phys. **104**, 2089 (1996).

[94] M. R. Falvo, G. J. Clary, R. M. Taylor, V. Chi, and F. P. Brooks Jr., S. Washburn, and R. Superfine, Bending and bucking of carbon nanotubes under large strain, Nature **389**, 582 (1997).

[95] B. I. Yakobson, C. J. Brabec, and J. Bernholc, Nanomechanics of carbon tubes: Instabilities beyond linear response, Phys. Rev. Lett. **76**, 2511 (1996).

[96] T. W. Tombler, C. Zhou, L. Alexseyev, J. Kong, H. Dai, L. Liu, C. S. Jayanthi, M. Tang, S. Wu, Reversible electromechanical characteristics of carbon nanotubes under local-probe manipulation, Nature **405**, 769 (2000).

[97] D. Srivastava, M. Menon, and K. Cho, Nanoplasticity of Single-Wall Carbon Nanotubes under Uniaxial Compression, Phys. Rev. Lett. **83**, 2973 (1999).

[98] D. Qian, E. C. Dickey, R. Andrews and T. Rantell, Load transfer and deformation mechanisms in carbon nanotube-polystyrene composites, Appl. Phys. Lett. **76**, 2868 (2000).

[99] M. J. Biercuk, M. C. Llaguno, M. Radosavljevic, J. K. Hyun, and A. T. Johnson, and J. E. Fischer, Carbon nanotube composites for thermal management, Appl. Phys. Lett. **80**, 2767 (2002).

[100] R. H. Baughman, C. Cui, A. A. Zakhidov, Z. Iqbal, J. N. Barisci, G. M. Spinks, G. G. Wallace, A.

Mazzoldi, D. De Rossi, A. G. Rinzler, O. Jaschinski, S. Roth, and M. Kertesz, Carbon Nanotube Actuators, Science **284**, 1340 (1999).

[101] H. Dai, J. H. Hafner, A. G. Rinzler, D. T. Colbert, R. E. Smalley, Nature **384**, 147 (1996).

[102] J. H. Hafner, C. L. Cheung, C. M. Leiber, Growth of nanotubes for probe microscopy tips, Nature **398**, 761 (1999).

[103] J. W. Mintmire, B. I. Dunlap and C. T. White, Are fullerene tubules metallic?, Phys. Rev. Lett. **68**, 631 (1992).

[104] N. Hamada, S. Sawada and A. Oshiyama, New one-dimensional conductors - graphitic microtubules, Phys. Rev. Lett., **68**, 1579 (1992).

[105] R. Saito, M. Fujita, G. Dresselhaus and M. S. Dresselhaus, Electronic structure of graphene tubules based on C-60, Phys. Rev. B **46**, 1804 (1992).

[106] S. J. Tans, M. H. Devoret, H. Dai, A. Thess, R. E. Smalley, L. J. Geerligs and C. Dekker, Individual single-wall carbon nanotubes as quantum wires, Nature, **386**, 474 (1997).

[107] A.G. Rinzler, J.H. Hafner, P. Nikolaev, L. Lou, S.G. Kim, D. Tománek, P. Nordlander, D.T. Colbert, and R.E. Smalley, Unraveling Nanotubes: Field Emission from an Atomic Wire, Science **269**, 1550 (1995).

[108] W. A. de Heer, A. Châtelain, and D. Ugarte, A Carbon Nanotube Field-Emission Electron Source, Science **270**, 1179 (1995).

[109] Y. S. Choia, J. H. Kanga, Y. J. Parkb, W. B. Choib, C. J. Leec, S. H. Joc, C. G. Leec, J. H. Youc, J. E. Junga, N. S. Leeb and J. M. Kim, An under-gate triode structure field emission display with carbon nanotube emitters, Diamond and Related Materials **10**, 1705 (2001).

[110] Y. Saito and S. Uemura, Field emission from carbon nanotubes and its applications to electron sources, Carbon 38, **169** (2000).

[111] H. Sugie, M. Tanemura, V. Filip, K. Iwata, K. Takahashi, and F. Okuyama, Carbon nanotubes as electron source in an x-ray tube, Appl. Phys. Lett. **78**, 2578 (2001).

[112] C. Bower, O. Zhou and W. Zhu, U.S. patent, Device Comprising Thin Film Carbon Nanotube Electron Field Emitter Structure, filed July, 1999, serial no. 09/351537.

[113] M.E. Read, W.G. Schwarz, M.J. Kremer, J.D. Lennhoff, D.L. Carnahan, K. Kempa, and Z.F. Ren, Carbon nanotube-based cathodes for microwave tubes, Proceedings of the 2001 Particle Accelerator

Conference, Chicago.

[114] A. C. Dillon, K. M. Jones, T. A. Bekkedahl, C. H. Kiang D. S. Bethune and M. J. Heben, Storage of hydrogen in single-walled carbon nanotubes, Nature **386**, 377, (1997).

[115] B. Gao, C. Bower, J. D. Lorentzen, L. Fleming, A. Kleinhammes, X. P. Tang, L. E. McNeil, Y. Wu, and O. Zhou, Enhanced saturation lithium composition in ball-milled single-walled carbon nanotubes, Chem. Phys. Lett. **327**, 69 (2000)

[116] S. C. Tsang, Y. K. Chen, P. J. F. Harris and M. L. H. Green, A simple chemical method of opening and filling carbon nanotubes, Nature **372**, 159 (1994)

[117] P. J. F. Harris, S. C. Tsang, J. B. Claridge and M. L. H. Green, High-resolution electron microscopy studies of a microporous carbon produced by arc-evaporation, J. Chem. Soc., Faraday Trans **90**, 2799 (1994).

[118] G. Gao, T. Cağin, W. A. Goddard, Energetics, structure, mechanical and vibrational properties of single-walled carbon nanotubes, Nanotechnology **9**, 184 (1998).

[119] M. Yu, B. S. Files, S. Arepalli, and R. S. Ruoff, Tensile Loading of Ropes of Single Wall Carbon Nanotubes and their Mechanical Properties, Phys. Rev. Lett. **84**, 5552 (2000).

[120] D. A. Walters, L. M. Ericson, M. J. Casavant, J. Liu, D. T. Colbert, K. A. Smith, and R. E. Smalley, Elastic strain of freely suspended single-wall carbon nanotube ropes, Appl. Phys. Lett. **74**, 3803 (1999)

[121] E. W. Wong, P. E. Sheehan, and C. M. Lieber, Nanobeam Mechanics: Elasticity, Strength, and Toughness of Nanorods and Nanotubes, Science **277**, 1971 (1997).

[122] M. Yu, O. Lourie, M. J. Dyer, K. Moloni, T. F. Kelly, and R. S. Ruoff, Strength and Breaking Mechanism of Multiwalled Carbon Nanotubes Under Tensile Load, Science **287**, 637 (2000).

[123] O. Lourie and H. D. Wagner, Evaluation of Young's modulus of carbon nanotubes by micro-Raman spectroscopy, J. Mater. Res. **13**, 2418 (1998).

[124] G. Overney, W. Zhong, and D. Tomanek, Structural rigidity and low-frequency vibrationa-modes of long carbon tubules, Z. Phys. D: At., Mol. Clusters **27**, 93 (1993).

[125] G. G. Tibbetts, Why are carbon filaments tubular, J. Cryst. Growth **66**, 632 (1984).

[126] A. J. Stone and D. J. Wales, Theoretical studies of icosahedral C60 and some related species, Chem. Phys. Lett. **128**, 501 (1986).

[127] S. Frank, P. Poncharal, Z. L. Wang, and W. A. de Heer, Carbon Nanotube Quantum Resistors, Science **280**, 1744 (1998).

[128] H. J. Choi, J. Ihm, Y. Yoon and S. G. Louie, Possible explanation for the conductance of a single quantum unit in metallic carbon nanotubes, Phys. Rev. B **60**, R14009 (1999).

[129] S. Sanvito, Y. Kwon, D. Tománek, and C. J. Lambert, Fractional Quantum Conductance in Carbon Nanotubes, Phys. Rev. Lett. **84**, 1974 (2000).

[130] P. Delaney, M. Di Ventra, and S. T. Pantelides, Quantized conductance of multiwalled carbon nanotubes, Appl. Phys. Lett. **75**, 3787 (1999).

[131] J. Kong, E. Yenilmez, T. W. Tombler, W. Kim, H. Dai, R. B. Laughlin, L. Liu, C. S. Jayanthi, and S. Y. Wu, Quantum Interference and Ballistic Transmission in Nanotube Electron Waveguides, Phys. Rev. Lett. **87**, 106801 (2001).

[132] W. Liang, M. Bockrath, D. Bozovic, J. H. Hafner, M. Tinkham, H. Park, Fabry - Perot interference in a nanotube electron waveguide, Nature **411**, 665 (2001).

[133] Y. Yoon, P. Delaney and S. G. Louie, Quantum conductance of multiwall carbon nanotubes, Phys. Rev. B **66**, 073407 (2002).

[134] R. Heyd, A. Charlier, and E. McRae, Uniaxial-stress effects on the electronic properties of carbon nanotubes, Phys. Rev. B **55**, 6820 (1997).

[135] L. Yang and J. Han, Electronic Structure of Deformed Carbon Nanotubes, Phys. Rev. Lett. **85**, 154 (2000).

[136] M. Buongiorno Nardelli, Electronic transport in extended systems: Application to carbon nanotubes, Phys. Rev. B **60**, 7828 (1999).

[137] C. T. White, T. N. Todorov, Carbon nanotubes as long ballistic conductors, Nature **393**, 240 (1998)

[138] M. P. Anantram, and T. R. Govindan, Conductance of carbon nanotubes with disorder: A numerical study, Phys. Rev. B **58**, 4882 (1998).

[139] P. L. McEuen, M. Bockrath, D. H. Cobden, Y.Yoon, and S. G. Louie, Disorder, Pseudospins, and Backscattering in Carbon Nanotubes, Phys. Rev. Lett. **83**, 5098 (1999).

[140] J. Kong, N. R. Franklin, C. Zhou, M. G. Chapline, S. Peng, K. Cho, H. Dai, Nanotube Molecular Wires as Chemical Sensors, Science **287**, 622 (2000).

[141] P. G. Collins, K. Bradley, M. Ishigami, and A. Zettl, Extreme Oxygen Sensitivity of Electronic Properties of Carbon Nanotubes, Science **287**, 1801 (2000).

[142] S. Jhi, S. G. Louie, and M. L. Cohen, Electronic properties of oxidized carbon nanotubes, Phys. Rev. Lett., **85**, 1710 (2000).

[143] H. Ulbricht, G. Moos, and T. Herte, Physisorption of molecular oxygen on single-wall carbon nanotube bundles and graphite, Phys. Rev. B **66**, 075404 (2002).

[144] S. Dag, O. Gülseren, T. Yildirim, and S. Ciraci, Oxygenation of carbon nanotubes: Atomic structure, energetics, and electronic structure, Phys. Rev. B **67**, 165424 (2003).

[145] P. Giannozzi, R. Car, and G. Scoles, Oxygen adsorption on graphite and nanotubes, J. Chem. Phys. **118**, 1003 (2003)

[146] Hyoung Joon Choi, Jisoon Ihm, Steven G. Louie and Marvin L. Cohen, Defects, Quasibound States, and Quantum Conductance in Metallic Carbon Nanotubes, Phys. Rev. Lett. **84**, 2917 (2000).

[147] Marc Bockrath, Wenjie Liang, Dolores Bozovic, Jason H. Hafner, Charles M. Lieber, M. Tinkham, and Hongkun Park, Resonant Electron Scattering by Defects in Single-Walled Carbon Nanotubes, Science **291**, 283 (2001).

[148] P. Kim, L. Shi, A. Majumdar, and P. L. McEuen, Thermal Transport Measurements of Individual Multiwalled Nanotubes, Phys. Rev. Lett. **87**, 215502 (2001)

[149] M. Kociak, A. Yu. Kasumov, S. Guéron, B. Reulet, I. I. Khodos, Yu. B. Gorbatov, V. T. Volkov, L. Vaccarini, and H. Bouchiat, Superconductivity in Ropes of Single-Walled Carbon Nanotubes, Phys. Rev. Lett. **86**, 2416 (2001).

[150] Z. K. Tang, Lingyun Zhang, N. Wang, X. X. Zhang, G. H. Wen, G. D. Li, J. N. Wang, C. T. Chan, and Ping Sheng, Superconductivity in 4 Angstrom Single-Walled Carbon Nanotubes, Science **292**, 2462 (2001).

[151] M. Buongiorno Nardelli, B.I. Yakobson, and J. Bernholc, Mechanism of strain release in carbon nanotubes, Phys. Rev. B **57**, R4277 (1998).

[152] A. Krishan, E. Dujardin, T. W. Ebbesen, P. N. Yianilos and M. M. J. Treacy, Young's modulus of single-walled nanotubes, Phys. Rev. B **58**, 14013 (1998); D.H. Robertson, D.W. Brenner, and J.W. Mintmire, *ibid*. **45**, 12592 (1992).

[153] M. Buongiorno Nardelli, B.I. Yakobson, and J. Bernholc, Brittle and Ductile Behavior in Carbon Nanotubes, Phys. Rev. Lett. **81**, 4656 (1998).

[154] P. Zhang, P.E. Lammert, and V.H. Crespi, Plastic Deformations of Carbon Nanotubes, Phys. Rev. Lett. **81**, 5346 (1998).

[155] B.I. Yakobson, Mechanical relaxation and "intramolecular plasticity" in carbon nanotubes, Appl. Phys. Lett. **72**, 918 (1998)

[156] D. Ceperley and B. Alder, Ground State of the Electron Gas by a Stochastic Method, Phys. Rev. Lett. **45**, 566 (1980).

[157] D. Hamann, M. Schlüter, and C. Chiang, Norm-Conserving Pseudopotentials, Phys. Rev. Lett. **43**, 1494 (1979).

[158] G. Bachelet, D. Hamann, and M. Schlüter, Pseudopotentials that work: From H to Pu, Phys. Rev. B **26**, 4199 (1982).

[159] D. Hamann, Generalized norm-conserving pseudopotentials, Phys. Rev. B **40**, 2980 (1989)

[160] E. Kaxiras and K.C. Pandey, Energetics of defects and diffusion mechanisms in graphite, Phys. Rev. Lett. **61**, 2693 (1988).

[161] J. Yu, R. K. Kalia, and P. Vashishta, Phonons in graphitic tubules: A tight-binding molecular dynamics study, J. Chem. Phys. **103**, 6697 (1995).

[162] B.I. Dunlap, Connecting carbon tubules, Connecting carbon tubules, Phys. Rev. B **46**, 933 (1992)

[163] T.W. Ebbesen and T. Takada, Topological and SP3 defect structures in nanotubes, Carbon **33**, 973 (1995).

[164] P.h. Lambin, A. Fonseca, J.P. Vigneron, J.B. Nagy, and A.A. Lucas, Structural and electronic properties of bent carbon nanotubes, Chem. Phys. Lett. **245**, 85 (1995).

[165] L. Chico, V.H. Crespi, L.X. Benedict, S.G. Louie, and M.L. Cohen, Pure Carbon Nanoscale Devices: Nanotube Heterojunctions, Phys. Rev. Lett. **76**, 971 (1996).

[166] M. Ouyang, J.-L. Huang, C.L. Cheung, and C.M. Lieber, Atomically Resolved Single-Walled Carbon Nanotube Intramolecular Junctions, Science **291**, 97 (2001).

[167] D. Orlikowski, M. Buongiorno Nardelli, J. Bernholc, and C. Roland, Ad-dimers on Strained Carbon Nanotubes: A New Route for Quantum Dot Formation?, Phys. Rev. Lett. **83**, 4132 (1999).

[168] C. Zhou, J. Kong, E. Yenilmez, H. Dai, Modulated Chemical Doping of Individual Carbon Nanotubes, Science **290**, 1552 (2000).

[169] U. Schlecht, I. Besnard, T. Vossmeyer, A. Yasuda, K. Balasubramanian, M. Burghard, K. Kern, Chemically modified carbon nanotube networks for gas sensing, Nanotube 2002 conference.

[170] J. Li, Y. Lu, Q. Ye, M. Cinke, J. Han, and M. Meyyappan, Carbon Nanotube Sensors for Gas and Organic Vapor Detection, Nano Lett. **3**, 929 (2003).

[171] K. Besteman, J. Lee, F. G. M. Wiertz, H. A. Heering, and C. Dekker, Enzyme-Coated Carbon Nanotube as single-molecule biosensors, Nano Lett. **3**, 727(2003).

[172] B. F. Erianger, B. Chen, M. Zhu, and L. Brus, Binding of an Anti-Fullerene IgG monoclonal antibody to single wall carbon nanotubes, Nano Lett. **1**, 465 (2001).

[173] S. S. Wong, E. Joselevich, A. T. Woolley, C. Cheung and C. M. Lieber, Covalently functionalized nanotubes as nanometer-sized probes in chemistry and biology, Nature, **394**, 52 (1998).

[174] Y. Cui, Q. Wei, H. Park, C. M. Lieber, Nanowire nanosensors for highly sensitive and selective detection of biological and chemical species, Science **293**, 1289 (2001).

[175] R. J. Chen, Y. Zhang, D. Wang, and H. Dai, Noncovalent sidewall functionalization of single-walled carbon nanotubes for protein immobilization, J. Am. Chem. Soc. **123**, 3838(2001).

[176] M. Shim, N. Wong, S. Kam, R. J. Chen, Y. Li, and H. Dai, Functionalization of carbon nanotubes for biocompatibility and biomolecular recognition, Nano Lett. **2**, 285 (2002).

[177] K. A. Williams, P. T. M. Veenhuizen, B. G. de la Torre, R. Eritja, C. Dekker, Carbon nanotubes with DNA recognition, Nature **420**, 761, (2002).

[178] K. G. Ong, K. Zeng, C. A. Grimes. A wireless, passive, carbon nanotube-based gas sensor. IEEE Sensors Journal, vol. **2,** 82 (2002).

[179] S. Chopra and a. Pham, J. Gaillard, A. Parker, and A. M. Rao, Carbon-nanotube-based resonant-circuit sensor for ammonia, Appl. Phys. Lett. **80**, 4632 (2002).

[180] S. J. Tans, A. R. M. Verschueren, C. Dekker, Room-temperature transistor based on a single carbon nanotube, Nature **393**, 49 (1998).

[181] U. Schlecht, I. Besnard, T. Vossmeyer, A. Yasuda, K. Balasubramanian, M. Burghard, K. Kern, Chemically modified carbon nanotube networks for gas sensing, Nanotube 2002 conference. (The

modification of the SWNT-network with 1 nm palladium-film increases the sensitivity of the sensor.)

[182] S. Datta, Electronic Transport in Mesoscopic Systems, Cambridge University Press, Cambridge, (1995).

[183] F. Ferry and S. Goodnick, Transport in Nanostructures, Cambridge University Press, Cambridge, (1997).

[184] N. D. Lang, Resistance of atomic wires, Phys. Rev. B **52**, 5335 (1995).

[185] M. Di Ventra, S. T. Pantelides, and N. D. Lang, First-Principles Calculation of Transport Properties of a Molecular Device, Phys. Rev. Lett. **84**, 979 (2000).

[186] J. Mozos, C. C. Wan, G. Taraschi, J. Wang, and H. Guo, Quantized conductance of Si atomic wires, Phys. Rev. B **56**, R4351 (1997).

[187] H. J. Choi and J. Ihm, *Ab initio* pseudopotential method for the calculation of conductance in quantum wires, Phys. Rev. B **59**, 2267 (1999).

[188] H. J. Choi, J. Ihm, Steven G. Louie and Marvin L. Cohen, Defects, Quasibound States, and Quantum Conductance in Metallic Carbon Nanotubes, Phys. Rev. Lett. **84**, 2917 (2000).

[189] K. Hirose and M. Tsukada, First-principles calculation of the electronic structure for a bielectrode junction system under strong field and current, Phys. Rev. B **51**, 5278 (1995).

[190] N. Kobayashi, M. Brandbyge, and M. Tsukada, First-principles study of electron transport through monatomic Al and Na wires, Phys. Rev. B **62**, 8430 (2000).

[191] U. Landman, R. Barnett, A. G. Scherbakov, and P. Avouris, Metal-Semiconductor Nanocontacts: Silicon Nanowires, Phys. Rev. Lett. **85**, 1958 (2000).

[192] M. Buongiorno Nardelli, J.-L. Fattebert, and J. Bernholc, O(N) real-space method for ab initio quantum transport calculations: Application to carbon nanotube–metal contacts, Phys. Rev. B **64**, 245423 (2001).

[193] M. Buongiorno Nardelli and J. Bernholc, Mechanical deformations and coherent transport in carbon nanotubes, Phys. Rev. B **60**, R16338 (1999).

[194] G. Mie, Ann. Phys. (Leipzig) **25**, 377 (1908).

[195] U. Kreibig, Z. Phys. **234**, 307 (1970).

[196] E. J. Robbins, R. E. Leckenby and P. Willis, Adv. Phys. **16**, 739 (1967).

[197] W. D. Knight, K. Clemenger, W. A. de Heer, W. A. Saunders, M. Y. Chou and M. L. Cohen, Electronic Shell Structure and Abundances of Sodium Clusters, Phys. Rev. Lett. **52**, 2141 (1984).

[198] S. G. Nilsson, K. Dan. V. Selsk, Mat. Fys. Medd. **29**, No. 16 (1955).

[199] J. L. Martins, R. Car, and J. Buttet, Surf. Sci. **106**, 265 (1981).

[200] W. Ekardt, Dynamical Polarizability of Small Metal Particles: Self-Consistent Spherical Jellium Background Model, Phys. Rev. Lett. **52**, 1925 (1984); Work function of small metal particles: Self-consistent spherical jellium-background model, Phys. Rev. B **29**, 1558 (1984).

[201] J. Pedersen, S. Bjornholm, J. Borggreen, K. Hansen, T. P. Martin, and H. D. Rasmussen, Nature **353**, 733 (1991).

[202] K. Clemenger, Phys. Rev. B **32**, 1359 (1985); Ph. D. thesis, University of California, Berkeley (1985).

[203] H. A. Jahn and E. Teller, Proc. R. Soc. London Ser. A **161**, 220 (1937).

[204] Proceedings of ISSPIC:

ISSPIC 1, 1977, J. Phys. (Orsay) **38**, C2.

ISSPIC 2, 1981, Surf. Sci. **106**.

ISSPIC 3, 1985, Surf. Sci. **156**.

ISSPIC 4, 1989, Z. Phys. D **12**.

ISSPIC 5, 1991, Z. Phys. D **19**, **20**.

ISSPIC 6, 1993, Z. Phys. D **26**

ISSPIC7, Kobe (Japan) 1994, Surf. Rev. Lett. **3** (1996)

ISSPIC 8, Kopenhagen 1996, Springer Verlag, Berlin (1997); Z. Phys. D **40** (1997).

ISSPIC9, Lausanne 1998, Eur. Phys. J. D **9** (1999)

ISSPIC10, Atlanta 2000, Eur. Phys. J. D **16** (2001)

ISSPIC 11, Eur. Phys. J. D, in print (2003)

[205] W. A. de Heer, The Physics of simple metal clusters: experimental aspects and simple models, Rev. Mod. Phys., **65**, 611 (1993).

[206] M. Brack, The physics of simple metal clusters: self-consistent jellium model and semiclassical approaches, Rev. Mod. Phys., **65**, 677 (1993)

[207] M. F. Jarrold, J. E. Bower, and J. S. Kraus, Collision induced dissociation of metal cluster ions: Bare aluminum clusters, Al_n^+ (n=3–26), J. Chem. Phys. **86**, 3876 (1987).

[208] D. M. Cox, D. J. Trevor, R. L. Whetten, E. A. Rohlfing, and A. Kaldor, Aluminum clusters: Magnetic

properties, J. Chem. Phys. **84**, 4651 (1986).

[209] S. A. Ruatta, L. Hanley and S. L. Aanderson, Size-dependent barriers for reaction of aluminum cluster ions with oxygen, Chem. Phys. Lett. **137**, 5 (1987).

[210] W. A. de Heer, P. Milani, and A. Chtelain, Nonjellium-to-jellium transition in aluminum cluster polarizabilities, Phys. Rev. Lett. **63**, 2834 (1989).

[211] K. E. Schriver, J. L. Persson, E. C. Honea, and R. L. Whetten, Electronic shell structure of group-IIIA metal atomic clusters, Phys. Rev. Lett. **64**, 2539 (1990).

[212] J. L. Persson, R. L. Whetten, H. Cheng and R. Stephen Berry, Evidence for quantized electronic level structure for 100–1300 electrons in metal-atomic clusters, Chem. Phys. Lett. **186**, 215 (1991).

[213] M. Pellarin, B. Baguenard, M. Broyer, J. Lermé, J. L. Vialle, and A. Perez, Shell structure in photoionization spectra of large aluminum clusters, J. Chem. Phys. **98**, 944 (1993).

[214] K. J. Taylor, C. L. Pettiette, M. J. Craycraft, O. Chesnovsky and R. E. Smalley, UPS of negative aluminum clusters, Chem. Phys. Lett. **152**, 347 (1988).

[215] G. Gantefor *et al.,* Faraday Discuss. Chem. Soc. **86**, 197 (1988).

[216] G. Ganteför and W. Eberhardt, Shell structure and s—p hybridization in small aluminum clusters, Chem. Phys. Lett. **217**, 600 (1994).

[217] C. Cha, G. Ganteför, and W. Eberhardt, The development of the 3p and 4p valence band of small aluminum and gallium clusters, J. Chem. Phys. **100**, 995 (1994).

[218] B. Baguenard, M. Pellarin, J. Lermé, J. L. Vialle, and M. Broyer, Competition between atomic shell and electronic shell structures in aluminum clusters, J. Chem. Phys. **100**, 754 (1994).

[219] J. Lermé, M. Pellarin, J. L. Vialle, B. Baguenard, and M. Broyer, Evidence for classical star orbit in large Al_N clusters, Phys. Rev. Lett. **68**, 2818 (1992).

[220] E. Cottancin, M. Pellarin, J. Lermé, B. Baguenard, B. Palpant, J. L. Vialle, and M. Broyer, Unimolecular dissociation of trivalent metal cluster ions: The size evolution of metallic bonding, *ibid.* **107**, 757 (1997)

[221] T. H. Upton, A perturbed electron droplet model for the electronic structure of small aluminum clusters, J. Chem. Phys. **86**, 7054 (1987).

[222] L. G. M. Pettersson and C. W. Bauschlicher, Jr., T. Halicioglu, Small Al clusters. II. Structure and binding in Al_n (n=2–6, 13), *ibid.* **87**, 2205 (1987).

[223] J. Y. Yi, D. J. Oh, and J. Bernholc, Structural distortions in metal clusters, Phys. Rev. Lett. 67, 1594 (1991).

[224] H. P. Cheng, R. S. Berry, and R. L. Whetten, Electronic structure and binding energies of aluminum clusters, Phys. Rev. B **43**, 10647 (1991).

[225] S. N. Khanna and P. Jena, Assembling crystals from clusters, Phys. Rev. Lett. **69**, 1664 (1992).

[226] S. N. Khanna and P. Jena, Atomic clusters: Building blocks for a class of solids, Phys. Rev. B **51**, 13 705 (1995).

[227] R. O. Jones, Structure and bonding in small aluminum clusters, Phys. Rev. Lett. **67**, 224 (1991).

[228] R. O. Jones, Simulated annealing study of neutral and charged clusters: Al_n and Ga_n, J. Chem. Phys. **99**, 1194 (1993)

[229] J. Akola, M. Manninen, H. Häkkinen, U. Landman, X. Li and L. Wang, Aluminum cluster anions: Photoelectron spectroscopy and ab initio simulations, Phys. Rev. B. **62**, 13216 (2000).

[230] X. Li, H. Wu, X. Wang, and L. Wang, s- p Hybridization and Electron Shell Structures in Aluminum Clusters: A Photoelectron Spectroscopy Study, Phys. Rev. Lett. **81**, 1909 (1998).

[231] N. W. Ashcroft and N. D. Mermin, Solid State Physics, Holt, Rinehart, and Winston, New York, (1976).

[232] C. E. Moore, in Atomic Energy Levels, Natl. Bur. Stand. (U.S.) Circ. (U.S. GPO, Washington, D.C., 1971), Vol. I.

[233] R. R. Zope and T. Baruah, Conformers of Al_{13}, $Al_{12}M$, and $Al_{13}M$ (M=Cu, Ag, and Au) clusters and their energetics, Phys. Rev. A **64**, 053202 (2001)

[234] B. K. Rao, S. N. Khanna, and P. Jena, Isomers of Al_{13} clusters and their interaction with alkali atoms, Phys. Rev. B **62** ,7 (2001).

[235] B. K. Rao and P. Jena, Energetics and electronic structure of carbon doped aluminum clusters, J. Chem. Phys. **115**, 2 (2001).

[236] O. C. Thomas, W. Zheng, and K. H. Brown, Jr., Magic numbers in copper-doped aluminum cluster anions, J. Chem. Phys. **114** ,13 (2001).

[237] X. G. Gong and V. Kumar, Enhanced Stability of Magic Clusters: A Case Study of Icosahedral $Al_{12}X$, X=B, Al, Ca, C, Si, Ge, Ti, As, Phys. Rev. Lett. **70**, 14 (1993).

[238] J. Yi, D. J. Oh, J. Bernholc and R. Car, Structural transitions in aluminum clusters, Chem. Phys. Lett.

174 ,461 (1990).

[239] X. G. Gong and V. Kumar, Enhanced stability of magic clusters: A case study of icosahedral Al12X, X=B, Al, Ga, C, Si, Ge, Ti, As, Phys. Rev. Lett. **70**, 2078 (1993).

[240] A. P. Seitsonen, M. J. Puska, M. Alatalo, R. M. Nieminen, V. Milman, and M. C. Payne, Crystals from metallic clusters: A first-principles calculation, Phys. Rev. B **48**, 1981 (1993).

[241] A. Rubio, Y. Miyamoto, X. blasé, M. L. Cohen, and S. G. Louie, Theretical study of one-dimensional chains of metal atoms in nanotubes, Phys. Rev. B, **53**, 4023 (1996).

[242] O. Gülseren, T. Yildirim, and S. Ciraci, Tunable adsorption on carbon nanotubes**,** Phys. Rev. Lett., **87**, 116802 (2001).

[243] B. D. Leskiw and A. W. Castelman, Jr, C. Ashman and S. N. Khanna, Reactivity and electronic structure of aluminum clusters: The aluminum-nitrogen system, J. Chem. Phys. **114**, 1165 (2001).

[244] N. Watari , S. Ohnishi, Electronic structure of H adsorbed on Pt13 clusters, J. Chem. Phys. **106**, 7531 (1997).

[245] F. Huisken, B. Kohn, R. Alexandrescu, and I. Morjan, Reactions of iron clusters with oxygen and ethylene: Observation of particularly stable species**,** J. Chem. Phys. **113**, 6579 (2000).

[246] E. K. Parks, T. D. Klots, B. J. Winter, and S. J. Riley, Reactions of cobalt clusters with water and ammonia: Implications for cluster structure, J. Chem. Phys. **99**, 5831 (1993).

[247] E. K. Parks and S. J. Riley, Modeling adsorbate uptake: Coverage dependence of the iron cluster-ammonia binding energy, J. Chem. Phys. **99**, 5898 (1993).

[248] E. K. Parks, K. P. Kerns, and S. J. Riley, The binding of CO to nickel clusters. I. Determination of saturation coverages, J. Chem. Phys. **112**, 3384 (2000); The binding of CO to nickel clusters. II. Structural implications and comparisons with electron counting rules, J. Chem. Phys. **112**, 3394 (2000).

[249] Special issue on Gas-Sensing Materials, MRS Bull. **24** (1999).

[250] Y. Shimizu and M. Egashira, MRS Bull. **24**, 18 (1999).

[251] Y. Takao, K. Miyazaki, Y. Shimizu, M. Egashira, J. Electrochem. Soc. **141**, 1028 (1994).

[252] H. M. McConnell, J. C. Owicki, J. W. Parce, D. L. Miller, G. T. Baxter, H. G. Wada, and S. Pitchford, The cytosensor microphysiometer: biological applications of silicontechnology, Science **257**, 1906 (1992).

[253] A. Mandelis and C. Christofides, Physics, Chemistry and Technology of Solid State Gas Sensor Devices

(Wiley, New York, 1993).

[254] J. Miasik, A. Hooper, B. Tofield, J. Chem. Soc. Faraday Trans. 1 **82**, 1117 (1986).